Summer 2018

Development and management of advanced batteries via additive manufacturing and modeling

Jie Li

Department: Mechanical and Aerospace Engineering

DEVELOPMENT AND MANAGEMENT OF ADVANCED BATTERIES VIA ADDITIVE MANUFACTURING AND MODELING

by

JIE LI

A DISSERTATION

Presented to the Faculty of the Graduate School of the

MISSOURI UNIVERSITY OF SCIENCE AND TECHNOLOGY

In Partial Fulfillment of the Requirements for the Degree

DOCTOR OF PHILOSOPHY

in

MECHANICAL ENGINEERING

2018

Approved by:

Jonghyun Park, Advisor
Robert G. Landers
Ming Leu
Charles Wojnar
Xinhua Liang

PUBLICATION DISSERTATION OPTION

This dissertation consists of the following six articles that have been published, submitted for publication, or will be submitted for publication as follows:

Paper I: Page 6-28 has been published in the *Materials and Design* in volume 119, pp 417-424, (2017).

Paper II: Page 29-54 has been published in the *Scientific Report* in volume 8, issue 1, pp 1846, (2018).

Paper III: Page 55-80 has been prepared to the *ACS Applied Materials & Interface*.

Paper IV: Page 81-117 has been published in the *Journal of Electrochemical Societ* in volume 164, issue 4, pp A874-A883 (2017).

Paper V: Page 118-159 has been published in the *Applied Energy* in volume 212, pp 1178–1190 (2018).

Paper VI: Page 160-187 has been prepared to the *Journal of Power Source*.

ABSTRACT

The applications of Li-ion batteries require higher energy and power densities, improved safety, and sophisticated battery management systems. To satisfy these demands, as battery performances depend on the network of constituent materials, it is necessary to optimize the electrode structure. Simultaneously, the states of the battery have to be accurately estimated and controlled to maintain a durable condition of the battery system. For those purposes, this research focused on the innovation of 3D electrode via additive manufacturing, and the development of fast and accurate physical based models to predict the battery status for control purposes. Paper I proposed a novel 3D structure electrode, which exhibits both high areal and specific capacity, overcoming the trade-off between the two of the conventional batteries. Paper II proposed a macro-micro-controlled Li-ion 3D battery electrode. The battery structure is controlled by electric fields at the particle level to increase the aspect ratio and then improve battery performance. Paper III introduced a 3D model to simulate the electrode structure. The effect of electrode thickness and solid phase volume fraction were systematically studied. Paper IV proposed a low-order battery model that incorporates stress-enhanced diffusion and electrolyte physic into a Single Particle model that addresses the challenges of battery modeling for BMS: accuracy and computational efficiency. Paper V proposed a single particle-based degradation model by including Solid Electrolyte Interface (SEI) layer formation coupled with crack propagation. Paper VI introduced a single-particle-based degradation model by considering the dissolution of active materials and the Li-ion loss due to SEI layer formation with crack propagation for $LiMn_2O_4$/Graphite battery.

ACKNOWLEDGMENTS

First, I would like to express my sincere gratitude to my advisor, Dr. Jonghyun Park, who brought me into this project, offering great opportunities and providing consistent guidance, advice, and encouragement to support my study. I am deeply grateful for the great opportunities and wonderful working environment offered by Dr. Park. It has been a great privilege and a pleasure to work with him.

Besides my advisor, I would like to thank my advisory committee members, Dr. Robert Landers, Dr. Xinhua Liang, Dr. Charles Wojnar and Dr. Ming Leu, for sharing their knowledge and kindly offering me support for research. They set a significant example with their diligence and outstanding academic performance, teaching me how to be a successful engineer in my future career.

My sincere thanks also goes to Dr. Jeremy Watts, Dr. Krishna Kolan, and Dr. Nima Lotfi, for offering help and sharing their knowledge. I also thank my lab mates and colleagues, Kasim Adewuyi, Brody Riemann, Yan Gao, and my friends for their help, support, and friendship throughout my graduate work.

Finally, I would like to express my eternal appreciation and love toward my family, and, especially, my mother, Lijing He, for her constant source of support with her words of encouragement and praise.

TABLE OF CONTENTS

Page

SECTION

LIST OF ILLUSTRATIONS

Paper II

Paper III

Paper V

LIST OF TABLES

SECTION

1. INTRODUCTION

Li-ion battery is an energy storage device that operates by converting the chemical energy into electrical energy. The typical battery includes two electrodes, a separator, and the electrolyte. For the electrode, it has a positive side, i.e. cathode, and a negative side, i.e. anode. The electrode normally contains active materials, binders, and conductive materials. The cathode active material typically is one type or mixed materials of Lithium Cobalt Oxide ($LiCoO_2$), Lithium Iron Phosphate ($LiFePO_4$), Lithium Manganese Oxide ($LiMn_2O_4$), or Lithium Nickel Manganese Cobalt Oxide ($LiNiMnCoO_2$/NMC) on an aluminum current collector. The anode active material commonly uses graphite materials on a copper current collector as a full-cell or lithium metal as a half-cell. The binder typically uses a polyvinylidene fluoride (PVDF) or a copolymer polyvinylidene fluoride–hexafluroropropylene (PVDF-HFP) to hold the battery structure. A conductive material is also needed, typically a high-surface-area carbon black, to increase the conductive of electrodes. The two electrodes are isolated by the microporous separator film immersed with the electrolyte. The electrolyte can be categorized into three types: liquid electrolytes, gel-polymer electrolytes, and ceramic (i.e. solid-state) electrolytes. Liquid electrolytes are the solutions of a lithium salt in organic solvents and the electrolyte is mostly absorbed into the electrodes and separator; gel-polymer electrolytes are typically films of PVDF-HFP and a lithium salt; ceramic electrolytes refer to inorganic, solid-state materials that are ionically conductive.

The battery is operated by reversible Li-ion exchange in an intercalation process, a reaction where Li-ions are reversibly removed or inserted into the active material without a significant structural change to the host. For example, during discharging, Li-ions inside the anode active material diffuse to the particle surface of the active material where they transfer from the solid-phase to electrolyte-phase. They then travel inside the electrolyte based on the mechanism of diffusion and migration to the cathode particles and insert inside the cathode active material. Meanwhile, electrons released in the anode travel through the external circuit to generate a flow of current, and vice versa during charging.

The Li-ion battery market has grown over $30 billion in two decades since 1999, and it has rapidly become the standard power source in the markets and is applied to an increasing range of applications, such as personal electric devices, electric vehicles, drones, and satellites. The widespread use of Li-ion batteries is due to the high specific energy (Wh/kg) and energy density (Wh/L), long cycle life, a broad temperature range of operation, and cost-effectiveness with flexible shape design. In the next decade, a higher energy and power density is still required for those applications. On the other hand, the Li-ion battery will degrade during cycling and may be damaged during over-discharge/charge or over-temperature conditions, which requires a management system to detect the battery status and avoid such damages.

In order to further improve the battery performance, besides developing new materials, it is necessary to enhance battery performance via optimizing battery electrode structures because they significantly affect the transport of species and their reactions. Paper I developed a novel hybrid 3D structure electrode via extrusion-based additive

manufacturing, which exhibits both high areal and specific capacity, thus overcoming the trade-off between the two of the conventional laminated batteries. In addition, conventional battery paste components were used optimally to fit the additive manufacturing process, which eliminates the need for the complicated solvent preparation process required for typical additive manufacturing processes in battery applications. Using a CR2032 coin cell, the general assembly problem that occurs at the 3D structured electrodes was solved, which means that the proposed hybrid 3D structure can be easily added to the existing lamination structure. Paper II further developed a micro-controlled Li-ion 3D battery electrode based on the hybrid 3D structure. The 3D structure can be further controlled by applied electric fields at the particle level to increase the aspect ratio and improve battery performance. The effect of the applied electric field on electrode particles was studied based on the increase of porosity and surface area, and the battery performance with and without well-controlled 3D structure were also compared. Electrochemical tests show that the new electrodes exhibit superior performances, which is due to a high aspect ratio 3D structure and ordered particle structures. In Paper III, a three-dimensional simulation framework was developed for 3D Li-ion battery structures. The model coupled the porous theory for electrolyte potential with the solid phase potential based on a 4^{th} order approximation equation for the solid phase concentration. This model can be applied to an arbitrary structure, and provide a guideline for the design of 3D electrode structures and can assist in the optimization of 3D structures for energy storage systems.

As the usage of Li-ion battery becomes more pervasive, increased concerns about their safety have become more critical. Consequently, a Battery Management System

(BMS) is used to optimize storage capacity and balance the various systems to satisfy functional requirements and prevent catastrophic failures. To achieve these goals through a BMS, identification of the battery status is extremely important. Therefore, advanced sensing and monitoring technologies are required to accurately predict the state of the battery and track the physical parameters. Paper IV developed a low-order battery model that incorporates stress-enhanced diffusion and electrolyte physics into a modified Single Particle (SP) model that addresses two important challenges of battery modeling for BMS: accuracy and computational efficiency. The developed model improves accuracy by including the potential drop in the electrolyte based on the predicted Li-ion concentration profile along the entire electrode thickness, and by including the enhanced diffusivity due to diffusion-induced stress. Incorporating analytical solutions into a conventional SP model eliminates the need to sacrifice calculation efficiency. The voltage prediction by the proposed model is more accurate than the conventional SP model. Compared to complex physics-based battery models, the proposed model significantly improves the computational efficiency of various discharge scenarios, including constant current, the Dynamic Stress Test, and the Highway Fuel Economy Test. Integrating mechanical responses into the single particle model not only increases model accuracy, but also makes it applicable to develop models for next-generation high energy density batteries.

Accurately and quickly predicting the State of Health (SOH) of a Li-ion battery is another important function in a BMS. Battery performance declines over time due to irreversible physical and chemical changes that naturally occur until the battery can no longer be used. Battery SOH is a measure of the state of a battery’s condition compared

to its initial condition, which is represented by the capacity of the battery after certain charge-discharge cycles. For instance, when the battery capacity in electric vehicles reaches 80% of its initial capacity, the battery is no longer considered usable. Therefore, SOH estimation is an essential component of a BMS for a variety of energy storage systems. Paper V developed a single particle-based degradation model by including Solid Electrolyte Interface (SEI) layer formation, coupled with crack propagation due to the stress generated inside the particles of the active materials. This low-order model quickly predicts capacity fade and voltage profile changes as a function of cycle number and temperature with considerable accuracy, allowing for the use of on-line estimation techniques. Li-ion loss due to SEI layer formation, increase in battery resistance, and changes in the electrodes' open circuit potential operating windows are examined to account for capacity fade and power loss. Despite its low-order implementation, the model proposed in this paper provides quantitative information regarding SEI layer formation and crack propagation, as well as the resulting battery capacity fade and power dissipation. In the Paper VI, an SP model for a LiMn2O4/Graphite battery was developed by including the key degradation mechanisms: (1) Mn dissolution in the cathode and (2) Li-ion loss due to SEI layer formation in the anode coupled with mechanical degradation mechanism. The model proposed in this paper provides quantitative information regarding Mn dissolution and Li-ion loss as well as the resulting battery capacity fade.

PAPER

I. A HYBRID THREE-DIMENSIONALLY STRUCTURED ELECTRODE FOR LITHIUM-ION BATTERIES VIA 3D PRINTING

ABSTRACT

New hybrid 3D structure electrodes with a high aspect ratio are fabricated through extrusion-based additive manufacturing to achieve high mass loading. This new 3D printed battery exhibits both high areal and specific capacity, thus overcoming the trade-off between the two of the conventional laminated batteries. This excellent battery performance is achieved by introducing a hybrid 3D structure that utilizes the benefits of the existing laminated structure and three-dimensional interdigitated structure. In addition, conventional battery paste components are used optimally to fit the additive manufacturing process, which eliminates the need for a complicated solvent preparation process required for a typical additive manufacturing process for battery applications. Using the CR2032 coin cell, the general assembly problem that occurs at the 3D structured electrodes is solved, which means that the proposed hybrid 3D structure can easily be added to the existing lamination structure. This innovative design and fabrication process demonstrates the high areal energy and power density, which is a critical requirement for energy storage systems in transportation and stationary applications.

1. INTRODUCTION

Despite remarkable advancements in Lithium Ion Batteries (LIBs), during the past several decades, a higher energy and power density is still required for portable devices, transportation, and stationary applications.[1-3] In order to satisfy these demands, besides developing new materials, it is necessary to enhance battery performance via optimizing battery electrode structures because they significantly affect the transport of species and their reactions.[4,5] In general, gravimetric capacity ($mAh \cdot g^{-1}$) is one of the most utilized metrics in LIB studies as it describes the capacity that a material can deliver. However, in practice, the actual amount of materials in an electrode determines the energy and power of a LIB. Accordingly, high mass loading is another important requirement for various applications. One simple strategy for achieving high mass loading is the addition of more materials, which means increasing the thickness of electrodes. Unfortunately, this approach limits the transport of ions and electrons, resulting in poor power performance and bad utilization of materials.[4] A better option is to make electrodes smartly, so that a more facile transport of the species will be possible.[6,7] Conventional modern batteries, which are based on laminated composite electrodes, are fabricated via a paste casting process that involves mixing the constituent materials and coating them onto a current collector. In a composite electrode structure, the electrode thickness, porosity, and mass loading are the key factors for increasing areal capacity ($mAh \cdot cm^{-2}$) and maximizing usage of materials. After a certain thickness, however, the electrode shows poor power performance.[4]

Three-dimensional (3D) batteries have been considered to be a new solution for improving battery performance.[3,6,7] Battery electrodes with 3D nanoarchitectures have been successfully synthesized for almost two decades.[8-16] Some of the nano-manufacturing methods (e.g., lithography tools) are expensive and time-consuming. However, additive manufacturing has several advantages, as compared to other manufacturing tools; because it can provide an inexpensive and flexible manufacturing process that includes more complex geometry designs and a wider selection of materials.[17,18] Therefore, the additive manufacturing technique appears to be a very promising method for fabricating 3D battery structures.[7, 19-22] However, the preparation of the proper composition and rheology of paste is demanding because of several requirements, including preventing clogging of the nozzles, promoting a bond between each filament, and keeping the controlled feature geometry after deposition.[23-25] For LIB applications, in particular, the use of paste chemical components is a critical factor in battery performance, since more binders inside the paste would decrease ionic and electronic conductivity. In this respect, conventional tape casting pastes have the advantage that they do not mix unnecessary components in pastes, which has been commercially used for LIB fabrication for decades.

Currently, 3D structures are being thoroughly studied for LIB applications, but most of these studies are focused on microbatteries.[7, 19-22] Further, a strategy of adopting the advantages of the conventional laminated structure and the 3D digital structure has not been considered. In this paper, a novel hybrid 3D structured electrode was developed to overcome the limitations of conventional laminated composite electrodes via an extrusion-based additive manufacturing technique. The principal goal of

this work was to utilize the out-of-plane dimension of the 3D structured electrode, so that power and energy density could be further enhanced with short ion transport distances and an increased surface area as compared to the conventional laminated structure. The rheology of the conventional tape casting paste with different solids loadings (SL) was tested for the reliability of printing onto a controlled hybrid 3D feature of an electrode, without adding unnecessary chemical components.

2. MATERIALS AND METHODS

2.1. MATERIALS AND PASTE PREPARATION

In this work, a $LiMn_2O_4$ (LMO) paste was used to fabricate a hybrid 3D structure electrode. Two different solids loading pastes were prepared by first mixing 85.5 wt% LMO powder (MTI, 13 μm) with 6.5 wt% carbon black (CB, Alfa Aesar) and 8 wt% Polyvinylidene fluoride (PvdF, Sigma-Aldrich), and that was then dispersed in N-Methyl-2-pyrrolidone solvent (NMP, Sigma-Aldrich) for 30% SL and 15% SL paste, respectively. The paste was mixed with a SpeedMixer (FlackTeck Inc) at 2000 RMP for 20 minutes at room temperature. The paste rheology was measured by a viscometer (Brookfield model HB) equipped with a CAP-52Z cone spindle at 25 ^{o}C. The viscosity (η) was recorded as a function of RMP (0.5-5) which corresponded to the shear rate (10-1000 s^{-1}) logarithmically, and the shear stress was calculated based on measured viscosity and shear rate.

2.2. ELECTRODE FABRICATION AND CELL ASSEMBLY AND TEST

An Extrusion Freeform Fabrication (EFF) system was used (Figure 1) to deposit the paste in a 3D structure. An aluminum foil piece (5 cm × 5 cm) was fixed on a substrate heated to 120 ^{o}C prior to printing, which was used as a current collector after assembly. The deposition system was a home-built extrusion-based additive manufacturing system, which consisted of a motion subsystem, a real-time control subsystem, and extrusion devices, which were controlled by Labview 2012 software. The system contained three linear axes, Daedal 404 XR (Parker Hannifin, Rohnert Park, CA) driven by three stepper motors (Empire Magnetics, Rohnert Park,CA) and was able to print up to three different materials. In this research, a single extruder was used to extrude the LMO paste.

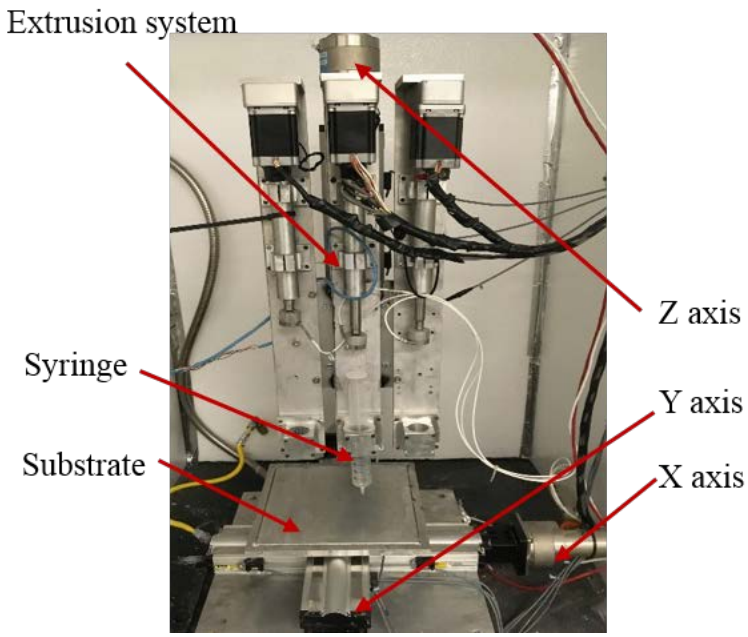

Figure 1. Extrusion Freeform Fabrication machine overview.

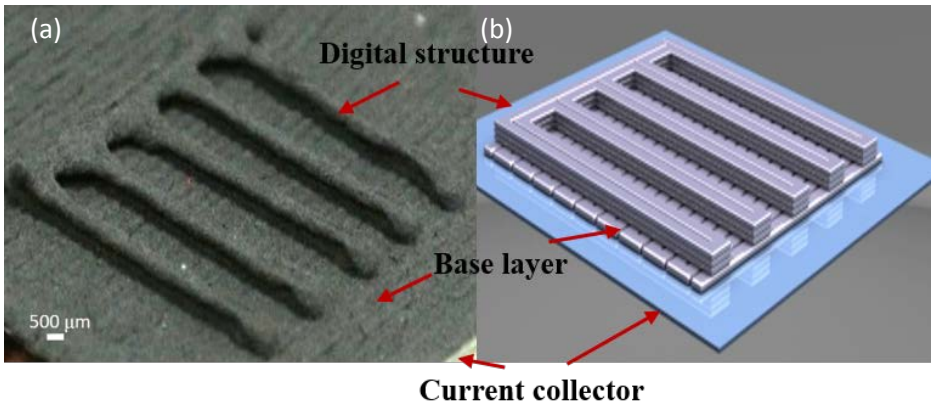

Figure 2. (a) Microscope image of printed hybrid 3D structure and (b) demonstration of hybrid 3D structure.

The paste was loaded into a 50 cc plastic syringe (EXELint) with a 200 µm nozzle (EFD Inc), and extruded with 100 N extrusion force onto a substrate that moved along the XY-axes. The hybrid 3D structure consisted of two parts: a base part and a digital structure part (Figure 2).

First, a base layer was printed to cover the current collector as a conventional laminated structure and the thickness of this base layer was optimized to yield the highest specific capacity (without 3D structure). Next, a digital structure, with a different number of layers, was printed on the top of the base layer to increase the specific surface area. All the fabricated structures were examined via scanning electron microscopy (SEM, Hitachi S4700).

A CR2032 coin cell (Wellcos Corp) was used to assemble a battery (Figure 3) in an argon-filled glove box (Mbraun). LMO was used as a cathode, Li foil as an anode, and commercial PP/PE/PP membrane (Celgard) as a separator; the battery was filled with liquid electrolyte 1M $LiFP_6$ EC:DMC 1:1 (Sigma-Aldrich).

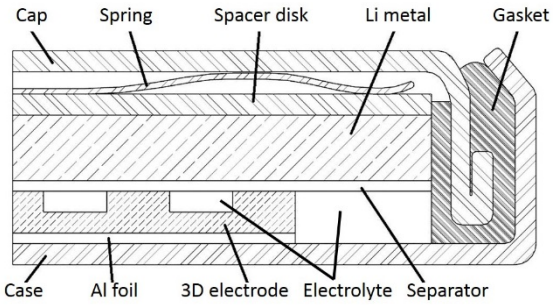

Figure 3. A CR2032 coin cell assembly with hybrid 3D structure cathode, lithium foil, separator, and electrolyte.

The electrochemical behavior of the assembled batteries was measured from 3 V to 4.2 V by using a battery testing station (IVIUMnSTAT, Ivium Tech). The specific capacity and areal capacity were measured under a 0.1 C-rate, and then the cycling performances were conducted with 0.1C, 0.2C, 0.5C, and 1C per three cycles. Battery impedance was also measured via an electrochemical impedance spectroscopy (EIS) at 3.5 V open circle voltage.

3. RESULTS AND DISCUSSION

3.1. PASTE CHARACTERISTICS

For additive manufacturing process, the paste properties, such as viscosity and shear stress, are important for obtaining a controlled shape after deposition. In contrast, the conventional tape casting pastes do not require high viscosity to free-stand after casting.[9-13]. To find the optimal paste for the processing, two batches of paste with 15% and 30% SL were first investigated for conventional tape casting process and EFF process. The rheology test results (Figure 4) indicated that both of the pastes exhibited a

shear-thinning behavior, which guaranteed that they could be extruded and controlled by the extrusion process. Also, the viscosity (10^1 ~ 10^3 Pa.s) and standoff shear stress (1.3 × 10^5 Pa) of the 30% SL paste were approximately 10 times larger than the viscosity (10^0 ~ 10^2 Pa.s) and the standoff shear stress (2 × 10^4 Pa) of the 15% SL paste. Therefore, the 30% SL paste was able to provide greater strength for the printed filaments without any collapse. Though it will be discussed in detail in Section 3.3.1, 30% SL was chosen for the additive manufacturing process in this work because SL itself has less impact on battery performance.

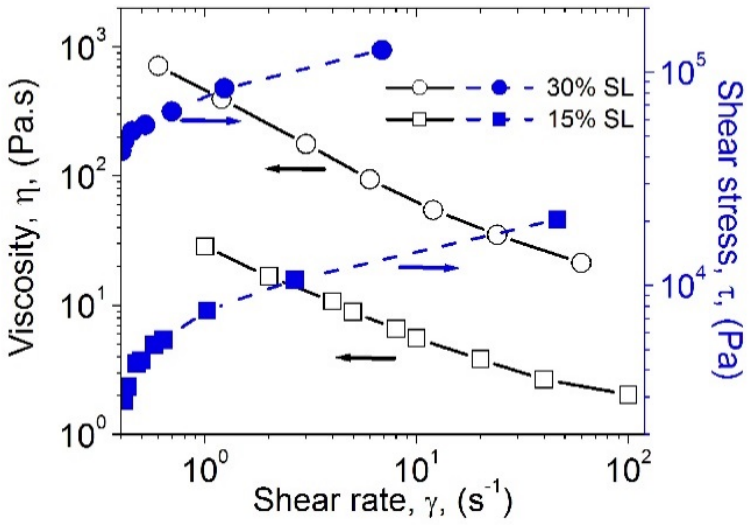

Figure 4. Paste viscosity and shear stress as a function of shear rate.

3.2. ELECTRODE STRUCTURES

After printing, the size of the printed cathode had a foot area of 10 × 10 mm^2. The thickness of the printed cathode and the width of the 3D structures were measured to investigate the possibility of collapse of the deposited layer (Figure 5a). The height of

one layer was approximately 190 μm and the width of two combined nearby filaments was 600 μm. As the layer numbers increases, the height increases linearly, but the width remains almost constant. Then, after drying, the microstructures of the hybrid 3D structure and the conventional structure were studied using SEM. All the structures in Figures 5b-f, including the hybrid structure (b), the laminated structure (c), the enlarged base layer (d) and the enlarged digital layer (e), and the enlarged laminated structure, show that the spinel LMO particles are uniformly mixed with the carbon black and the PvdF. This clearly shows that there is no significant difference in the particle-level structure inside the cells from the two different fabrication methods.

3.3. ELECTROCHEMICAL PERFORMANCE

3.3.1. Battery Capacities. First, to study the effect of SL on battery performance, and to find the optimal thickness of the base layer, only the conventional laminated structures were cast with 15% SL paste and 30% SL paste with different thickness from ~100 μm to ~400 μm. As shown in Figure 6, the battery performance of both electrodes generally exhibited similar behavior: (1) the specific capacity decreased after its maximum value (110 ± 5 mAh·g^{-1}) at 160 μm, and (2) the areal capacity continued to increase to the maximum value (3.5 ± 0.08 mAh·cm^{-2}) at 370 μm. This indicated that the SL of the paste did not significantly affect battery performance. Thus, a 30% SL solution was used for the hybrid 3D structures because the 30% SL paste significantly increased standoff stress, which, as discussed in the rheology results, provided sufficient strength to maintain the controlled shape after deposition.

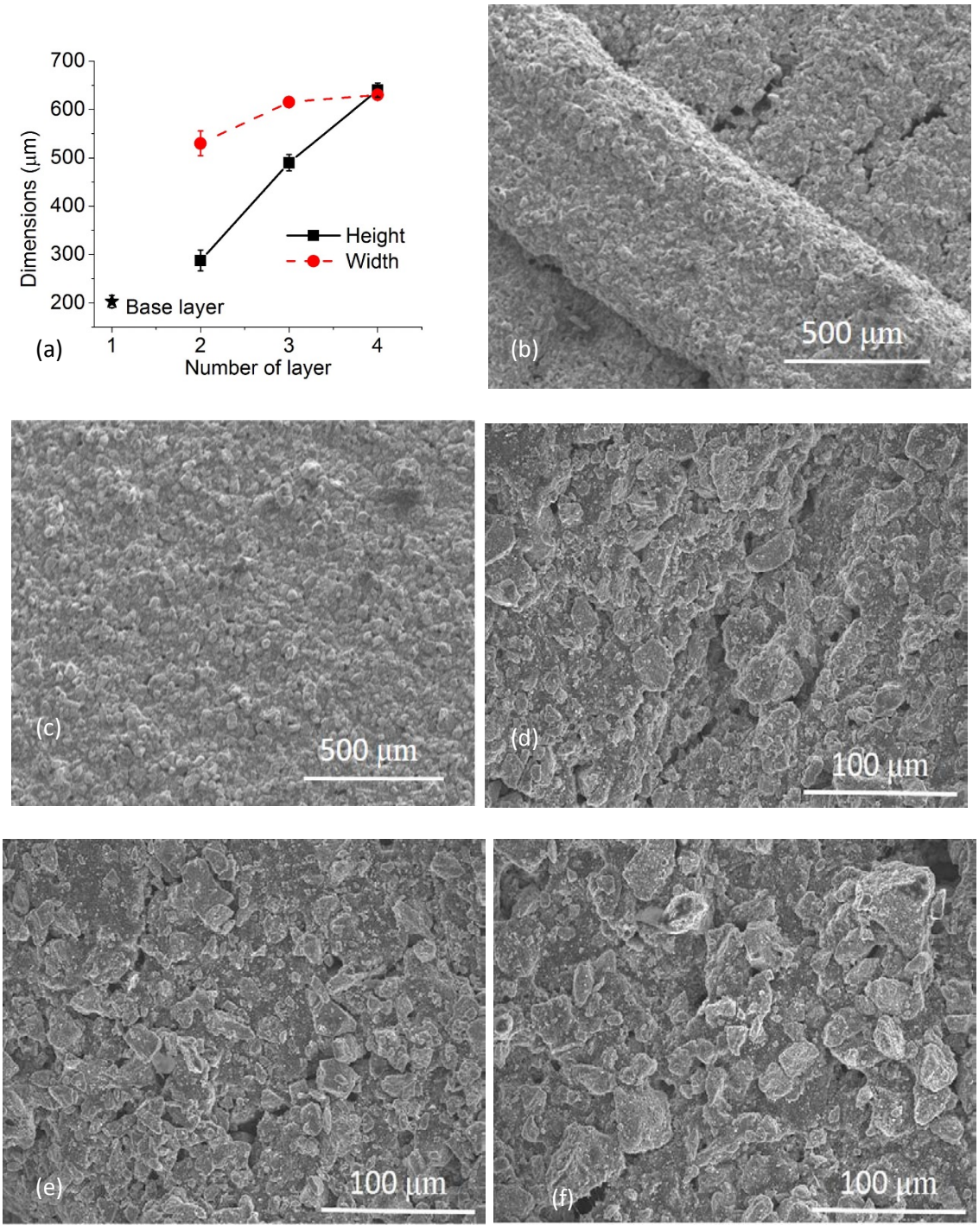

Figure 5. (a) Height and width of the printed filaments as a function of layer numbers, (b-f): SEM image of (b) the hybrid 3D structure, (c) the laminated structure, (d) the 3D printed base layer (zoomed-in), (e) the 3D printed digital structure (zoomed-in), and (f) the laminated structure (zoomed-in).

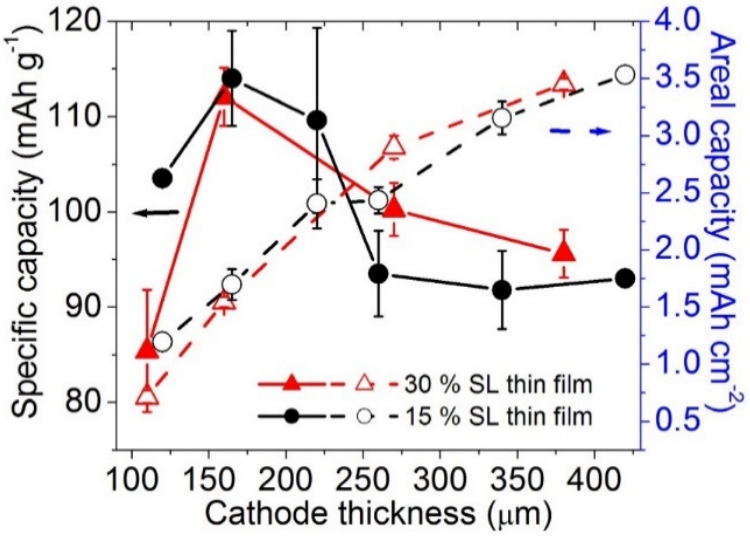

Figure 6. Comparison of specific capacity and areal capacity as a function of cathode thickness for conventional laminated structure with different solid loading.

Next, as shown in Figures. 7, the conventional laminated structure and the hybrid 3D structure were compared by specific capacity, areal capacity, and volume capacity. In the case of specific capacity (Figure 7a), the conventional laminated structure (LS) exhibited a maximum value (110 ± 5 mAh·g^{-1}) at 160 μm, and then decreased as the thickness increased further.

However, the hybrid 3D structure (HS) showed a higher value (117 ± 6 mAh·g^{-1}) than that of LS, even though it is much thicker (370 μm vs. 160 μm). As the case of LS, the specific capacity of HS was decreased from its maximum value as the thickness of electrode increased, which was attributed to the transport delay in the transportation of li-ions, in particular, the particles near the current collector are not effectively utilized at higher thickness.

On the other hand, as the thickness increased, the areal capacity of the LS continuously increased up to the maximum value (3.5 ± 0.08 mAh·cm^{-2} at 370 μm),

which is much smaller than the maximum of HS, 4.5 ± 0.3 mAh·cm^{-2} at 270 μm as shown in Figure 7b.

In Figure 7a and 7b, an asterisk indicates the value of the printed base layer ((190 μm thickness). Its specific capacity is the range of values similar to the LS, but its areal capacity is higher than value of the LS at the same thickness. The printed base of 190 μm showed an areal capacity similar to that of 270 μm LS.

For very thick (490 μm), the areal capacity of the HS is almost the same as for the maximum value, while the LS value continues to increase with thickness. This is the result of competition between the increased mass loading and reduced specific capacity as the thickness increases.

As shown in Figure 7c, the volumetric capacities decreases as the electrode thickness increases after reaching the maximum value, similar to the case of specific capacity (Figure 7a). The HS has a maximum volume capacity (180 mAh·cm^{-3}) of up to 80% greater than the conventional structure (100 mAh·cm^{-3}) in the thickness (270 μm) providing the maximum value in both cases.

In conclusion, first, the specific capacities of both HS and conventional LS are within a reasonable range of the specific capacities of LMO material (90-120 mAh·g^{-1}) [8, 26], and the areal capacities and volumetric capacities of the LS are similar to those of LMO half-cells [27, 28]. Also, as the electrode thickness increases, the areal capacities and volumetric capacities increase. By contrast, the areal capacity of HS is much higher than the values in literature. This means the new hybrid 3D structure (HS) can achieve high areal capacity without compromising specific capacity.

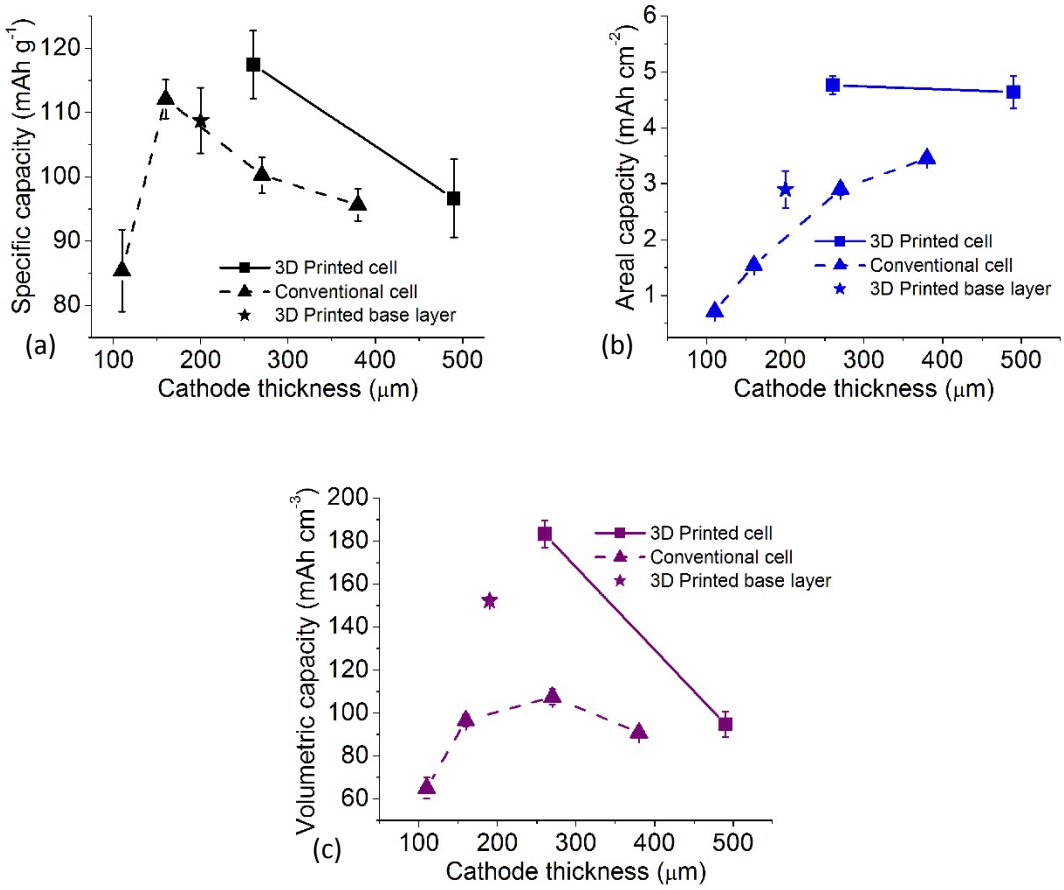

Figure 7. Comparison of conventional laminated structure and printed hybrid 3D structure as a function of cathode thickness (a) Specific capacity, (b) areal capacity, and (c) Volumetric capacity.

3.3.2. Voltage Profile and Cycling Performance. Figure 8 shows the first and second voltage profile during charge/discharge of the two best cells out of conventional laminated structure (LS) and 3D hybrid structures (HS) of different thickness, as discussed in Section 3.3.1. Those thickness are 160 μm and 270 μm for LS and HS, respectively. As shown in 8a, the specific capacity of HS in this cell is higher than that of LS in the first cycle, but similar in the second. However, as shown in 8b, the HS shows a

much higher areal capacity even in the second cycle, which is consistent with the conclusion of the previous section.

In order to study their cycle performance, each cell was cycled 3 times with 0.1C, 0.2C, 0.5C, and 1C, and then finally 8 cycles further with 0.1C again as shown in Figure 9a. Except for the first three cycles of HS, all have stable performance with a slight decrease in capacity. As expected, capacity is reduced at high C-rates due to a high ohmic resistance. However, the HS still shows higher areal capacity than the LS even at high C-rates. For instance, it shows about 1.5 times the areal capacity at the HS (0.83 $mAh{\cdot}cm^{-2}$) than at the LS (0.59 $mAh{\cdot}cm^{-2}$) at 1C. After returning to the low 0.1C, both cells show stable performance, while still the HS (3.38 $mAh{\cdot}cm^{-2}$) shows 2.6 times the specific capacity of the LS (1.30 $mAh{\cdot}cm^{-2}$). Compared with the last value of the first 0.1C cycle group, the HS showed about a 6.9% capacity decrease during the second 0.1C cycle group, which is a reflection of cumulative deterioration caused by side reactions such as Mn dissolution; this is slightly higher than the fading in the LS (4.9%), which may be related to higher surface area. Thereafter, the HS exhibits the similar capacity fade rate to the LS, which is 0.5% fade per cycle.

A higher surface areas can lead to more side reactions, such as more interface layer formation [29] or dissolution of active materials [30]. That is why we observed a larger capacity fade in the first three cycles of the HS compared to the LS. However, a high surface area does not necessarily mean a higher capacity fade rate for two reasons: (1) protective layers are formed to slow the side reactions after initial formation, even if it is not completely stable until the of its life; (2) the benefit of a short diffusion path and facile diffusion of the 3D structure can reduce ion accumulation inside active materials,

and correspondingly reduced stress level, which causes less mechanical failures, such as cracks, that directly accelerate chemical side resections due to the increase interface. As an evidence, we observed fast capacity reduction for the first three cycles in the 3D structures, but after 12 cycles, they show a fade rate of 0.5% per cycle, similar to the conventional laminated structures. The coulombic efficiency of both HS and LS is stabilized after a small drop between different C-rates and shows similar values as shown in Figure 9b.

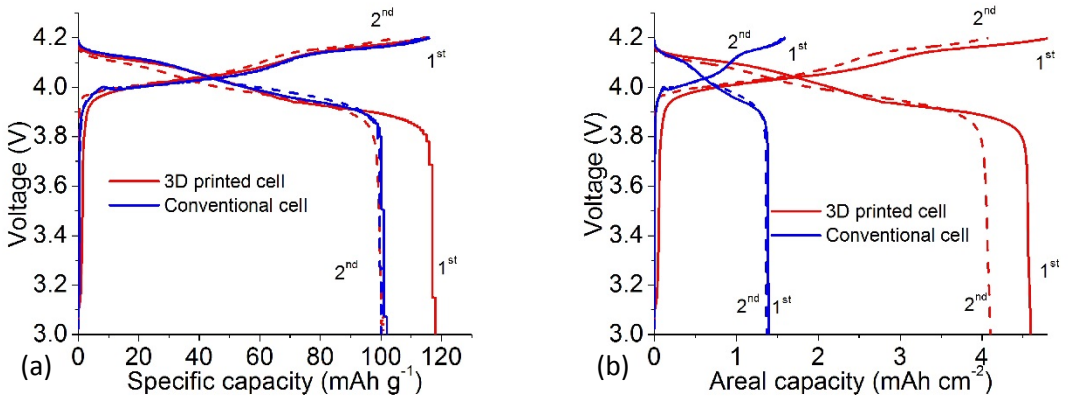

Figure 8. 1st (solid line) and 2nd (dash line) cycles (a) specific charge/discharge capacity and (b) areal charge/discharge capacity.

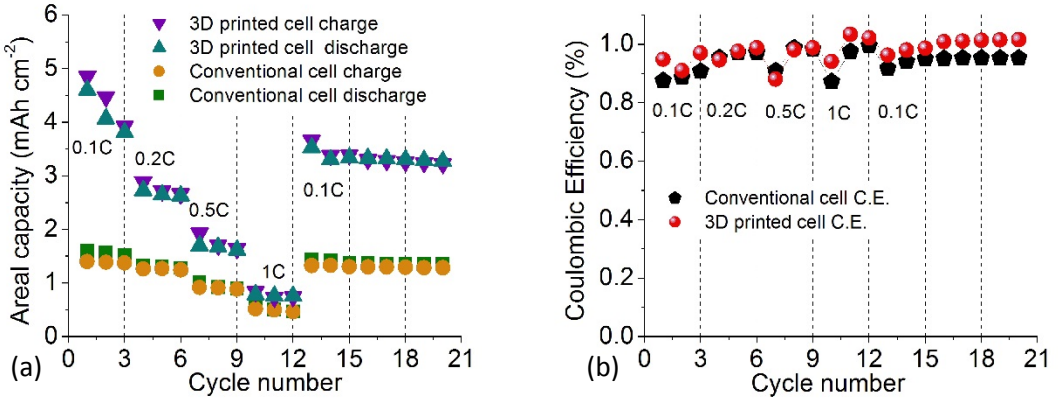

Figure 9. (a) Cycling performance with 0.1C, 0.2C, 0.5C, 1C and 0.1C of 30% SL conventional structure (160 μm) and printed hybrid 3D structure (270 μm), and (b) coulombic efficiency.

3.3.3. Power and Energy Density. In Figure 10, the areal energy and power densities of conventional laminated structures with/without optimized thickness, printed hybrid 3D structures, and other recently reported reference values for 3D structured LIBs are plotted.[8,10,14,21,31-39] As marked with a green square (Figure 10), the energy density and power density of our conventional laminated structure increased as the electrode thickness increased, and the optimal thickness showed a power density similar to that of the cell, which was a half cell with a synthesized LMO nanotube cathode.[8] The hybrid 3D structure LMO batteries, printed on the base layer, showed a 64.6 $J \cdot cm^{-2}$ energy density with a 2.3 $mW \cdot cm^{-2}$ power density. These values are quite outstanding in the aspect of both energy and power density, as compared to other materials systems. In particular, this is very promising when we consider that the theoretical capacity of our LMO is not high enough, as compared to the materials in references $LiCoO_2$,[10,37,38] NiSn-$LiMn_2O_4$,[39] and $LiFePO_4$ [21].

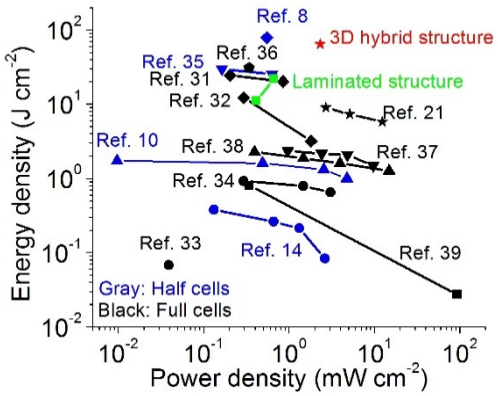

Figure 10. Comparison of the energy and power densities of our conventional laminated structure and a printed hybrid 3D structure, with reference data.

3.3.4. Impedance Analysis. In order to further study the electrochemical behavior of the printed hybrid 3D structure, an electrochemical impedance spectroscopy test was conducted with an optimized conventional structure and a printed hybrid 3D structure.

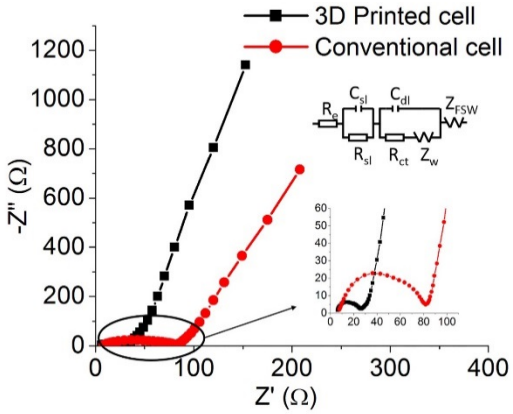

Figure 11. Comparison of impedance with the conventional laminated structure and printed hybrid 3D structure.

The Nyquist plots for the two samples were plotted (Figure 11). The original data were fitted by a circuit diagram model of R(CR)(CRW)W.[40] The high-frequency intercept at the Z' axis corresponded to the ohmic resistance, R_e, which represented the resistance of the electrolyte, and the semicircle in the middle-frequency range indicated the charge transfer resistance, R_{ct}.[41] The Warburg impedance, Z_w, related to a combined effect of the diffusion of li-ions on the electrode/electrolyte interfaces, which corresponded to the straight sloping line at the low-frequency end.[42] It can be seen that both cells had a similar (8 Ω) ohmic resistance, but the semicircle of the printed hybrid 3D structure was smaller than that of the conventional laminated structure. From the fitted impedance parameters, the charge transfer resistance, R_{ct}, of the printed hybrid 3D structure ($R_{ct} \approx 19.6\ \Omega$) was smaller than that of the conventional laminated structure

($R_{ct} \approx 62.6\ \Omega$), indicating that inserting and de-inserting li-ions for the printed hybrid 3D structure were easier than for the conventional laminated structure.[42—44] This means that the hybrid 3D structured electrode greatly enhanced the transport of li-ions.

4. CONCLUSIONS

In this study, a novel hybrid 3D structure electrode is, for the first time, proposed that can achieve high battery performance, such as high areal energy and power density. The proposed structure utilizes the advantages of digital structure (i.e. high aspect ratio) to break through the limitation posed by the conventional laminated structure, which can be applied to large scale battery formats. An extrusion-based additive manufacturing method is used to fabricate this hybrid 3D structure by using the conventional solution, which resolves the typical challenges in preparing solutions for the extrusion process. The results indicate that significantly enhanced areal energy and power densities can be achieved with the hybrid 3D structure. The hybrid 3D structure $LiMn_2O_4$ battery shows superior performances (117.0 $mAh \cdot g^{-1}$ and 4.5 $mAh \cdot cm^{-2}$), in terms of specific capacity and areal capacity. More importantly, compared to the conventional structure, the hybrid 3D structure was more efficient and had much higher li-ions utilization, which presents a new possibility for preparing an electrode with excellent electrochemical performance (64.6 $J \cdot cm^{-2}$ energy density with 2.3 $mW \cdot cm^{-2}$ power density). This work resolved fabrication, solution preparation, and assembly issues for a scaled up 3D battery via the extrusion-based additive manufacturing method. It demonstrated that the proposed 3D structures provide a high specific surface area and quick responses, which are the key

challenges in the area of materials science involving two interfaces (e.g., solid and liquid) and their kinetic reactions. The results can be further applied to other areas related to reactions at interfaces, including other energy storage systems, energy conversion systems, and sensors.

REFERENCES

[1] Lu, L.; Han, X.; Li, J.; Hua, J.; Ouyang, M. A Review on the Key Issues for Lithium-ion Battery Management in Electric Vehicles. *Journal of Power Sources*. 2013, 226, 272-88.

[2] Nitta, N.; Wu, F.; Lee, J.T.; Yushin, G. Li-ion Battery Materials: Present and Future. *Materials Today*. 2015, 18, 252-264.

[3] Arthur, T.S.; Bates, D.J.; Cirigliano, N.; Johnson, D.C.; Malati, P.; Mosby, J.M.; Perre, E.; Rawls, M.T.; Prieto, A.L.; Dunn, B. Three-dimensional Electrodes and Battery Architectures. *Mrs Bulletin*. 2011, 36, 523-31.

[4] Gallagher, K.G.; Trask, S.E.; Bauer, C.; Woehrle, T.; Lux, S.F.; Tschech, M.; Lamp, P.; Polzin, B.J.; Ha, S.; Long, B.; Wu, Q. Optimizing Areal Capacities Through Understanding the Limitations of Lithium-ion Electrodes. *Journal of The Electrochemical Society*. 2016, 163, A138-49.

[5] Park, J.; Li, J.; Lu, W.; Sastry, A.M. Geometric Consideration of Nanostructures for Energy Storage Systems. *Journal of Applied Physics*. 2016, 119, 025101.

[6] Long, J.W.; Dunn, B.; Rolison, D.R.; White, H.S. Three-dimensional Battery Architectures. *Chemical Reviews*. 2004, 104, 4463-92.

[7] Ferrari, S.; Loveridge, M.; Beattie, S.D.; Jahn, M.; Dashwood, R.J.; Bhagat, R. Latest Advances in the Manufacturing of 3D Rechargeable Lithium Microbatteries. *Journal of Power Sources*. 2015, 286, 25-46.

[8] Nishizawa, M.; Mukai, K.; Kuwabata, S.; Martin, C.R.; Yoneyama, H. Template Synthesis of Polypyrrole-Coated Spinel LiMn2O4 Nanotubules and Their Properties as Cathode Active Materials for Lithium Batteries. *Journal of the Electrochemical Society*. 1997, 144, 1923-7.

[9] Cheah, S.K.; Perre, E.; Rooth, M.; Fondell, M.; Hårsta, A.; Nyholm, L.; Boman, M.; Gustafsson, T.; Lu, J.; Simon, P.; Edström, K. Self-supported Three-dimensional Nanoelectrodes for Microbattery Applications. *Nano Letters*. 2009, 9, 3230-3.

[10] Shaijumon, M.M.; Perre, E.; Daffos, B.; Taberna, P.L.; Tarascon, J.M.; Simon, P.; Nanoarchitectured 3D Cathodes for Li-Ion Microbatteries. *Advanced Materials*. 2010, 22, 4978-81.

[11] Long, J.W.; Rolison, D.R. Architectural Design, Interior Decoration, and Three-dimensional Plumbing en Route to Multifunctional Nanoarchitectures. *Accounts of Chemical Research*. 2007, 40, 854-62

[12] Habazaki, H.; Kiriu, M.; Konno, H. High Rate Capability of Carbon Nanofilaments with Platelet Structure as Anode Materials for Lithium ion Batteries. *Electrochemistry Communications*. 2006, 8, 1275-9.

[13] Li, N.; Martin, C.R. A High-rate, High-capacity, Nanostructured Sn-based Anode Prepared Using Sol-Gel Template Synthesis. *Journal of the Electrochemical Society*. 2001, 148, A164-70.

[14] Gowda, S.R.; Leela Mohana Reddy, A.; Zhan, X.; Jafry, H.R.; Ajayan, P.M. 3D Nanoporous Nanowire Current Collectors for Thin Film Microbatteries. *Nano Letters*. 2012, 12, 1198-202.

[15] Chan, C.K.; Peng, H.; Liu, G.; McIlwrath, K.; Zhang, X.F.; Huggins, R.A.; Cui, Y. High-performance Lithium Battery Anodes Using Silicon Nanowires. *Nature Nanotechnology*. 2008, 3, 31-5.

[16] Wu, M.S.; Chiang, P.C.J.; Lee, J.T.; Lin, J.C. Synthesis of Manganese Oxide Electrodes with Interconnected Nanowire Structure as an Anode Material for Rechargeable Lithium ion Batteries. *The Journal of Physical Chemistry B*. 2005, 109, 23279-84.

[17] Gibson, I.; Rosen, D.W.; Stucker, B. Additive manufacturing technologies. *New York: Springer*; 2010.

[18] Adams, J.J.; Duoss, E.B.; Malkowski, T.F.; Motala, M.J.; Ahn, B.Y.; Nuzzo, R.G.; Bernhard, J.T.; Lewis, J.A. Conformal Printing of Electrically Small Antennas on Three-Dimensional Surfaces. *Advanced Materials*. 2011, 23, 1335-40.

[19] Engstrom, D.S.; Porter, B.; Pacios, M.; Bhaskaran, H. Additive Nanomanufacturing–A review. *Journal of Materials Research*. 2014, 29, 1792-816.

[20] Fu, K.; Wang, Y.; Yan, C.; Yao, Y.; Chen, Y.; Dai, J.; Lacey, S.; Wang, Y.; Wan, J.; Li, T.; Wang, Z. Graphene Oxide-Based Electrode Inks for 3D-Printed Lithium-Ion Batteries. *Advanced Materials.* 2016, 28, 2587-2594.

[21] Sun, K.; Wei, T.S.; Ahn, B.Y.; Seo, J.Y.; Dillon, S.J.; Lewis, J.A. 3D Printing of Interdigitated Li-ion Microbattery Architectures. *Advanced Materials*. 2013, 25, 4539-43.

[22] Kim, S.H.; Choi, K.H.; Cho, S.J.; Choi, S.; Park, S.; Lee, S.Y. Printable Solid-state Lithium-ion Batteries: A New Route Toward Shape-conformable Power Sources with Aesthetic Versatility for Flexible Electronics. *Nano Letters*. 2015, 15, 5168-77.

[23] Feilden, E.; Blanca, E.G.T.; Giuliani, F.; Saiz, E.; Vandeperre, L. Robocasting of Structural Ceramic Parts with Hydrogel Inks. *Journal of the European Ceramic Society*. 2016, 36, 2525-33.

[24] Li, W.; Ghazanfari, A.; Leu, M.C.; Landers, R.G. Methods of Extrusion on Demand for High Solids Loading Ceramic Paste in Freeform Extrusion Fabrication. Solid Freeform Fabrication Symposium. 2015, 332–45.

[25] Ahn, B.Y.; Duoss, E.B.; Motala, M.J.; Guo, X.; Park, S.I.; Xiong, Y.; Yoon, J.; Nuzzo, R.G.; Rogers, J.A.; Lewis, J.A. Omnidirectional Printing of Flexible, Stretchable, and Spanning Silver Microelectrodes. *Science.* 2009, 323, 1590-3.

[26] Brodd, R.J. Batteries for Sustainability: Selected Entries from the Encyclopedia of Sustainability Science and Technology. *Springer Science & Business Media.* 2012.

[27] Tang, X.; Lin, B.; Ge, Y.; Ge, Y.; Lu, C.; Savilov, S.V.; Aldoshin, S.M.; Xia, H.; $LiMn_2O_4$ Nanorod Arrays: A potential Three-dimensional Cathode for Lithium-ion Microbatteries. *Materials Research Bulletin*. 2015, 69, 2-6.

[28] Tang, S.B.; Lai, M.O.; Lu, L.; Electrochemical Studies of Low-temperature Processed Nano-crystalline $LiMn_2O_4$ Thin Film Cathode at 55 ^oC. *Journal of Power Sources*. 2007, 164, 372-378.

[29] Lu, D.; Shao, Y.; Lozano, T.; Bennett, W.D.; Graff, G.L.; Polzin, B.; Zhang, J.; Engelhard, M.H.; Saenz, N.T.; Henderson, W.A.; Bhattacharya, P. Failure mechanism for fast-charged lithium metal batteries with liquid electrolytes. *Advanced Energy Materials.* 2015, 5, 1400993.

[30] Leung, K., 2016. First Principles Modeling of Mn (II) Migration above and Dissolution from LixMn2O4 (001) Surfaces. *Chemistry of Materials*.

[31] Gaikwad, A.M.; Whiting, G.L.; Steingart, D.A.; Arias, A.C. Highly Flexible, Printed Alkaline Batteries Based on Mesh-Embedded Electrodes. *Advanced Materials*. 2011, 23, 3251-5.

[32] Nathan, M.; Golodnitsky, D.; Yufit, V.; Strauss, E.; Ripenbein, T.; Shechtman, I.; Menkin, S.; Peled, E.; Three-dimensional Thin-film Li-ion Microbatteries for Autonomous MEMS. *Journal of Microelectromechanical Systems*. 2005, 14, 879-85.

[33] Min, H.S.; Park, B.Y.; Taherabadi, L.; Wang, C.; Yeh, Y.; Zaouk, R.; Madou, M.J.; Dunn, B. Fabrication and Properties of a Carbon/polypyrrole Three-dimensional Microbattery. *Journal of Power Sources*. 2008, 178, 795-800.

[34] Kotobuki, M.; Suzuki, Y.; Munakata, H.; Kanamura, K.; Sato, Y.; Yamamoto, K.; Yoshida, T. Effect of Sol Composition on Solid Electrode/solid Electrolyte Interface for All-solid-state Lithium ion Battery. *Electrochimica Acta*. 2011, 56, 1023-9.

[35] Mazor, H.; Golodnitsky, D.; Burstein, L.; Gladkich, A.; Peled, E. Electrophoretic Deposition of Lithium Iron Phosphate Cathode for Thin-film 3D-microbatteries. *Journal of Power Sources*. 2012, 198, 264-72.

[36] Kim, H.; Proell, J.; Kohler, R.; Pfleging, W.; Pique, A.; Laser-Printed and Processed LiCoO2 CathodeThick Films for Li-ion Microbatteries. *Journal of Laser Micro/Nanoeng*. 2012, 7, 320-5.

[37] Yoshima, K.; Munakata, H.; Kanamura, K. Fabrication of Micro Lithium-ion Battery with 3D Anode and 3D Cathode by Using Polymer Wall. *Journal of Power Sources*. 2012, 208, 404-8.

[38] Bates, J.B.; Dudney, N.J.; Neudecker, B.; Ueda, A.; Evans, C.D. Thin-film Lithium and Lithium-ion Batteries. *Solid State Ionics*. 2000, 135, 33-45.

[39] Pikul, J.H.; Zhang, H.G.; Cho, J.; Braun, P.V.; King, W.P. High-power Lithium ion Microbatteries from Interdigitated Three-dimensional Bicontinuous Nanoporous Electrodes. *Nature Communications*. 2013, 4, 1732.

[40] Mohamedi, M.; Takahashi, D.; Uchiyama, T.; Itoh, T.; Nishizawa, M.; Uchida, I. Explicit Analysis of Impedance Spectra Related to Thin Films of Spinel $LiMn_2O_4$. *Journal of Power Sources*. 2001, 93, 93-103.

[41] Guo, D.; Chang, Z.; Tang, H.; Li, B.; Xu, X.; Yuan, X.Z.; Wang, H. Electrochemical Performance of Solid Sphere Spinel $LiMn_2O_4$ with High Tap Density Synthesized by Porous Spherical Mn_3O_4. *Electrochimica Acta*. 2014, 123, 254-9.

[42] Zhang, S.S.; Xu, K.; Jow, T.R. EIS Study on the Formation of Solid Electrolyte Interface in Li-ion Battery. *Electrochimica Acta*. 2006, 51, 1636-40.

[43] Zhuang, Q.C.; Wei, T.; Du, L.L.; Cui, Y.L.; Fang, L.; Sun, S.G. An Electrochemical Impedance Spectroscopic Study of The Electronic and Ionic Transport Properties of Spinel $LiMn_2O_4$. *The Journal of Physical Chemistry C*. 2010, 114, 8614-21.

[44] Cho, S.; Chen, C.F.; Mukherjee, P.P. Influence of Microstructure on Impedance Response in Intercalation Electrodes. *Journal of The Electrochemical Society*. 2015, 162, 1202-1214.

II. MACRO-/MICRO-CONTROLLED LITHIUM-ION 3D BATTERY VIA 3D PRINTING AND ELECTRIC FIELD

ABSTRACT

This paper presents a new concept for making battery electrodes that can simultaneously control macro-/micro-structures and help address current energy storage technology gaps and future energy storage requirements. Modern batteries are fabricated in the form of laminated structures that are composed of randomly mixed constituent materials. This randomness in conventional methods can provide a possibility of developing new breakthrough processing techniques to build well-organized structures that can improve battery performance. In the proposed processing, an electric field (EF) controls the microstructures of manganese-based electrodes, while additive manufacturing controls macro-3D structures and the integration of both scales. The synergistic control of micro-/macro-structures is a novel concept in energy material processing that has considerable potential for providing unprecedented control of electrode structures, thereby enhancing performance. Electrochemical tests have shown that these new electrodes exhibit superior performance in their specific capacity, areal capacity, and life cycle.

1. INTRODUCTION

Although remarkable advances have been made in lithium ion batteries (LIBs) during the past several decades, higher energy and power densities are still required for

portable devices, transportation, and stationary applications. [1-3] Even though gravimetric capacity is one of the most utilized metrics in measuring LIB performance, the amount of materials in an electrode actually determines the energy and power of the LIB. Thus, the requirement for a high tap density is of considerable importance for various applications. The conventional strategy towards a high tap density is to add more material to a higher packing density. While an increase in the volume fraction of an active material improves the transport of lithium ions and electrons on the solid phase, it impedes the transport of lithium ions in an electrolyte. For this reason, increasing packing density is not always desirable. An alternative strategy would be to add more materials by increasing the thickness of the electrodes. This approach, however, limits the transport of ions and electrons, resulting in poor power performance and inefficient utilization of materials. The goal of this paper is to present a means for circumventing these challenges to conventional structures through a new concept for electrode structures, based on macro-micro-controlled three-dimensional (3D) electrodes that can facilitate the transport of the species. An optimized 3D structure permits a facile transport of ions, via a short diffusion path with an enhanced electrochemical reaction, through a higher interface area. (Figure. S1). For this reason, 3D structured electrodes are considered to have a huge potential for improving battery performance. [3-7]

Recently, an extrusion-based additive manufacturing process has been proved to provide many advantages compared to other additive manufacturing technologies, such as aerosol jet and ink jet printing. Not only is it inexpensive and flexible enough to fabricate more complex geometry designs, but it can be applied to a wider selection of materials with a high mass loading. [8, 9] In particular, the extrusion-based additive

manufacturing technique appears to be a very promising method for fabricating 3D battery electrode structures. [5, 7, 10-13] Unfortunately, the preparation of a proper composition of paste for the extrusion process is rather demanding because of the need to prevent clogging of the nozzles, promote a bond between each filament, and keep a controlled feature geometry after extrusion. [14-16] In addition, for LIB applications, the chemical components in a paste can significantly affect battery performance. For instance, additional binders for improving mechanical integrity would decrease ionic and electronic conductivity.

Another approach that could improve battery performance is to deploy well-organized individual particles in an electrode. Modern batteries are fabricated by casting randomly mixed slurries onto current collectors. These randomly distributed particles (active particles or additive particles) easily agglomerate to form weak spots that can cause a bottleneck in the electrochemical reaction. Also, particles can become an isolated group within the network and, consequently, this isolated group does not perform its essential duty, but hinders the transport of species instead. Further, because a random structure may create a long path for transport, a well-organized structure will provide better responses and superior performance, as compared to a randomly distributed structure. Battery electrodes, with controlled structures at the micro/nano level (such as nanotubes and 3D nanostructures), have been synthesized based on a top-down approach that includes the use of lithography tools, but these are expensive and time-consuming.[17-25] An opposite approach is to fabricate structures, via a bottom-up approach using chemical or physical reactions. In particular, utilizing an electric field (EF) is an effective approach because it is easily implemented and it provides a long-

range effect of electrostatic interactions.[26-29] It has been found that an EF could efficiently manipulate particles in a colloidal slurry, including a “chain effect” by moving and rotating particles in a slurry under an external EF.

This paper details a new innovative approach for fabricating 3D structured electrodes, in which three-dimensional features can be simultaneously controlled at the macro-micro-levels (which the conventional manufacturing process cannot do). The proposed process integrates the extrusion-based additive manufacturing process for macro-control and an EF for micro-control. This is a new unique method for manufacturing battery electrodes that has the potential for providing synthetic control of materials architectures, such as particle network, geometries, and integration. This could lead to transformational enhancement of key energy storage parameters that include capacity, energy density, and life cycle.

2. RESULTS

2.1. SOLIDS LOADING IMPACT

Constituent materials should be organized to promote high conductivity, robust mechanical strength, a high specific area, and superior battery performance. To achieve these, two aspects must be simultaneously considered, including shaping the structure and the corresponding battery functionality. To shape target structures, via an extrusion-based additive manufacturing process, many factors should be considered, including the impact of the electrode’s constituent materials, solids loading (SL) (volumetric ratio of solids in a solution) to prevent clogged nozzles, bonding strength between each filament,

and features to be retained after extrusion. These features can all be characterized by two key physical properties of paste, viscosity and shear stress. For battery function, a large amount of active material would contribute to higher capacity, together with appropriate amounts of a conductive material and binder. However, excessive amounts of an additive material could interfere with species transportation. To understand and determine the fundamental requirements for the slurry, first, the effect of SL on battery fabrication and performance were studied based on the conventional structures without any geometric control. Six $LiMn_2O_4$ (LMO) pastes, with different SLs, were prepared from 10% to 35% (in 5% increments, Table S1). Rheology test results (Figure 1a) indicated that all of the pastes exhibited a shear-thinning behavior, implying that they could be extruded and controlled by the extrusion process. The effect of SL was that the viscosity increased with increasing SL, and the 30% and 35% SL pastes (10^3 Pa.s and 10^5 Pa) showed two orders of magnitude higher in viscosity and stress than the 10% SL paste did (10 Pa.s and 10^3 Pa). This high viscosity was related to the prevention of the collapse of a 3D extruded structure, which will be discussed later.

To determine the relationship between the SL and mass loading (ML) (weight of active materials in a unit electrode foot area), conventional structures with 160 μm electrode thickness were examined. As shown in Figure 1b, a linear relationship was observed between paste SL and electrode ML. By increasing the SL from 10% to 35%, the ML increased 2.8 times and achieved 0.028 g/cm^2. For LIB applications, in general, a higher ML was required to increase energy density. When the structure was too dense, however, the transport of lithium ions in the electrolyte was hindered, as described earlier. Therefore, there is an optimal SL due to the trade-off between the transport

properties of the solid and electrolyte phases. Figures 1c and 1d show battery cycling performance with different SLs. A 10% SL produced the lowest mass loading (0.01 g/cm^2) and a very low specific capacity (40 mAh/g). This poor specific capacity (from the 10% SL) could be caused by poor percolation of the electrode (Figure S2c), while the high SL paste could cast a dense electrode (Figure S2d). As evidenced, Figure S1b shows a high charge transfer resistance (200 Ω) of the 10% SL cast electrode, compared to other high SL cases. The 30% SL showed a maximum specific capacity of 98 mAh/g, while the 35% SL showed a lower capacity of 85 mAh/g. For coulombic efficiency (Figure 1d), all samples exhibited good performance. A quick change in the coulombic efficiency was observed when the C-rate changed, but it quickly stabilized. This was caused by a residual concentration gradient inside particles caused by the previous cycling. In summary, by considering both paste properties and battery performance, the 30% SL was selected for the fabrication of macro-micro controlled electrodes (to be discussed later).

2.2. MACRO-CONTROLLED 3D STRUCTURE

The proposed extrusion-based additive manufacturing process is shown in Figure 2. Figures 2a and 2c depict the actual system and a schematic diagram, respectively, while Figures 2b and 2d show the electric field process (described in the next section). This extrusion process was used to fabricate a macro-controlled 3D structure (a hybrid 3D structure composed of a digital structure on a conventional laminated structure). Figure 2e shows one example of printed 3D electrodes. A macro-controlled hybrid 3D structure was systematically studied in the authors' previous work [5]. In this paper, a verification test was first conducted to compare the conventional and micro-macro-controlled structures. This macro-controlled 3D structure was fabricated by adding an

interdigitated 3D structure on the top of a conventional laminate structure (160 μm), making the total electrode thickness 270 μm. The thickness of the conventional cell used for the comparison was also 270 μm. Then, each cell was cycled at rates of 0.1C, 0.2C, 0.5C, 1C, and 0.1C, with five cycles per each C-rate.

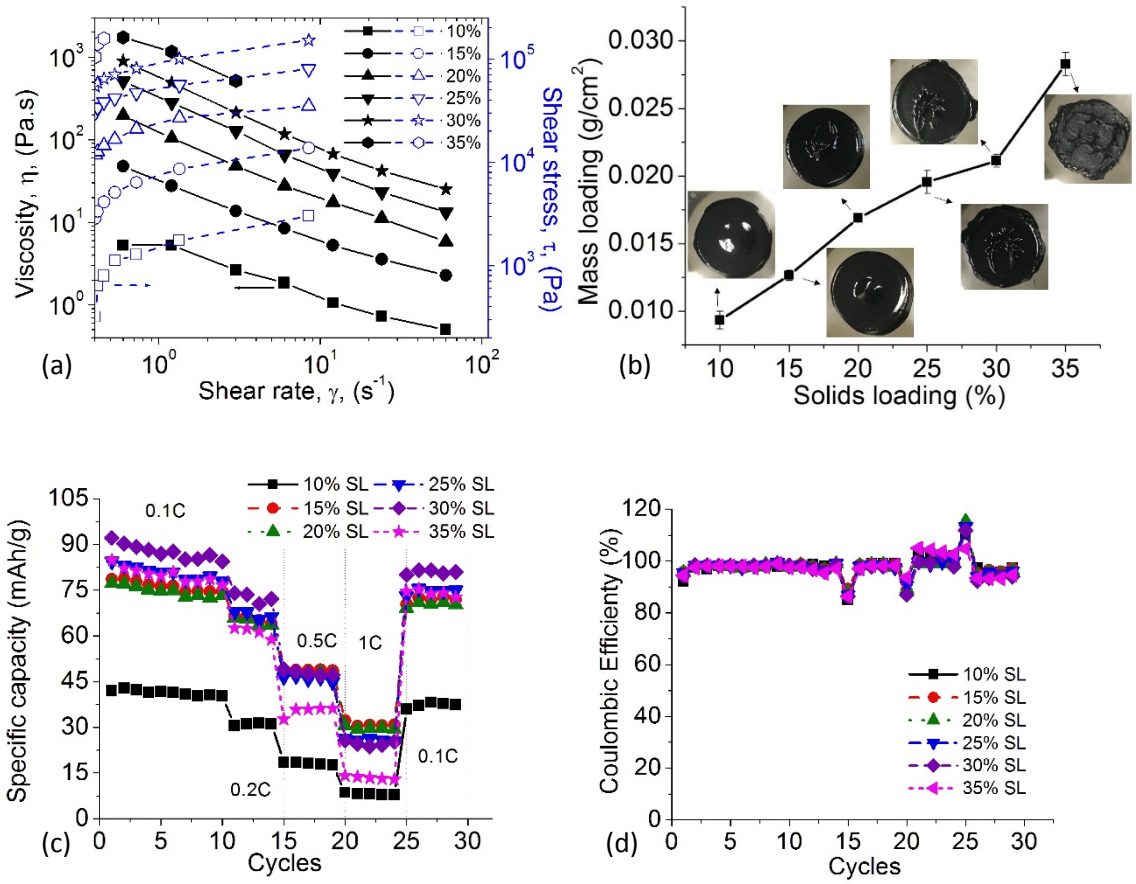

Figure 1. Solids loading (SL) impact on (a) paste rheology, (b) mass loading, (c) specific capacity, and (d) coulombic efficiency in a range of 10% SL to 35% SL.

As shown in Figure 3, the cycling test showed that the areal capacity of the macro-controlled 3D structure reached 3.1 mAh/cm^2, which was 1.7 times higher than that of the conventional structure. In addition, as expected, the capacity reduced at high

C-rates due to high ohmic resistance. For coulombic efficiency, in general, both structures had a stabilized value, but a small variation in C-rates after the initial formation cycle (shown in Figure 3b). During the first five cycles, in particular, the structures showed a lower coulombic efficiency. This was related to chemical side reactions during the formation cycle. For instance, like the Solid Electrolyte Interphase (SEI) layer in the anode, a thin film formed on the cathode particles' surface, called Solid Permeable Interface, SPI layer. In general, this process consumes the active lithium ions and solvents and causes gas evolution that builds up pressure inside the cell, causing significant capacity fade. For this reason, the inside of the battery is not stable and might show a lower coulombic efficiency during the first few cycles. This phenomenon was also observed during the first few cycles in our previous experiments [5].

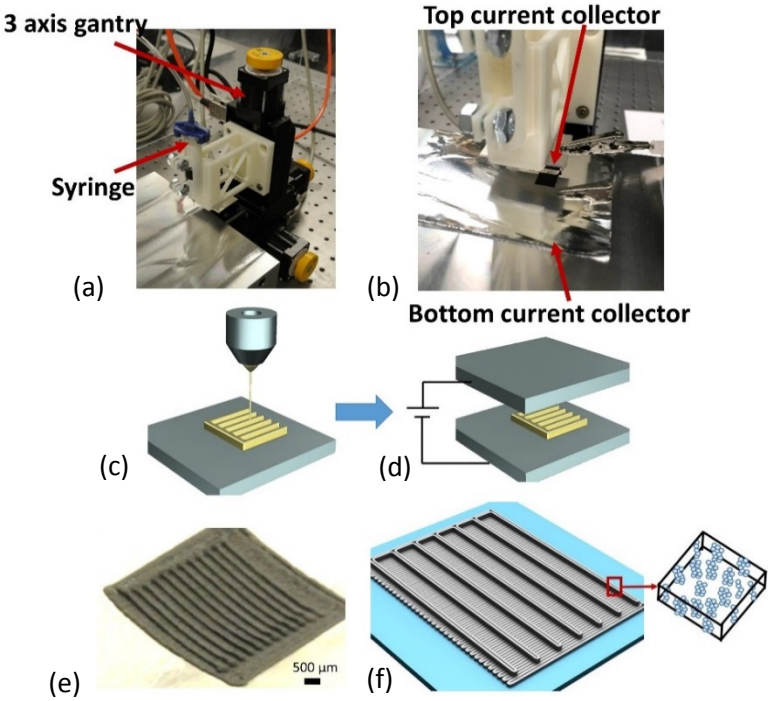

Figure 2. Illustration of (a and c) additive manufacturing system, (b and d) electric field treatment process, and (e and f) macro-micro controlled structure.

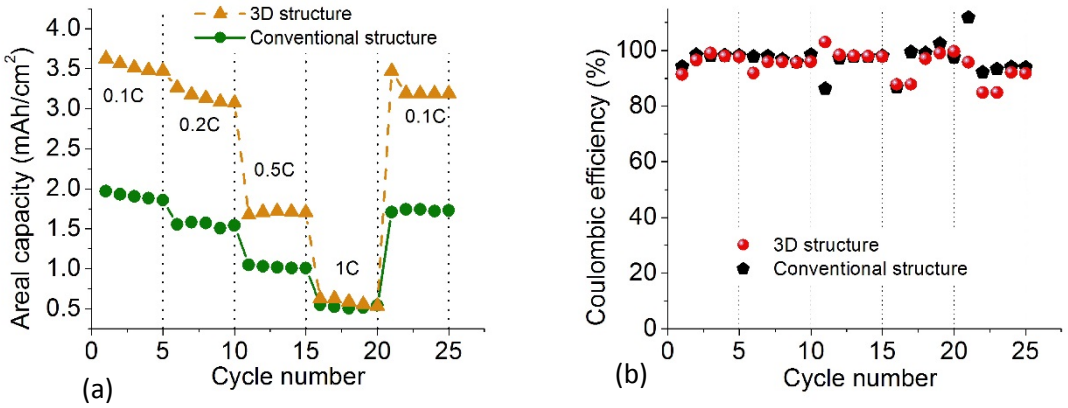

Figure 3. Cycling performance of a conventional structure and macro-controlled 3D structure (a) areal capacity and (b) coulombic efficiency.

As described earlier, maintaining a 3D structure after extrusion is critical for gaining the benefits of the structure. In this work, to prevent the collapse of an extended 3D structure, a hot plate (HP) was used as an external heating source to accelerate drying. Figure 4 shows cross sections of two electrodes, without (Figure 4a) and with (Figure 4b) an HP. As shown in Figure 4a, the 3D structure without the HP did not keep the desired interdigitated structure but collapsed into an uncontrolled shape. The contour plots, marked on the images, represented the boundaries of each electrode and clearly showed the differences in the final fabricated structures. To contrast them, each line was overlapped in those figures and, when the two electrodes were compared by ImageJ software, a 29% difference was measured between the contour lengths. By considering the same length in the plane, this meant that a 29% reduction in the outer surface area occurred because of the collapse. This 3D structure collapse was related to the drying speed of the paste. When it was naturally dried, without an HP, the collapse happened very slowly in the air (i.e., within approximately 6 to 10 hours), but with an HP, the electrodes could be partially dried and solidified within 1 minute, and dried completely

within 10 minutes. Thus, the use of an HP (or another type of heating source) is a good option for accelerating the drying process during fabrication to construct a well-controlled 3D structure.

2.3. MICRO-CONTROLLED STRUCTURE

As described earlier, a well-ordered internal structure is another way to enhance battery performance. The remaining question, concerning materials processing, is how to fabricate an electrode with a controlled internal structure. In this work, an EF was used. Figures 2b and 2d show the setup used for processing by applying an EF to create organized nanostructures in an electrorheological fluid, composed of particles dispersed in a slurry. The dispersed particles tend to line up and form a chain parallel to the applied EF. Such behavior can be attributed to electric polarization interaction, a pairwise dipolar interaction between particles. Particles, with the same polarization direction, will repel each other if they remain on a plane that is perpendicular to the EF, but the interaction becomes attractive when the two particles shift and are relative to each other by one radius. [26-29] Figures 5a and 5b show a simple demonstration of this chaining process for battery materials. A slurry of LMO particles in an N-methyl-2-pyrrolidone solvent (NMP) was cast on a glass substrate, and then an EF was applied, along the vertical direction (as shown in the figure). The images were first captured by a stereo microscope (Amscope Inc.) while the particles were randomly distributed on a glass substrate without an applied EF (Figure 5a). Then, when an EF was applied, the particles moved toward the current collector and, finally, rearranged as “chains” (Figures 5b and S3).

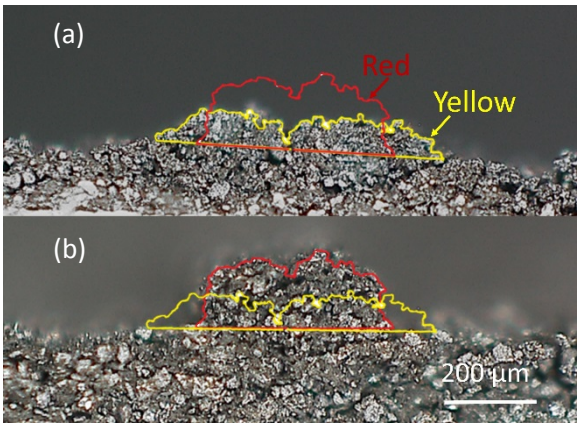

Figure 4. Effect of a hot plate on electrode geometry: (a) without a hot plate and (b) with a hot plate. Each contour plot represents the boundary of the structure. For comparison, the contour plots are overlapped, as shown in both (a) and (b) above.

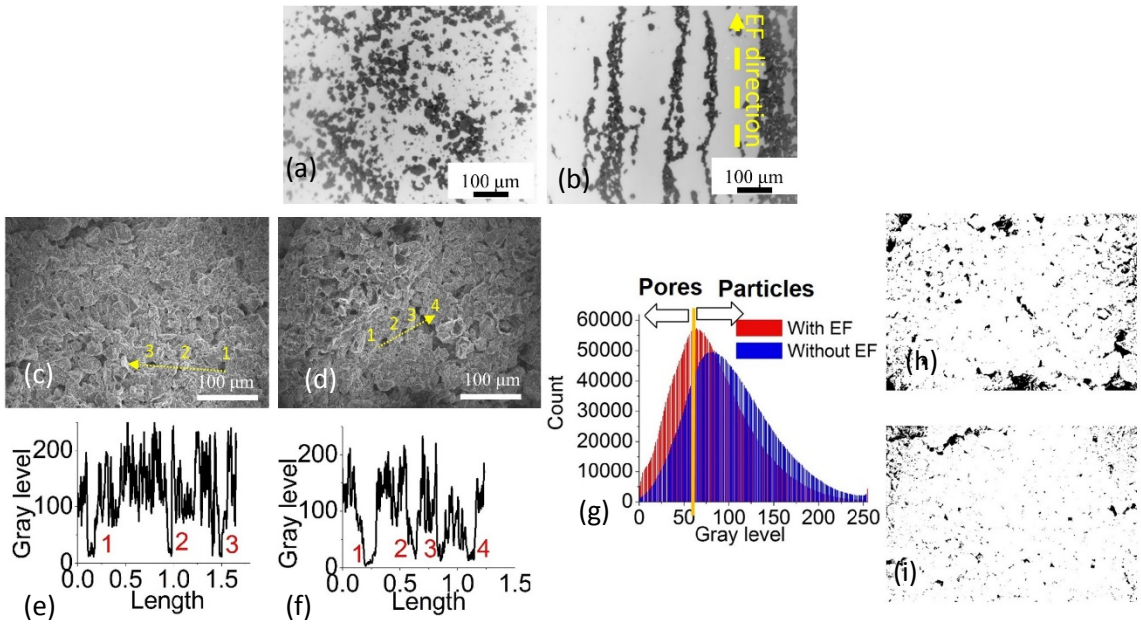

Figure 5. Effect of an electric field on LMO powder (a) without EF and (b) with EF. SEM images of electrodes (c) with EF and (d) without EF, Gray level profiles (e, f) of the lines shown in the SEM images, Gray level distribution (g) of two samples, and Pore distribution after an adjustment of color threshold for the electrodes (h) with EF and (i) without EF.

Although these results confirmed the responsive behavior of battery materials to an EF, the viscosity of slurry for practical battery electrodes was high. One important

question that needed to be answered concerned the mobility of particles in high viscosity slurry. To answer this question, conventional structure electrodes were fabricated with and without an EF. To compare these electrodes, the Brunauer–Emmett–Teller (BET) test was administered for surface area, Scanning Electron Microscopy (SEM) analysis was conducted for surface morphology, and X-Ray Diffraction (XRD) measurements were made for microstructure orientation. The surface area of particles in electrodes is one of the critical factors that determine battery performance. From the BET test, it was found that the surface area of the electrode under an EF was found to be about twice that of the electrode without EF. The measured surface areas were 3.5 m^2/g and 1.7 m^2/g, respectively. Next, to visualize the difference, SEM images with different orientations were taken. As shown in Figures 5c, 5d, S4, S5, it was difficult to distinguish them by appearance alone. For further analysis, a graphical interpretation was made by using ImageJ software (a common approach for porosity analysis) [30]. For this, the images were cropped to remove label bars, and adjusted to maximum and minimum brightness and contrast. To identify the pores, a threshold value of 70 gray level was selected by observing the sharp drop in line profiles, which represented the pore boundary (Figures 5c, 5d, 5e, 5f). This value was confirmed with a dozen of pores and then used to measure the areal porosity of the whole binary images (Figure 5g). This analysis showed that the electrode with an EF had more porosity (8.5%) than the electrode without EF (3.9%), as illustrated in Figures 5h and 5i. This result was consistent with the conclusion obtained from the BET test.

Another interesting piece of evidence, concerning the responsive behavior of battery materials to an EF, was obtained from an XRD measurement. The XRD test was

performed for electrodes without EF and with EF (at different applied voltages) at different drying times. A maximum applied voltage (10 kV) was selected that would avoid sparks during the process that could cause damage to the electrodes. For comparison, half of the maximum voltage (5 kV) was also applied. Additionally, based on a hypothesis that drying time will affect the microstructure, different drying times (3 h and 6 h) were compared. When the applied EF was turned off before the electrode was fully dried, a Brownian motion might break the formed structures because of the EF effect. Based on a rough estimation, the electrodes were partially dried in 3 hours and fully-dried in 6 hours. On the other hand, when an HP was used, the drying time was 1 minute for half drying and 10 minutes for full drying.

For XRD measurement, each sample was tested based on two forms, including a form of the whole electrode itself and as the powder after breaking the same electrode. Samples with 0 V without an HP were used as the control group. The peaks corresponding to the control group (shown in Figure 6a) are well matched with the reported values in the literature [31,32]. At a low voltage (5 kV) with a short drying time (3 h) and 0V with HP samples, the peaks were the same as the control sample. However, the peaks in <111>, <311>, and <222> were missing for long periods of time from electrode samples with high applied voltages. A possible reason for this was a preferred orientation of the particles under the applied EF. In order to confirm this, the measured electrodes were broken into a powder and measured by XRD again. For all samples, the missing peaks showed up again (Figure 6b), indicating that there was no longer any preferred orientation. These series of XRD measurements proved that when the applied

EF was too small, or the drying time was too short, the EF effect could not be expected. This supported the proposed reason for the missed peaks above.

Next, four samples with conventional structures (no EF, 5 kV/3 h, 5 kV/6 h, and 10 kV/3 h) were assembled into half-cells to examine the effect of EF on battery performance. As shown in Figures 6c and 6d, the electrodes with 10 kV/3 h and 5 kV/6 h showed higher capacities than those of the electrodes without an EF and with 5 kV/3 h. Hence, the samples effectively-treated by an EF (Figure 6c) showed improved results. For the coulombic efficiency (Figure 6d), all of the samples showed similar values of around 95% to100%.

2.4. MACRO-MICRO CONTROLLED STRUCTURE

As the final goal, both macrostructure (additive manufacturing process) and microstructure (electric field process) were controlled simultaneously. For the macrostructure control, a 270 μm hybrid 3D electrode, which showed the best performance in the previous section, was constructed. Next, an EF with 10 kV was applied to those hybrid electrodes. For comparison, some of the hybrid electrodes were not applied with an EF. Then, the cells were cycled at different C-rates (0.1C, 0.2C, 0.5C, 1C, and 0.1C), with five cycles per each C-rate (shown in Figure 7a). All samples showed stable performance, along with slight decreases in capacity. As expected, the capacity was reduced at high C-rates due to high ohmic resistance. However, the sample with an EF showed greater areal capacity than the sample without an EF did, even when C-rates were high. For instance, the areal capacity of the sample with an EF (0.76 $mAh.cm^{-2}$) was about 1.21 times that of the sample without EF (0.63 $mAh.cm^{-2}$) at 1C. After returning to

the low 0.1C, both cells showed stable performances, but the one with an EF (3.38 mAh cm^{-2}) showed 7% more areal capacity than the one without EF (3.18 mAh $cm^{-2)}$. The columbic efficiency of both samples (with and without EF) was stabilized after a small drop between different C-rates, but they showed similar values, as shown in Figure 7b.

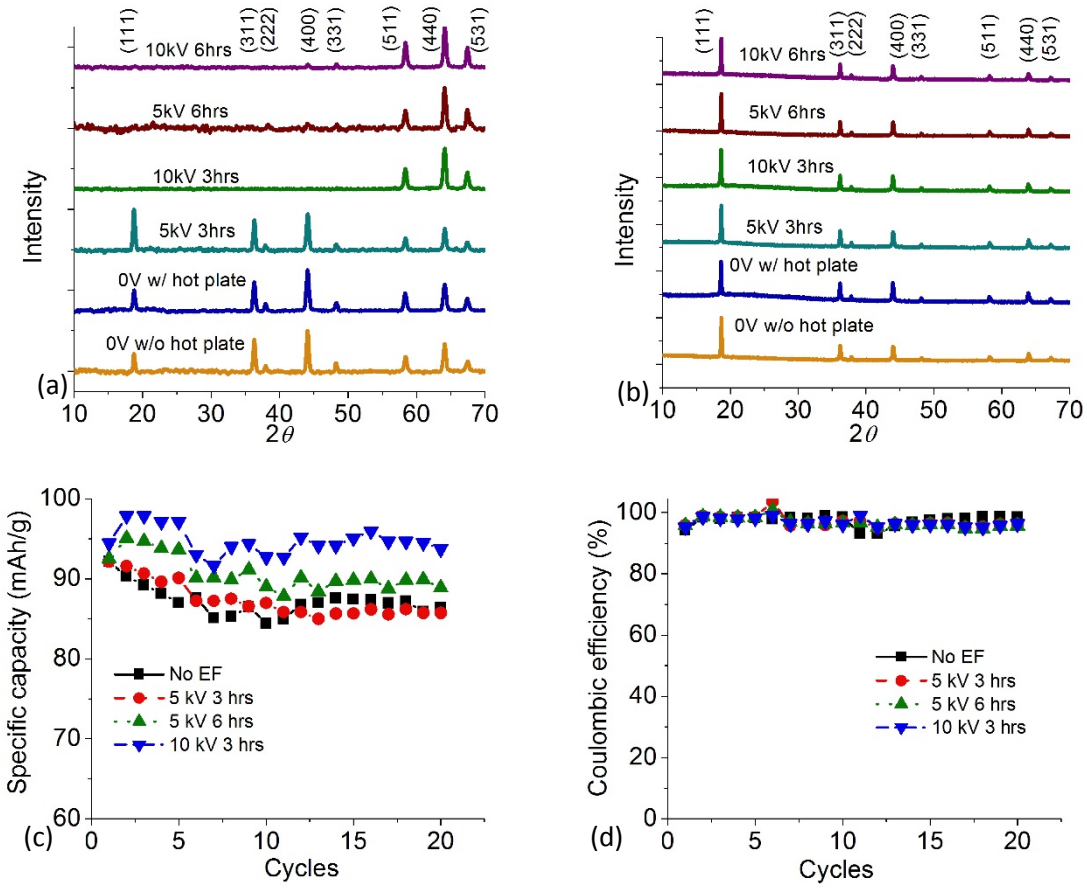

Figure 6. XRD results obtained from electrodes under different conditions: (a) electrode film samples and (b) electrode power samples, and (c) and (d) cycling performance with different conditions.

Nyquist plots were made for both samples (Figure 7c). The original data were fitted with a circuit diagram model of R(CR)(CRW)W.[33] The high-frequency intercept at the Z′ axis corresponded to the ohmic resistance, R_e (which represented the resistance

of the electrolyte), and the semicircle in the middle-frequency range indicated the charge transfer resistance, R_{ct}.[34] The Warburg impedance, Z_w, was related to a combined effect of the diffusion of lithium ions on the electrode/electrolyte interfaces, which corresponded to the straight sloping line at the low-frequency end.[35] It can be seen that both cells had a similar (7 Ω) ohmic resistance, but the semicircle of the EF-processed 3D structure was smaller than that of the 3D structure without an EF. From the fitted impedance parameters, the charge transfer resistance, R_{ct}, of the 3D printed and EF processed 3D structure ($R_{ct} \approx 100$ Ω), was smaller than that of the 3D printed without the EF ($R_{ct} \approx 150$ Ω). This indicated that the (de)intercalation process for the EF-processed 3D structure was easier than that for the sample without the EF.[35-37] This indicated that the EF-processed electrode greatly enhanced the transport of lithium ions.

The cyclic voltammetry curves with EF (Figure 7d) and without EF (Figure 7e) indicated that both of the samples had the same polarization values of around 3.8, 4.1, and 4.2 V, which was reasonable because the EF process did not affect the chemical properties (Figure 6b). In addition, when the two different scan rates (from 0.025 to 0.25 mVs^{-1}) were compared, both samples had similar shapes when the scan rate was lower than 0.25 mVs^{-1}. The sample with an EF showed a more symmetrical shape at a high scan rate, which meant that the sample with an EF had better rate capability than the sample without EF did. As shown in Figure 7f, the voltage profile of four different configurations of the 3D printed batteries with the same thickness of 270 μm were compared; they included (1) no controlled structure (i.e., without HP and EF); (2) macro-controlled structure (i.e., without EF); (3) micro-controlled structure (i.e., without HP); and (4) macro-micro controlled structure (i.e., with HP and EF).

As discussed earlier, the process using an HP improved the external 3D structure morphology, while the EF process increased the particle order inside the electrode. The sample with an HP provided 30% more surface area than the sample without HP did and, similarly, the applied EF doubled the surface area of the electrode. For the battery responses for those cells, first, four samples showed a very similar voltage drop, indicating that the ohmic drop was not significantly affected by the fabrication process. Next, as compared to the conventional structure (1.8 mAh/cm^2), the capacity increased to 2.8 mAh/cm^2 with additive manufacturing (no controlled structure). However, this capacity was lower than that of the macro-controlled structure with 3.1 mAh/cm^2. By micro-controlling, the capacity increased farther to 3.3 mAh/cm^2, indicating that micro-control had more impact than macro-control did. Finally, the macro-micro controlled structure showed the best performance (3.5 mAh/cm^2) by simultaneously utilizing the advantages of a 3D structure and electronically ordered particles.

3. DISCUSION AND CONCLUSIONS

A well-known disadvantage of the additive manufacturing process is that the three-dimensional printing process takes a long time to mass-produce filaments printed in the x-y direction, and then to print layer-by-layer in the z-direction. Thus, compared to slurry casting (casting any thickness at one time), the time required for printing the structure will increase with increased cell area, thickness, and structure resolution.

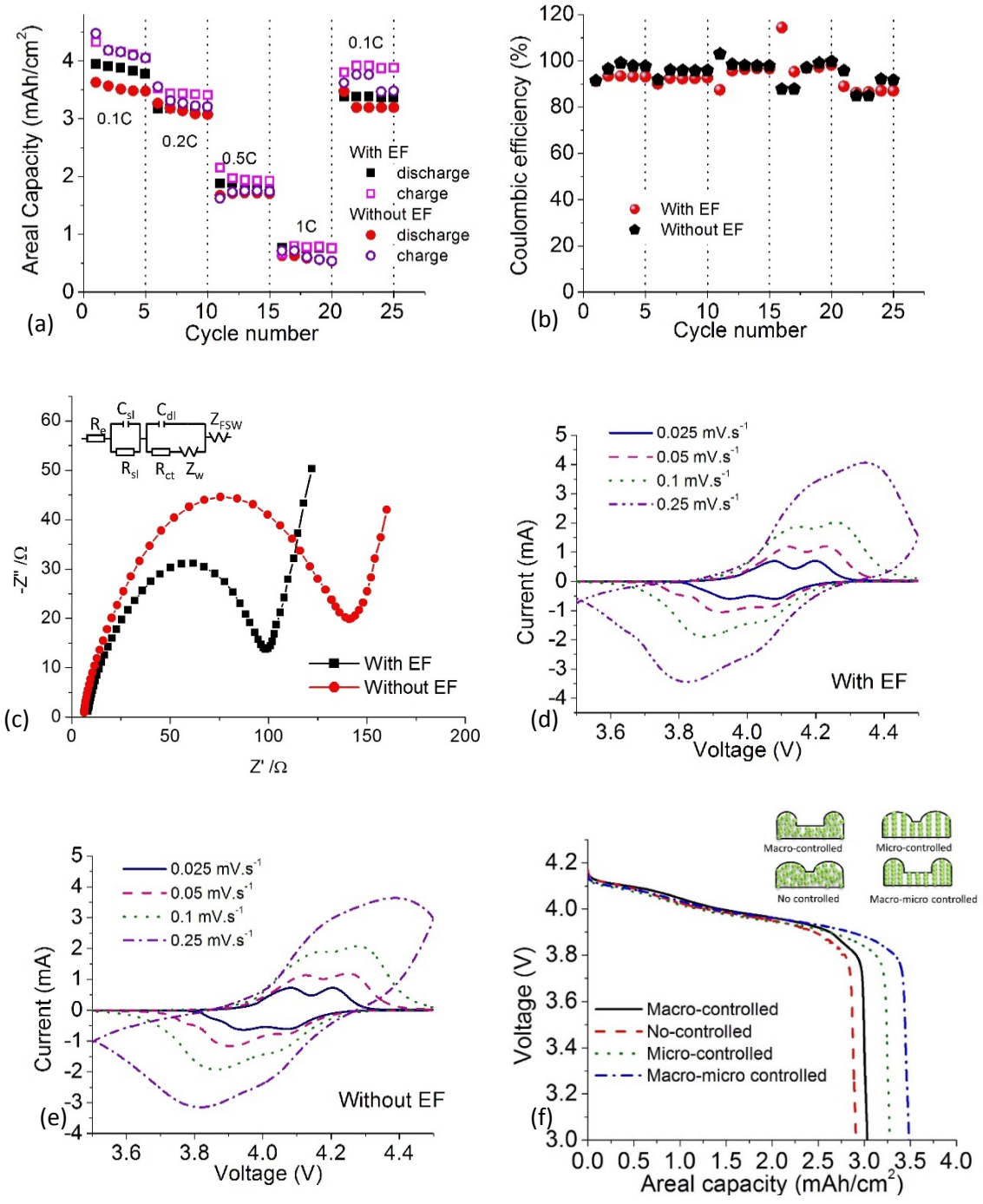

Figure 7. Comparisons of the performance of structures with and without EF of (a) cycling with 0.1C, 0.2C, 0.5C, 1C, and 0.1C; (b) coulombic efficiency; (c) impedance and cyclic voltammetry; (d) with EF; and (e) without EF; (f) voltage profile comparison of the four configurations.

For example, from our experimental setup (without applying an electric field), a 270 μm thickness, with a 1x1 cm^2 area on a laboratory scale, took 5 minutes for casting, while the extrusion-based printing required about 10 minutes with a 200 μm nozzle size. On the other hand, post-processing was more important and time-consuming from the point of view of the entire manufacturing processing time. Typical casting electrodes required a long drying time in an oven (usually overnight), at 100-130 °C. In contrast, our printing system that contained a heated substrate of 120 °C allowed the samples to be dried quickly within 10 minutes. To compare the two processes, thermogravimetric analysis was performed at 120 °C with a small piece of the 3D sample (50 mg) and a cast sample (30 mg). As shown in Figure 8, the cast sample took about 40 minutes to dry, while the printed sample did not lose weight during the measurement. This clearly demonstrated that our proposed additive manufacturing method can save more time during the post-processing phase than the conventional method can.

This study proposes a novel multi-scale process to fabricate 3D structure electrodes via combining additive manufacturing and an electric field process. The influence of the processing parameters on a particle network has been clarified in order to improve the quality of electrode structures. The effects of solids loading on paste properties and battery performance were carefully studied initially. Higher SLs increased the paste viscosity and stress that were needed to control the macro-shape after extrusion via extrusion-based additive manufacturing, and to increase mass loading. Based on these two sets of experiments, the 30% SL paste was found to be the optimal loading with high viscosity (10^3 Pa.s) and high specific capacity (92 mAh/g). The macro-controlled 3D structure showed that the hybrid 3D structure could attain a high areal capacity (3.1

mAh/cm^2) and double the areal capacity (as compared to a conventional laminated structure). Further, the effect of using a heating source during printing was studied. It was found that the heating source accelerated solidification of a printed electrode and then helped to retain its shape before solidification was complete. It was also observed that the heating source did not affect the chemical in the electrode materials, and the well-controlled shape was able to improve battery performance (approximately 60%) by increasing the surface area of the electrode, as compared to the conventional structure (Fig. 3a).

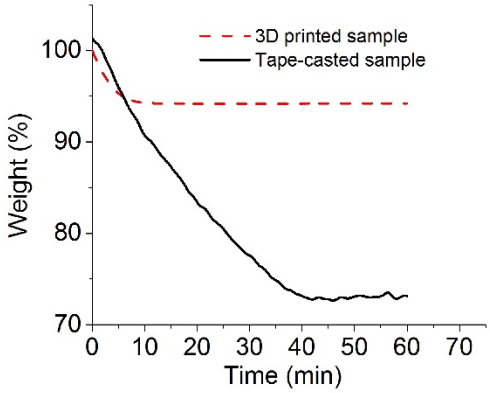

Figure 8. Thermal gravity tests of the 3D printed sample and conventional cast sample.

For the microstructure aspect, the applied EF ordered the internal structure of the electrode through a “chain effect” that manipulated particles, so that the surface of the electrode increased approximately 200%. The effect of the applied EF was also systematically studied with different EFs and duration times. It was observed that the maximum EF (10 kV) with 3 hours, or a medium EF (5 kV) with 6 hours, would cause the particles to be in a preferred orientation order. Electrochemical performance tests of

the samples showed that a higher EF with rapid drying would improve battery performance by approximately 7% (Figure 6).

Finally, a macro-micro-controlled 3D structure was fabricated, and comparisons were made for battery performances between 3D structure samples with no EF and a maximum EF with an HP. The results indicated that the performance of a macro-controlled 3D structure could be further improved via manipulating the microstructures. Further characterization, including impedance and cyclic voltammetry tests, indicated that the sample with an EF enhanced the transport of lithium ions and had a better capability rate than the sample without an EF did. Voltage profiles from the four different fabrication conditions showed that the macro-micro-controlled structure showed 21%, 16%, and 7% more areal capacity than a structure with no control, a macro-controlled structure, and a micro-controlled structure, respectively (Fig. 7f). The proposed control of extruded structures, with a well-organized distribution of energy materials, demonstrated more superior properties and advantages than structures with randomly distributed materials.

4. METHODS

4.1. MATERIAL PREPARATION

A $LiMn_2O_4$ (LMO) paste was used to fabricate the electrodes. The paste was prepared by first mixing 85.5 wt% of LMO powder (MTI, 13 μm) with 6.5 wt% of carbon black (CB, Alfa Aesar) and 8 wt% of Polyvinylidene fluoride (PVDF, Sigma-Aldrich). This was then dispersed in the N-methyl-2-pyrrolidone solvent (NMP, Sigma-

Aldrich) for different solids loading. The paste was mixed with a SpeedMixer (FlackTeck Inc) at 2000 RMP for 20 minutes at room temperature.

4.2. ELECTRODE FABRICATION

An extrusion-based additive manufacturing system was used to extrude the paste into a 3D structure. An aluminum foil piece was fixed on a substrate, prior to printing, which was then used as a current collector after assembly. The extrusion-based additive manufacturing system was a home-built system consisting of a motion subsystem, a hot plate, extrusion devices, and power supply for the EF. The paste was loaded into a 10 ml plastic syringe with a 150 μm nozzle (EFD Inc), and extruded with 80 psi extrusion pressure onto the substrate that moved along the XY-axes. First, a base layer was printed to cover the current collector as a conventional laminated structure. Next, a digital structure was printed on top of the base layer to increase the specific surface area. After printing, a voltage of 10 kV, which was the maximum voltage without a spark, was applied at a distance of 1.25 cm for 10 minutes. A hot plate (at 120 ^{o}C) was used to remove solutions quickly. The conventional structures were cast by using a doctor blade on an aluminum foil, followed by EF processing. EFs were applied at a distance of 1.25 cm from the top of the electrode with variable applied voltages and different duration times.

4.3. MATERIALS CHARACTERIZATION

The morphologies of an EF-treated sample were characterized with a Scanning Electron Microscopy (SEM, Hitachi S4700) by using secondary electrons at 15kV

accelerating voltage. The SEM images were cropped to remove label bars and were adjusted to the same brightness and contrast by using ImageJ software. A threshold value of the gray level, representing the boundary of pores, was found to be 70 by observing a dozen of pores. This value was used for areal porosity measurements. The X-ray diffraction (Philips X-Pert Diffractometer) test was used to detect the particle orientation caused by the applied EFs. The whole electrode samples and their broken powder samples were compared through XRD tests.

4.4. ASSEMBLY

A CR2032 coin cell (Wellcos Corp) was used to assemble a battery in an argon-filled glove box (Mbraun). LMO was used as a cathode, Li foil as an anode, and commercial PP/PE/PP membrane (Celgard) as a separator; the battery was filled with liquid electrolyte 1M $LiFP_6$ EC:DMC 1:1 (Sigma-Aldrich).

4.5. ELECTROCHEMICAL MEASUREMENTS

The electrochemical behavior of the assembled coin cells was measured from 3 V to 4.2 V by using a battery testing station (IVIUMnSTAT, Ivium Tech). The specific capacity and areal capacity were measured under a 0.1 C-rate, and then the cycling performances were conducted with 0.1C, 0.2C, 0.5C, 1C, and back to 0.1C for five cycles. Battery impedance was measured via an electrochemical impedance spectroscopy (EIS) at 3.5 V open circle voltage, and the cyclic voltammetry curves were measured at 0.025-0.25 $mV \cdot s^{-1}$.

REFERENCES

[1] Lu, L., Han, X., Li, J., Hua, J. & Ouyang, M., A review on the key issues for lithium-ion battery management in electric vehicles," *J. Power Sources*, 226, 272-288 (2013).

[2] Nitta, N., Wu, F., Lee, J.T. & Yushin, G., Li-ion battery materials: present and future, *MaterialsToday*, 18, 252-264 (2015).

[3] Arthur, T.S., *et al.*, Three-dimensional electrodes and battery architectures, *Mrs Bulletin*, 36, 523-531 (2011).

[4] Gallagher, K.G., *et al.*, Optimizing areal capacities through understanding the limitations of lithium-ion electrodes, *J. The Electrochemical Society*, 163, A138-A149 (2016).

[5] Li, J., Leu, M.C., Panat, R. & Park, J., A hybrid three-dimensionally structured electrode for lithium-ion batteries via 3D printing, *Materials & Design*, 119, 417-424 (2017).

[6] Long, J.W., Dunn, B., Rolison, D.R. & White, H.S., Three-dimensional battery architectures, *Chemical Reviews*, 104, 4463-4492 (2004).

[7] Ferrari, S., *et al.*, Latest advances in the manufacturing of 3D rechargeable lithium microbatteries, *J. Power Sources*, 286, 25-46 (2015).

[8] Gibson, I., Rosen, D.W. & Stucker, B., *Additive manufacturing technologies* 238 (Springer, 2010).

[9] Adams, J.J., *et al.*, Conformal printing of electrically small antennas on three-dimensional surfaces, *Advanced Materials*, 23, 1335-1340 (2011).

[10] Engstrom, D.S., Porter, B., Pacios, M. & Bhaskaran, H., Additive nanomanufacturing–A review, *J. Materials Research*, 29, 1792-1816 (2014).

[11] Fu, K., *et al.*, Graphene oxide-based electrode inks for 3D-Printed lithium-ion batteries, *Advanced Materials*, 28, 2587-2594 (2016).

[12] Sun, K., *et al.*, 3D printing of interdigitated Li-Ion microbattery architectures, *Advanced Materials*, 25, 4539-4543 (2013).

[13] Kim, S.H., *et al.*, Printable solid-state lithium-ion batteries: a new route toward shape-conformable power sources with aesthetic versatility for flexible electronics, *Nano Letters*, 15, 5168-5177 (2015).

[14] Feilden, E., *et al.*, Robocasting of structural ceramic parts with hydrogel inks, *J. the European Ceramic Society*, 36, 2525-2533 (2016).

[15] Li, W., Ghazanfari, A., Leu, M.C. & Landers, R.G., Extrusion-on-demand methods for high solids loading ceramic paste in freeform extrusion fabrication. *Virtual and Physical Prototyping*, 1-13 (2017).

[16] Ahn, B.Y., *et al.*, Omnidirectional printing of flexible, stretchable, and spanning silver microelectrodes, *Science*, 323, 1590-1593 (2009).

[17] Wang, L., *et al.*, Crystal orientation tuning of LiFePO4 nanoplates for high rate lithium battery cathode materials. *Nano letters*, 12, 5632-5636 (2012).

[18] Cheah, S.K., *et al.*, Self-supported three-dimensional nanoelectrodes for microbattery applications, *Nano Letters*, 9, 3230-3233 (2009).

[19] Shaijumon, M.M., *et al.*, Nanoarchitectured 3D cathodes for Li-Ion microbatteries, *Advanced Materials*, 22, 4978-4981 (2010).

[20] Long, J.W. & Rolison, D.R., Architectural design, interior decoration, and three-dimensional plumbing en route to multifunctional nanoarchitectures, *Accounts of Chemical Research*, 40, 854-862 (2007).

[21] Habazaki, H., Kiriu, M. & Konno, H., High rate capability of carbon nanofilaments with platelet structure as anode materials for lithium ion batteries, *Electrochemistry Communications*, 8, 1275-1279 (2006).

[22] Wei, Q., *et al.*, Porous one-dimensional nanomaterials: design, fabrication and applications in electrochemical energy storage. *Advanced Materials*, (2017).

[23] Wen, W., *et al.*, Pseudocapacitance-Enhanced Li-Ion microbatteries derived by a TiN@ TiO 2 nanowire anode. *Chem*, 2, 404-416 (2017).

[24] Chan, C.K., Zhang, X.F. & Cui, Y., High capacity Li ion battery anodes using Ge nanowires. *Nano letters*, 8, 307-309 (2008).

[25] Wu, M.S., Chiang, P.C.J., Lee, J.T. & Lin, J.C., Synthesis of manganese oxide electrodes with interconnected nanowire structure as an anode material for rechargeable lithium ion batteries, *The Journal of Physical Chemistry B*, 109, 23279-23284 (2005).

[26] Velev, O.D., Gangwal, S. & Petsev, D.N., Particle-localized AC and DC manipulation and electrokinetics, *Annual Reports Section" C"(Physical Chemistry)*, 105, 213-246 (2009).

[27] Bouffier, L., Ravaine, V., Sojic, N. & Kuhn, A., Electric fields for generating unconventional motion of small objects, *Current Opinion in Colloid & Interface Science*, 21, 57-64 (2016).

[28] Park, J.S. & Saintillan, D., Electric-field-induced ordering and pattern formation in colloidal suspensions, *Physical Review E*, 83, 041409 (2011).

[29] Belijar, G., *et al.*, Dynamics of particle chain formation in a liquid polymer under ac electric field: modeling and experiments, *J. Physics D: Applied Physics*, 50, 025303 (2016).

[30] Jensen, E.C., Quantitative analysis of histological staining and fluorescence using ImageJ. *The Anatomical Record*, 296, 378-381 (2013).

[31] Wang, J., *et al.*, A homogeneous intergrown material of $LiMn_2O_4$ and $LiNi_{0.5}Mn_{1.5}O_4$ as a cathode material for lithium-ion batteries. *J. Materials Chemistry A*, 3, 2353-2360 (2015).

[32] Ilango, P.R., *et al.*, Eco-friendly nitrogen-containing carbon encapsulated $LiMn_2O_4$ cathodes to enhance the electrochemical properties in rechargeable Li-ion batteries. *Scientific Reports*, 6, p.29826 (2016).

[33] Mohamedi, M., Explicit analysis of impedance spectra related to thin films of spinel LiMn2O4, *J. Power Sources*, 93, 93-103 (2001).

[34] Guo D., *et al.*, Electrochemical performance of solid sphere spinel LiMn2O4 with high tap density synthesized by porous spherical Mn3O4, *Electrochimica Acta*, 123, 254-259 (2014).

[35] Zhang, S.S., Xu, K. & Jow, T.R., EIS study on the formation of solid electrolyte interface in Li-ion battery, *Electrochimica Acta*, 51, 1636-1640 (2006).

[36] Zhuang, Q.C., *et al.*, An electrochemical impedance spectroscopic study of the electronic and ionic transport properties of spinel LiMn2O4, *The Journal of Physical Chemistry C*, 114, 8614-8621 (2010).

[37] Cho, S., Chen, C.F. & Mukherjee, P.P.,"Influence of microstructure on impedance response in intercalation electrodes," *J. The Electrochemical Society*, 162, A1202-A1214 (2015).

III. ENHANCED BATTERY PERFORMANCE THROUGH 3D STRUCTURED ELECTRODES: EXPERIMENTAL AND MODELING STUDY

ABSTRACT

Three-dimensional (3D) electrode structures have the potential to significantly improve lithium-ion battery performance, such as power and energy density, but due to the complexity of geometries caused by the scale expansion, a precise understanding of the relationship between battery physics and structures is required. In this work, a novel hybrid 3D structure is investigated to deeply understand the advantages of the 3D structure and to provide a guideline for design optimization. Experimental observation from an extrusion-based 3D structure is incorporated into a 3D electrochemical model based on porous theory with a 4^{th} order approximation for solid phase concentration. A systematic study focused on the impact of electrode tap density (thickness and volume fractions) on 3D battery performance is conducted. Experimental and simulation results show that the proposed 3D hybrid structure exhibits higher specific capacity and area capacity than conventional electrode structures. This is found to be due to the uniformly distributed concentration within the electrode, even at thicker electrodes. Parametric metrics are introduced to provide the physical insight of 3D hybrid structure and the limiting factor for battery responses, and eventually a guideline for design optimization for more general 3D geometries.

1. INTRODUCTION

Advanced Lithium-Ion Batteries (LIBs) are one of the key solutions to the challenges associated with pollution and transportation energy costs to replace conventional fuels with cost-competitiveness. The development of an advanced battery with a reduction in its cost requires optimal battery design, which allows for minimizing unnecessary components that increase both weight and cost. In order to optimize battery design, besides developing new materials, it is necessary to enhance battery performance via optimizing battery electrode structures to promote the transport of species and their reactions.[1-5] Although the gravimetric capacity is one of the most utilized metrics in LIB studies as it describes the capacity that a material can deliver, the actual amount of materials in an electrode determines the energy and power of the LIB. Therefore, a high tap density is another important requirement for various applications.

Adding more material is one simple method for achieving high tap density, which can be fulfilled by increasing the thickness or volume fraction of electrodes. Conventional laminated composite electrodes are fabricated via a tape casting process that involves mixing the constituent materials and casting them onto a current collector. Tap density increases with increasing electrode thickness, however, the electrode exhibits lower power performance after a certain thickness. This is due to the limitation of transport of ions resulting in bad utilization of materials.[1] A better way to increase tap density without sacrificing power is to fabricate electrodes that can allow a more facile transport of the species.[2-5] Three-dimensional (3D) batteries have been considered to be a new solution for this approach. Currently, 3D structure batteries confirmed that the

3D electrode structure can efficiently improve the utilization of material.[5-11] In our previous work, a novel hybrid 3D electrode structure was developed to enhanced areal energy and power densities by overcoming the tradeoff between specific capacity and areal capacity.[5]

Compared to experiments, optimal battery design via modeling is the most effective way in terms of processing time and cost. Modeling tools for these purposes, however, must include appropriate design elements and must be accurate in predicting. A LIB can be decomposed into scales of three different lengths: meso-, micro-, and nano-scale. The kinetics and transport phenomena at the micro-/nano-scales must be linked to the mesoscale perspective, including electrode geometry, porosity, and thermal behavior. In recent decades, researchers have developed computational models to simulate the 3D structure based on non-porous electrode theory as a thin film model.[12-16] Those models can accurately account for geometry in nano-/micro-scale (particle-level) modeling, but are computationally expensive to consider the mesoscale (cell-level) battery structure. To simulate batteries in mesoscale, the pseudo-2D (P2D) model [17] has been widely used in predicting battery performance. This model relies on the continuum-based porous electrode theory, in which active particles are modeled via a homogenized P2D approach. This model is also able to study different active material composition effects on power and energy performance [18] and mechanical stress in the particles when the cell is subjected to a mechanical load.[19] This method is, however, limited to the study of homogenized systems, and therefore it cannot account for the effects of the geometry of the electrode on battery cell performance. Another mathematical model in 1D called Single Particle model [20] is the reduced order model

based on the P2D with an analytical expression for solid phase concentration. Although those models are also not able to capture the non-uniform geometry on a large scale, they are able to predict the solid phase concentration accurately without non-uniform electrode geometry information. By combining the P2D model and SP model, the battery performance with a non-uniform geometry should be able to be accurately simulated.[21]

In this paper, a 3D model has been developed based on the porous electrode theory to solve transport and kinetics problems of arbitrary 3D electrode structures by using a fourth order analytical solution to solve the solid phase diffusion problem. This model has been validated with experimental observations, and a case study of the effect of thickness on battery performance provides a better understanding of the benefits of 3D structures compared to conventional laminated structures. Numerical simulation results include detailed electrochemical behaviors at the geometric effects on the battery cell performance, such as solid phase concentration distribution, voltage profiles, and specific capacity. Further, the limiting factors of electrode structure were introduced and guidelines for determining optimal parameters were investigated.

2. EXPERIMENT AND SIMULATION METHOD

2.1. MATERIALS PREPARATION, ELECTRODE FABRICATION AND TEST

In this work, a $LiMn_2O_4$ (LMO) paste was used to fabricate the electrodes. A 30% solids loading paste was prepared by mixing 85.5 wt% LMO powder (MTI, 13 μm) with 6.5 wt% carbon black (CB, Alfa Aesar) and 8 wt% Polyvinylidene fluoride (PvdF, Sigma-Aldrich) in N-Methyl-2-pyrrolidone solvent (NMP, Sigma-Aldrich).

An extrusion-based additive manufacturing system was used to extrude the paste into a 3D structure. An aluminum foil piece was fixed on a substrate heated to 120 ºC prior to printing, which was used as a current collector after assembly. The paste was loaded into a plastic syringe with a 200 μm nozzle, and extruded onto a substrate that moved along the XY-axes. The hybrid 3D structure consisted of two parts: a base part and a digital structure part (Figure 1a). First, a base layer was printed to cover the current collector as a conventional laminated structure and the thickness of this base layer was optimized to yield the highest specific capacity (without 3D structure). Next, a digital structure, with a different number of layers, was printed on the top of the base layer to increase the specific surface area.

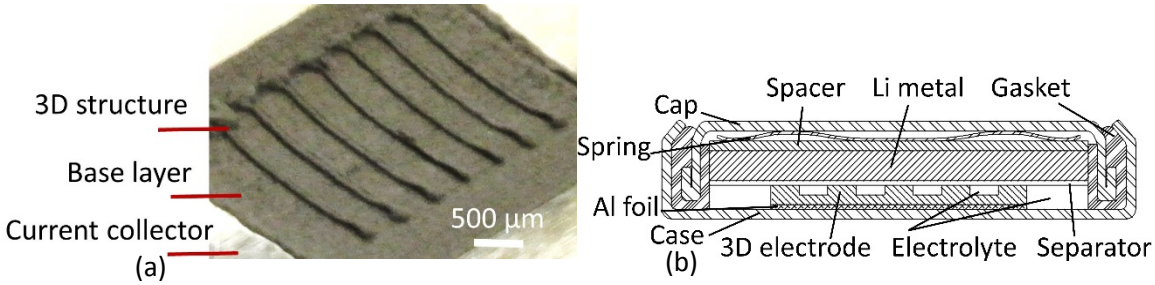

Figure 1. (a) Microscope image of printed hybrid 3D structure and (b) A CR2032 coin cell assembly with hybrid 3D structure cathode, lithium foil, separator, and electrolyte.

A CR2032 coin cell was used to assemble a battery (Figure 1b) in an argon-filled glove box. LMO was used as a cathode, Li foil as an anode, and commercial PP/PE/PP membrane as a separator; the battery was filled with liquid electrolyte 1M $LiFP_6$ EC:DMC 1:1 (Sigma-Aldrich). The electrochemical behavior of the assembled batteries was measured from 3 V to 4.2 V. The specific capacity and areal capacity were measured under a 0.1 C-rate.

2.2. CONTINUUM ELECTROCHEMICAL MODEL FOR LI-ION BATTERIES

A 3D half-cell model was used in this paper, the mass and charge conservation equations and the corresponding boundary conditions in the solids phase were applied to the electrode region as shown in Figure 2. Similarly, the governing equations related to the mass and charge conservation, and their boundary conditions in the electrolyte phase were applied to the electrode and separator regions. All those governing equations were derived from the porous electrode theory.

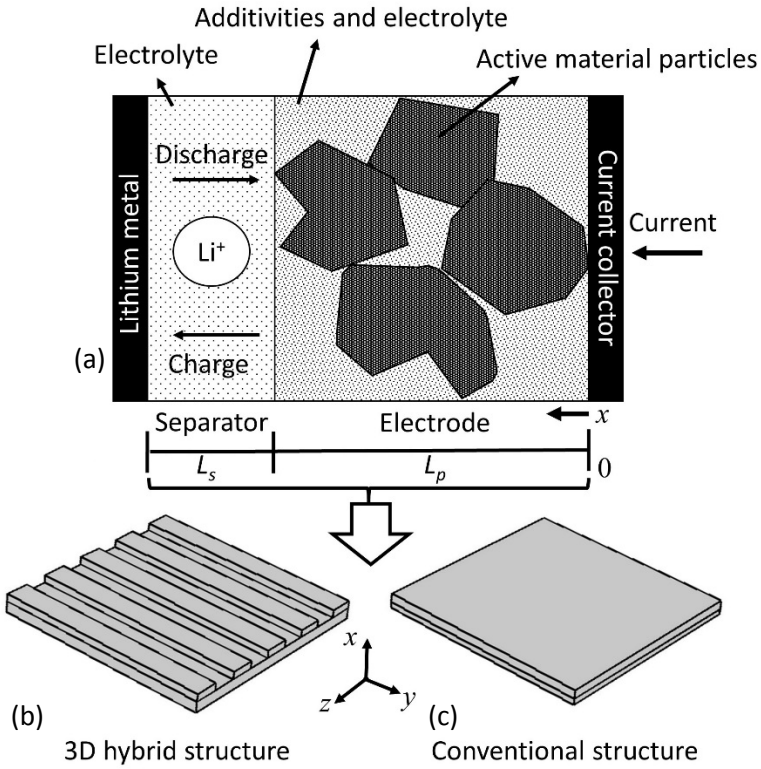

Figure 2. (a) Illustration of cell with porous electrode, (b) 3D hybrid structure and (c) conventional structure.

2.2.1. Transport In Solid Phase. Inside the active material of each electrode, the solid phase Li-ion concentration can be described by Fick's law in a spherical coordinate,

$$\frac{\partial c_{s,j}(r,t)}{\partial t} = \frac{D_{s,j}}{r^2}\frac{\partial}{\partial r}\left(r^2\frac{\partial c_{s,j}(r,t)}{\partial r}\right) \quad (1)$$

where $c_{s,j}$ is the solid phase Li-ion concentration, t is time, r is the radial coordinate, $D_{s,j}$ is the solid phase diffusion coefficient, and the subscript j = *p/n* denotes the positive/negative electrode. The boundary condition for Eq. 1 is:

$$D_{s,j}\frac{\partial c_{s,j}(t)}{\partial r}\bigg|_{r=0} = 0 \; and \; D_{s,j}\frac{\partial c_{s,j}(t)}{\partial r}\bigg|_{r=R_j} = -J_j(t) \quad (2)$$

where R_j is the particle radius and J_j is the Li-ion molar flux density on the active material surface.

In this work, a 4th order polynomial approximation is used to consider the solid phase concentration, which has been well established based on volume-averaging assumption. The solid phase concentration can be described as [20]

$$c_{s,j}(r,t) = a(t) + b(t)\left(\frac{r^2}{R_j^2}\right) + c(t)\left(\frac{r^4}{R_j^4}\right) \quad (3)$$

By substituting the polynomial approximation in Eq. 3 to Eq. 1, the coefficients *a(t)*, *b(t)*, and *c(t)*, respectively, are

$$a(t) = \frac{39}{4}c_{s,j,surf}(t) - 3R_j q_{s,j,avg}(t) - \frac{35}{4}c_{s,j,avg}(t) \quad (4a)$$

$$b(t) = -35c_{s,j,surf}(t) + 10R_j q_{s,s,avg}(t) + 35c_{s,j,avg}(t) \quad (4b)$$

$$c(t) = \frac{105}{4} c_{s,j,surf}(t) - 7R_j q_{s,s,avg}(t) - \frac{105}{4} c_{s,j,avg}(t) \quad (4c)$$

where $c_{s,j,surf}$ is the particle surface concentration, $c_{s,j,avg}$ is the average solid phase concentration, and $q_{s,j,surf}$ is the average solid phase flux.

Using the boundary conditions in Eq. 2 after substituting the polynomial approximation in Eq. 3 into Eq. 1, the following ODEs are obtained to describe the average solid-phase concentration and average solid-phase flux, respectively:

$$\frac{dc_{s,p,avg}(X,t)}{dt} = -\frac{J_p(X,t)}{3R_p} \quad (5)$$

$$\frac{dq_{s,p,avg}(X,t)}{dt} = -30\frac{D_{s,p}}{R_p^2} q_{s,p,avg}(X,t) - \frac{45}{2R_p^2} J_p(X,t) \quad (6)$$

where $\boldsymbol{X}$ is the coordinate (x, y, and z) inside 3D electrode as shown in Fig. 2.

Then, the particle surface concentration inside the cathode can be expressed as

$$c_{s,p,surf}(X,t) = c_{s,p,avg}(X,t) + \frac{8R_p}{35} q_{s,p,avg}(X,t) - \frac{R_p}{35D_{s,p}} J_p(X,t) \quad (7)$$

The Li-ion molar flux density is related to the individual electrodes overpotential through the Bulter-Vomer kinetics

$$J_p(X,t) = k_p c_{s,p,max} c_e^{0.5} \left(1 - \frac{c_{s,p,surf}(X,t)}{c_{s,p,max}}\right)^{0.5} \left(\frac{c_{s,p,surf}(X,t)}{c_{s,p,max}}\right)^{0.5} \times \left\{exp\left(\frac{0.5F}{RT}\eta_p(X,t)\right) - exp\left(-\frac{0.5F}{RT}\eta_p(X,t)\right)\right\} \quad (8a)$$

For the lithium electrode at $x = L_s+L_p$

$$J_{Li}(t) = 0.025\sqrt{c_{e,s}(X,t)}\left\{exp\left(-\frac{0.5F}{RT}\Phi_{e,s}(X,t)\right) - exp\left(\frac{0.5F}{RT}\Phi_{e,s}(X,t)\right)\right\} \quad (8b)$$

where k_p is the reaction rate constant, c_e is the electrolyte concentration, R is the universal gas constant, T is the ambient temperature, and η_j is the reaction overpotential defined as $\eta_p = \Phi_{s,p} - \Phi_{e,p} - U_p$, where $\Phi_{s,p}$ is the solid-phase potential, $\Phi_{e,p}$ is the electrolyte phase potential, and U_p is the open-circuit potential (OCP), which, in general, is a function of $c_{s,p,surf}$.

2.2.2. Transport In Electrolyte. The Li-ion concentration in the electrolyte phase changes due to the changes in the gradient diffusive flow of Li-ions. The equation is based on the porous electrode theory.[17]

$$\epsilon_k \frac{\partial c_{e,k}(X,t)}{\partial t} = \frac{\partial}{\partial X}\left(D_{eff,k}\frac{\partial c_{e,k}(X,t)}{\partial X}\right) + a_k(1-t_+)J_k(X,t) \quad (9)$$

where $k=p/s$ for cathode and separator, respectively, and $J_s(X,t) = 0$. ε_k is the liquid phase volume fraction, $D_{eff,k}$ is the effective diffusion coefficient, $D_{eff,k} = D_k(\varepsilon_k)^{brug}$, $brug$ is the Bruggman coefficient, a_k is the specific surface area of electrode, t_+ is the transference number in the electrolyte. The boundary condition are:

1. Fluxes of the ions are zero for all time at the current collector ($x = 0$ and $x = L_p + L_s$)

$$-D_{eff,p}\left.\frac{\partial c_{e,p}(t)}{\partial X}\right|_{x=0} = 0 \tag{10a}$$

$$-D_{eff,s}\left.\frac{\partial c_{e,s}(t)}{\partial X}\right|_{x=L_p+L_s} = \frac{J_{Li}(t)}{F} \tag{10b}$$

where L_p is cathode thickness and L_s is separator thickness.

The Li-ion concentration in the electrolyte phase changes due to the changes in the gradient diffusive flow of Li-ions. The equation is same as in the porous electrode theory

2. Continuity of the flux and concentration of the electrolyte at the electrode-separator interface

$$-D_{eff,p}\left.\frac{\partial c_{e,p}(t)}{\partial X}\right|_{x=L_p} = -D_{eff,s}\left.\frac{\partial c_{e,s}(t)}{\partial X}\right|_{x=L_p} \tag{11}$$

$$c_{e,p}(t)\big|_{x=L_p} = c_{e,s}(t)\big|_{x=L_p} \tag{12}$$

The initial condition for Eq. 9 is

$$c_{e,k}(X,0) = c_{e,k,0} \tag{13}$$

The specific electrode surface area, a_p, can be expressed in terms of the liquid phase volume fraction in cathode, ε_p, as

$$a_p = \frac{3\left(1-\epsilon_p\right)}{R_p} \tag{14}$$

2.2.3. Electrical Potentials. Charge conservation in the solid phase of each electrode can be described by Ohm's law

$$\sigma_{eff,j}\frac{\partial^2 \Phi_{s,j}(X,t)}{\partial X^2} = a_j F J_j(X,t) \tag{15}$$

The boundary conditions at the current collectors as a function of applied current density, I

$$-\sigma_{eff,p}\frac{\partial \Phi_{s,p}(t)}{\partial X}\bigg|_{x=0} = I \tag{16}$$

$$-\sigma_{eff,p}\frac{\partial \Phi_{s,p}(t)}{\partial X}\bigg|_{x=L_p} = 0 \tag{17}$$

where the current density I is related to the applied current, i_{app}, and the electrode foot area, *A*, as $I = i_{app}/A$, and $k_{eff,k}$ is the effective conductivity as a function of electrolyte concentration $k_{eff,k} = k_j(\varepsilon_j)^{0.5}$. Combining Kirchhoff's law with Ohm's law in the electrolyte phase yields

$$k_{eff,k}\frac{\partial^2\Phi_{e,k}(X,t)}{\partial X^2} - \frac{2k_{eff,k}RT(1-t_+)\partial^2 \ln c_{e,k}(X,t)}{F\partial X^2}\left(1+\frac{d\ln f_+}{d\ln c_{e,k}}\right) = I \qquad (18)$$

Since the boundary conditions of $\Phi_{e,k}$ is arbitrary. Set $\Phi_{e,k}(0, y, z, t) = 0$ at the positive electrode current collector interface. The remaining boundary conditions follow from continuity of $\Phi_{e,k}$

$$k_{eff,k}\frac{\partial\Phi_{e,k}(X,t)}{\partial X} - \frac{2k_{eff,k}RT(1-t_+)\partial \ln c_{e,k}(X,t)}{F\partial X}\left(1+\frac{d\ln f_+}{d\ln c_{e,k}}\right)\Bigg|_{x=0} = 0 \qquad (19a)$$

$$k_{eff,k}\frac{\partial\Phi_{e,k}(X,t)}{\partial X} - \frac{2k_{eff,k}RT(1-t_+)\partial \ln c_{e,k}(X,t)}{F\partial X}\left(1+\frac{d\ln f_+}{d\ln c_{e,k}}\right)\Bigg|_{x=L_p+L_s} = J_{Li}(t) \qquad (19b)$$

$$-k_{eff,p}\frac{\partial\Phi_{e,p}(t)}{\partial X}\Bigg|_{x=L_p} = -k_{eff,s}\frac{\partial\Phi_{e,s}(t)}{\partial X}\Bigg|_{x=L_p} \qquad (20)$$

The parameters used in the simulation are listed in Table 1, the battery geometry information, such as particle radius, electrode thickness, and volume fractions, are based on experiments and physical parameters, such as diffusivity and conductivity, are based on common material properties.

Table 1. Model parameters used in simulation studies.

Parameter	Value	Description
brug	1.5	Bruggeman coefficient
$C_{e,k,0}$	2000	Initial electrolyte concentration (mol m^{-3})
$C_{\max,\, pos}$	22860	Positive maximum concentration (mol m^{-3})
D_e	7.5×10^{-11}	Diffusion coefficient in electrolyte (m^2s^{-1})
$D_{s,p}$	2.5×10^{-15}	Solid-phase Li diffusivity, positive electrode (m^2s^{-1})
F	96487	Faraday's constant (C mol^{-1})
i_0	0.85	Constant flux for half-cell
I	Variable	Applied current density (A m^{-2})
$k_{s,p}$	3.8	Solid phase conductivity (S m^{-1})
k_p	2×10^{-6}	Reaction rate coefficient, cathode ($m^{2.5}mol^{-0.5}s^{-1}$)
L_p	Variable	Cathode thickness (m)
L_s	30×10^{-6}	Separator thickness (m)
R	8.314	Universal gas constant (J mol^{-1} K^{-1})
R_p	13×10^{-6}	Particle radius, positive electrode (m)
t_+	0.363	Cationic transport number
ε_p	0.24	Positive electrode porosity
ε_s	1	Separator porosity

3. RESULTS AND DISCUSSIONS

3.1. ELECTROCHEMICAL PERFORMANCE

The battery performance for the conventional structure (CS) and the 3D hybrid structure (HS) were compared at different electrode thickness. In the case of specific capacity (Figures 3a and 3b), the CS exhibited a maximum value (110 ± 5 mAh·g^{-1}) at 160 μm, and then decreased as the thickness increased further. However, the HS showed

a higher value (117 ± 6 mAh·g^{-1}) than that of the CS, even though it was much thicker (370 μm vs. 160 μm). As the case of CS, the specific capacity of the HS was decreased from its maximum value as the thickness of electrode increased. On the other hand, as the thickness increased (Figures 3a and 3c), the areal capacity of the CS continuously increased up to the maximum value (3.5 ± 0.08 mAh·cm^{-2} at 370 μm), which was much smaller than the maximum of HS, 4.5 ± 0.3 mAh·cm^{-2} at 270 μm as shown in Figure 3a and 3c. This was the result of a competition between the increased mass loading and the reduced specific capacity as the thickness increases.

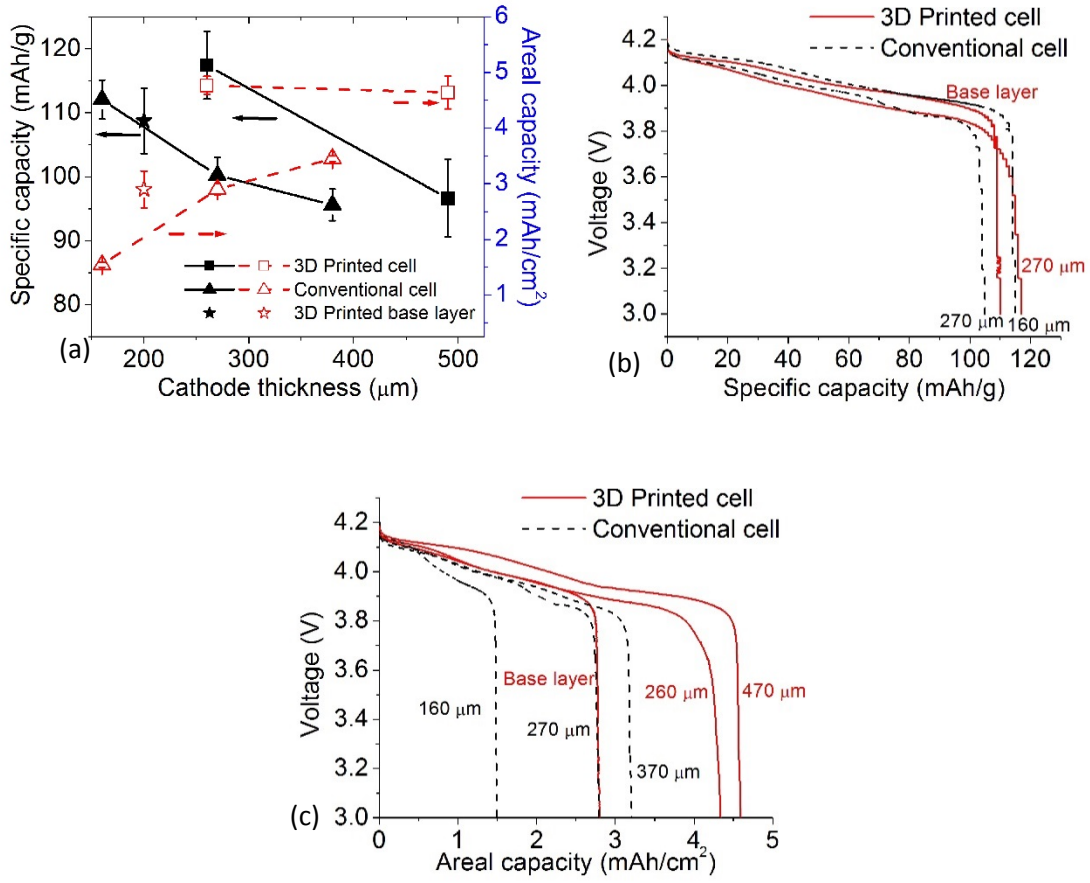

Figure 3. Comparison of conventional structure and printed 3D hybrid structure: (a) specific capacity and areal capacity as a function of cathode thickness, voltage profile at different electrode thickness as a function of specific capacity, and (c) voltage profile as a function of areal capacity.

3.2. VERIFICATION

The 3D model was first verified with P2D model [17] in term of the voltage profile and solid phase surface concentration at cathode-separator and cathode-current collector (C.C.) interface, respectively. As shown in Figures. 4a and 4b, the voltage profile of the 3D model were well matched with the ones from P2D model at the end of discharge with errors smaller than 0.3%, and the increase of voltage error at the end of discharge could due to the 3D model had a faster voltage drop after 3.7V compare to the P2D model. For the solid phase surface concentration as shown in Figures. 4c and 4d, the $c_{s,surf}$ of 3D model at two interfaces were agreed well with P2D model with maximum 300 mol/m^2 (2%) difference. This indicated that by combining the 4th order approximation equation for solid phase concentration with P2D model is enable to extend the model into three dimensional with ignorable errors.

3.3. IMPACT OF SOLID PHASE DIFFUSION AND ELECTROLYTE TRANSPORTATION

Solid phase diffusion in the active material particles and the electrolyte transportation are two important factors determining the reactions in the 3D electrode and battery performance. To evaluate the characteristic time of relative intercalation and electrolyte transport to the discharge time, two parameters S_c and S_S can be introduced for solid phase diffusion and electrolyte transport, respectively. [22] In this work, those two parameters were extended to study the effect of thickness and solid phase volume fraction in conventional and 3D electrodes as shown in Figures 5a and 5b.

For the conventional structure, the S_c is the ratio of diffusion time to discharge time

$$S_{c,con} = \frac{R_p^2 I}{D_{s,p} F (1 - \varepsilon_p) c_{max,pos} l_{pos}} \tag{17}$$

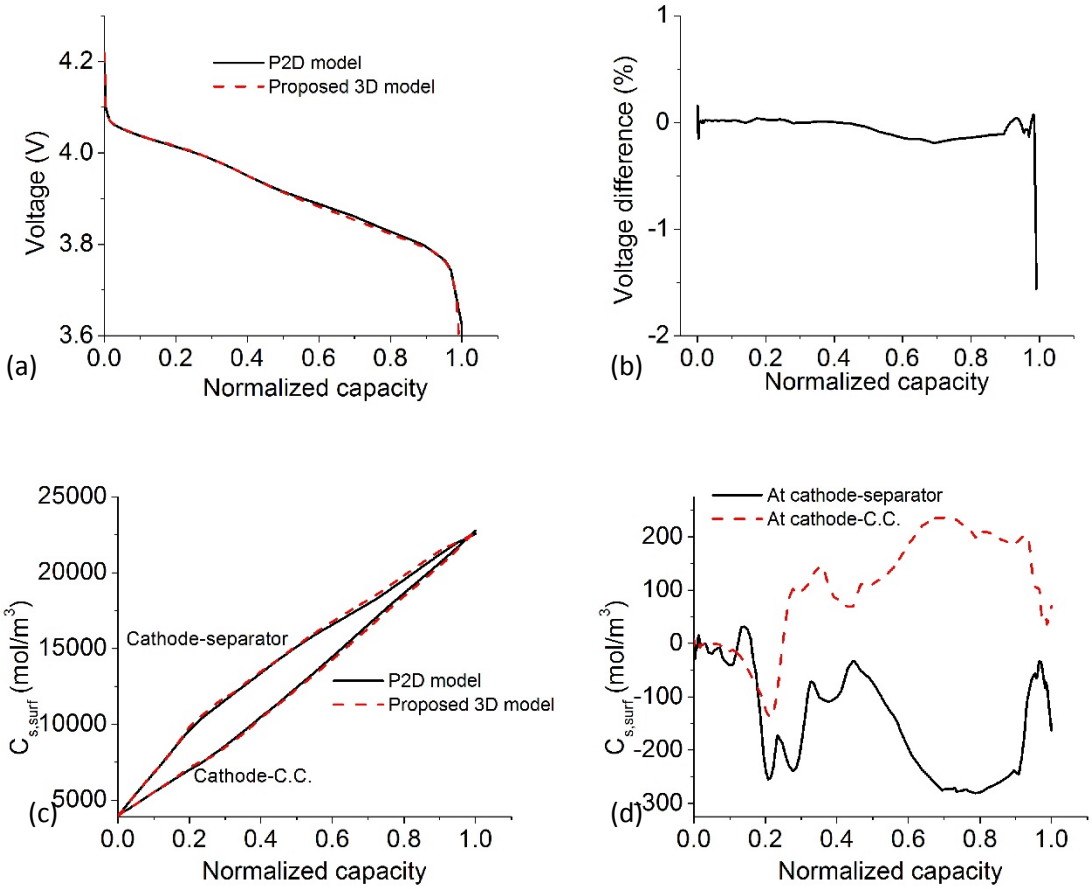

Figure 4. Comparison of P2D and 3Dof (a) voltage profile, (b) voltage difference between P2D and proposed 3D model and (b) solid phase surface concentration at cathode-separator and cathode-current collector interfaces.

The S_s is the ratio of electrolyte transport time to discharge time

$$S_{s,con} = \frac{(l_{sep} + l_{pos}) I w}{D_{eff,p} F (1 - \varepsilon_p) c_{max,pos} l_{pos}} \tag{18}$$

For 3D structure, an average length for cathode is used and Eqs. 17 and 18 can be rewired as:

$$S_{c,3D} = \frac{R_p^2 I(2n-1)}{D_{s,p} c_{max,pos}(1-\varepsilon_p) F\left(n l_{pos,1} + (n-1) l_{pos,2}\right)} \tag{19}$$

where n is the number of fingers in the 3D structure and $l_{pos,1}$ is the thickness of finger structure and $l_{pos,2}$ is the base structure, w is the length of electrode.

$$S_{s,3D} = \frac{\left(n\left(l_{pos,1} + l_{sep}\right) + (n-1)\left(l_{pos,2} + l_{sep}\right)\right) wI}{D_{eff,p} c_{max,pos}(1-\varepsilon_p) F\left(n l_{pos,1} + (n-1) l_{pos,2}\right)} \tag{20}$$

The current density can be calculated based on theoretical capacity with applied C-rate

$$I = \frac{i_{app}}{A} = \frac{Q_c(1-\varepsilon_p)\rho V C_{rate}}{A} = \frac{Q_c(1-\varepsilon_p)\rho A l_{pos} C_{rate}}{A} \tag{21}$$

where Q_c is the theoretical battery capacity, ρ is the active material density, V is the electrode volume.

According to Doyle et al [22], in case of S_c>>1, it means the diffusion in the solid phase is the limiting factor for battery performance, and in case of S_s >>1, the transportation concentration variation is the limiting factor. In this study, the S_c and S_s were compared with different volume fraction from 0.3 to 0.6 and different cathode

thickness from 160 to 500 μm. Both of S_c and S_s is the limiting factor (>>1) with variable thickness and volume fraction; the increase of S_c and S_s value means the solid phase diffusion or electrolyte transportation is a more critical factor. As shown in Figure 5c, the value of S_c was independent of the cathode thickness and volume fraction for both conventional and hybrid 3D structure. This is due the S_c is only limited by particle radius, R_p, and solid phase diffusion coefficient, $D_{s,p}$ (Eqs. 17 and 19) and independent from electrode geometry by considering the applied current (Eq. 21). The electrolyte transportation is limited by electrode geometry and depended on the volume fraction and electrode thickness (Eqs. 18 and 20). As shown in Figure 5d, the S_s value increased nonlinearly as a function of volume fraction and linearly as a function of electrode thickness. The S_s value was detailed in Figures 5e and 5f, for a variable thickness with 0.55 volume fraction and a variable volume fraction at 270μm thickness. Comparing the S_s of conventional and 3D hybrid structure, it can be seen that the 3D hybrid structure was able to improve the electrolyte transportation and more efficient at a thick thickness (maximum reduce 33%) and approximately reduce 12% at any volume fraction. This analysis explained how the 3D hybrid structure could improve the battery performance at a thicker thickness and can be further used to optimize the design of 3D structures.

3.4. 3D SIMULATION OF CONVENTIONAL AND HYBRID 3D STRUCTURE

The 3D computational model was validated with experimental results for the voltage profile of hybrid 3D structure and conventional structure at 270 μm thickness as shown in Figure 6a. Based on the geometry changes, the simulation was able to capture the transportation and diffusion in electrolyte and electrode region. The changes lead to a

different termination speed in the voltage profile, and the simulation results were able to capture the capacity change due to the modified geometry and generally agreed with experimental observation.

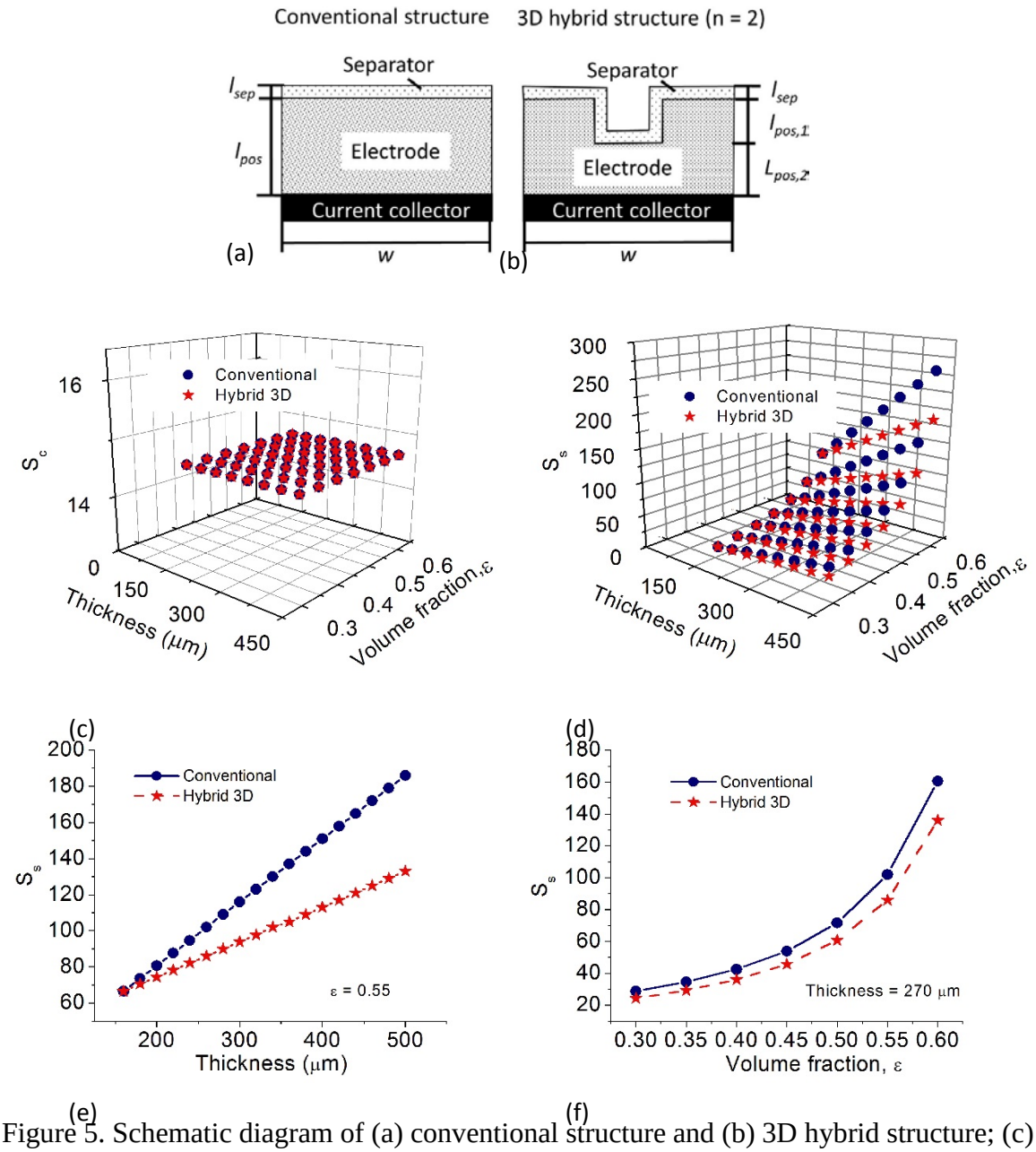

Figure 5. Schematic diagram of (a) conventional structure and (b) 3D hybrid structure; (c) S_c as a function of volume fraction and cathode thickness, (d) S_s as a function of volume fraction and cathode thickness, (e) S_s as a function of thickness with 0.55 volume fraction, and (f) S_s as a function of volume fraction at 270μm thickness.

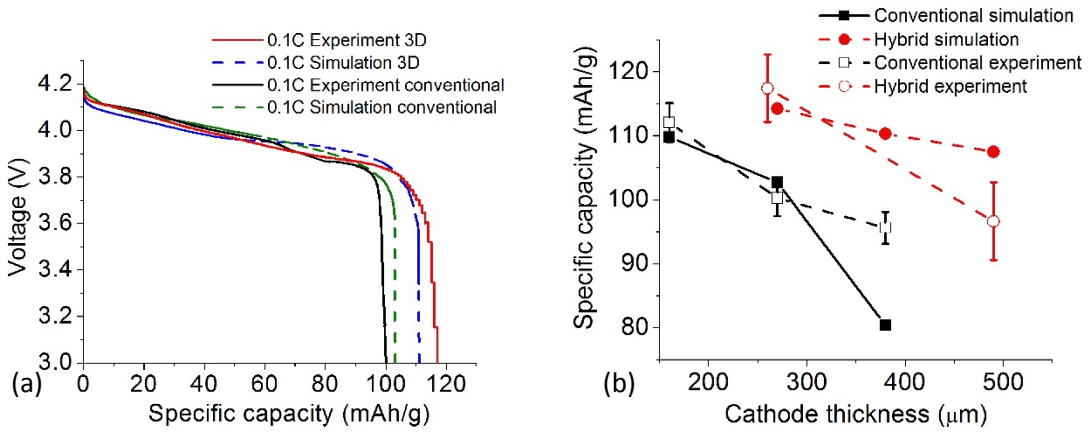

Figure 6. Comparison of (a) voltage profile with simulation and experimental results and (b) specific capacity as a function of electrode thickness.

The 3D model was used to compute the capacity change for 3D hybrid and conventional structure as a function of cathode thickness and compared with experimental results. As shown in Figure. 6b, the simulation was able to capture the capacity decrease with the increasing of electrode thickness from 160 to 490 μm. The simulation for conventional structure showed similar capacity change at 160 and 270 μm as experimental observation, and the capacity quickly decreased in the simulation could due to the limitation of electrolyte transportation as mentioned above. The experimental data showed less decreased capacity should thank the porous electrode where the electrolyte transportation might not be limited ideally as it in the simulation. For the hybrid 3D structure, the simulation agreed well with experimental results at 270 and 370 μm. The capacity decrease due to increased thickness showed less critical phenomena than experiments at 490 μm, which indicated that a better controlled 3D structure could further improve the battery performance.

The distribution of solid phase concentration and electrolyte concentration for 3D hybrid and conventional structures at different thickness were compared as shown in

Figure 7. The concentration gradient increased with increased thickness for both of 3D hybrid and conventional structure. For the conventional structure from 160 to 490 μm, the solid phase concentration difference between electrode-separator interface and electrode-C.C interface increased from 594 to 16900 mol/m^3; the electrolyte concentration difference between the electrode-C.C interface and separator-li foil interface increased from 240 to 3312 mol/m^3. Comparing the conventional structure, the 3D hybrid structure (Figures 7a to 7d) can reduce 96%, 95% and 46% of the solid phase concentration difference at 270 μm, 380 μm and 390 μm, respectively; it, as show in Figures 7e to 7g, also can reduce 8%, 19%, and 21% of the electrolyte concentration difference at 270 μm, 380 μm and 390 μm, respectively. It confirmed that the 3D structure could improve the transportation of ions inside electrolyte and then enhance the utilization of active materials. To obtain a clear idea about the advantages of 3D hybrid structure, a case of flux distribution is plotted at 270 μm as shown in Figure 7i, and the size of the arrow indicated the logarithm scale of flux inside the structure. It can be observed that the flux of 3D hybrid structure at the electrode-separator interface is stronger (5 times), then gradually decreasing toward electrode-c.c. interface and finally became similar to the flux of conventional structure.

Based on the concentration distribution, a stress distribution also can be compared. For the case of a spherical particle, the stress tensor contains two independent components: radial stress σ_r and tangential stress σ_t.

$$\sigma_r(r) = \frac{2\Omega_j E_j}{3(1-\nu_j)}\left(\frac{1}{R_j^3}\int_0^{R_j} c(r,t)\, r^2\, dr - \frac{1}{r^3}\int_0^{r} c(r,t)\, r^2\, dr\right) \tag{22}$$

$$\sigma_t(r) = \frac{\Omega_j E_j}{3(1-\nu_j)}\left(\frac{2}{R_j^3}\int_0^{R_j} c(r,t)\, r^2\, dr - \frac{1}{r^3}\int_0^{r} c(r,t)\, r^2\, dr - c(r,t)\right) \quad (23)$$

where $\tilde{c}$ is the concentration change from the initial value, ν_j is the Poisson's ratio, and E_j is the Young's modulus of active materials. [23]

The stress is considering the maximum stress at partcile surface ($r = R_p$), then the radial stress σ_r is zero, and then the Eq. 23 can be rewrite based the concentration analytical equations (Eqs. 5 and 7) as

$$\sigma_t(R_p) = \frac{\Omega_p E_p}{9(1-\nu_p)}\left(3c_{s,p,avg}(t) - 3c_{s,p,surf}(t)\right) \quad (24)$$

One case at 270 μm, as shown in Figure 7j, is used to compare the stress distribution. It can be observed that the maximum gradient of 3D hybrid structure (16 GPa) is slightly smaller than the one of the conventional structure (19 GPa). It is more important that the stress distribution is followed the pattern of the solid phase concentration, which leads to a uniformed distribution.

4. CONCLUSIONS

In this work, a 3D computational model based on the porous electrode theory with a 4th order analytical expression for solid phase concentration is developed to simulate the 3D battery electrode structure on a large scale. The results from the 3D model are compared with experimental observations based on voltage profile and capacity with

different electrode structure and thickness, it shows the capability of the 3D model to predict the voltage profile and capacity change with a 3D geometry.

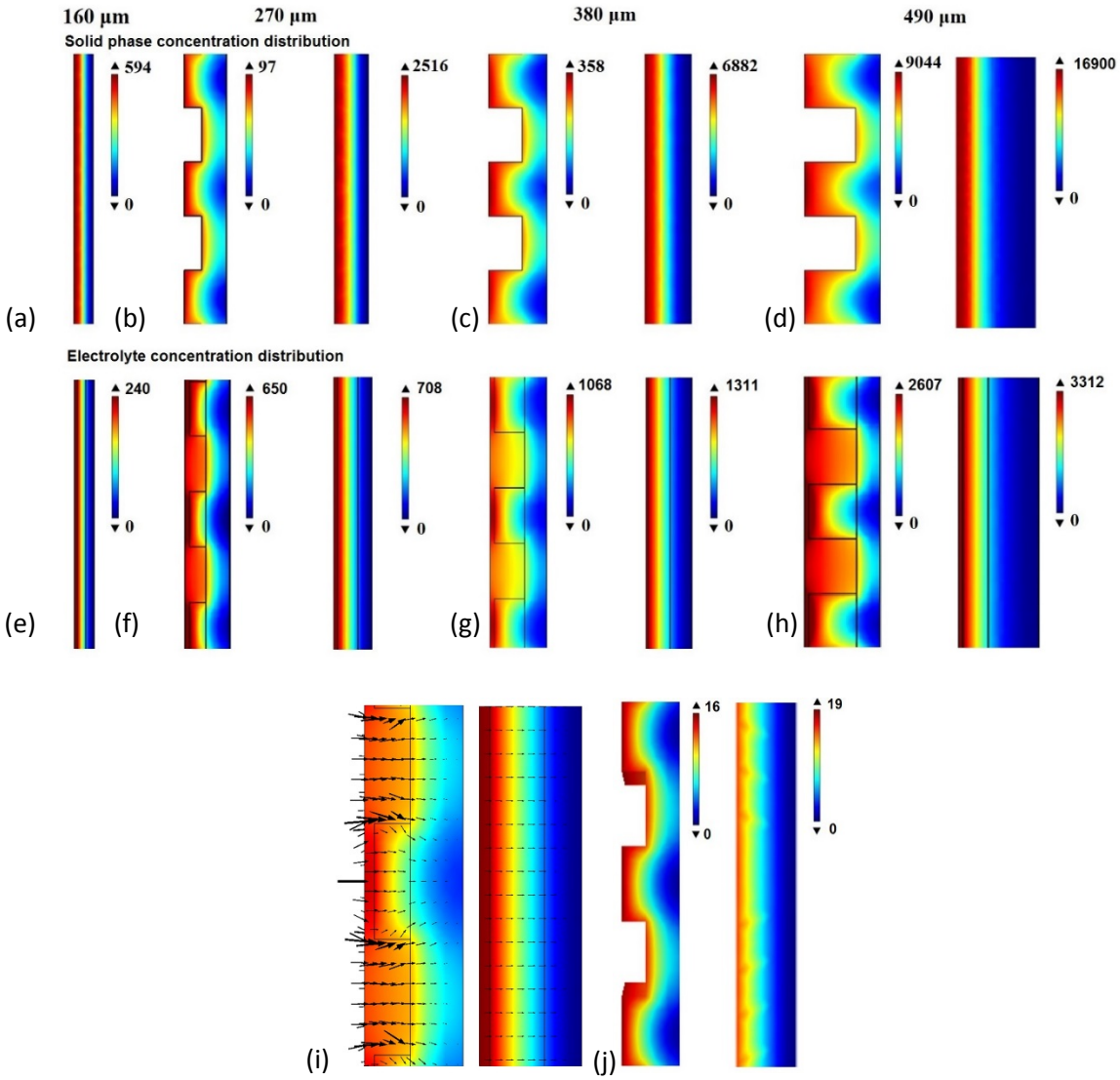

Figure 7. Comparison of concentration distribution (mol/m^3) as a function of thickness of solid phase concentration at (a) 160 µm, (b) 270 µm, (c) 380 µm, and (d) 490 µm; electrolyte concentration (mol/m^3)at (e) 160 µm, (f) 270 µm, (g) 380 µm, and (h) 490 µm; (i) Flux distribution and (j) tangential stress distribution (GPa) of the 270 µm thickness electrodes.

It is also found that the solid phase concentration gradient in the electrode structure plays an important role in the transport of the species, and the 3D structure would reduce the concentration gradient. An analytical method is also developed to determine the limiting factor in diffusion and electrolyte transportation. It found that the thickness and volume fraction are key factors in the battery structure design to determine battery performance. This model developed in this work can be defined as a guideline for future parameter determination and is able to be used to optimize the 3D electrode structure design.

REFERENCES

[1] Gallagher, K.G.; Trask, S.E.; Bauer, C.; Woehrle, T.; Lux, S.F.; Tschech, M.; Lamp, P.; Polzin, B.J.; Ha, S.; Long, B. and Wu, Q. Optimizing Areal Capacities Through Understanding the Limitations of Lithium-Ion Electrodes. *J. The Electrochem. Soc*, 2016, *163*(2), pp.A138-A149.

[2] Arthur, T.S.; Bates, D.J.; Cirigliano, N.; Johnson, D.C.; Malati, P.; Mosby, J.M.; Perre, E.; Rawls, M.T.; Prieto, A.L. and Dunn, B. Three-Dimensional Electrodes and Battery Architectures. *Mrs Bulletin*, 2011, *36*(7), pp.523-531.

[3] Ferrari, S.; Loveridge, M.; Beattie, S.D.; Jahn, M.; Dashwood, R.J. and Bhagat, R. Latest Advances in the Manufacturing of 3D Rechargeable Lithium Microbatteries. *J. Power Sources*, 2015, *286*, pp.25-46.

[4] Long, J.W.; Dunn, B.; Rolison, D.R. and White, H.S. Three-Dimensional Battery Architectures. *Chemical Reviews*, 2004, *104*(10), pp.4463-4492.

[5] Li, J.; Leu, M.C.; Panat, R. and Park, J. A Hybrid Three-Dimensionally Structured Electrode for Lithium-Ion Batteries via 3D Printing. *Materials & Design*, 2017, *119*, pp.417-424.

[6] Gibson, I.; Rosen, D.W. and Stucker, B. *Additive manufacturing technologies*, 2010, Vol. 238. New York: Springer.

[7] Adams, J.J.; Duoss, E.B.; Malkowski, T.F.; Motala, M.J.; Ahn, B.Y.; Nuzzo, R.G.; Bernhard, J.T. and Lewis, J.A. Conformal Printing of Electrically Small Antennas on Three-Dimensional Surfaces. *Advanced Materials*, 2011, *23*(11), pp.1335-1340.

[8] Engstrom, D.S.; Porter, B.; Pacios, M. and Bhaskaran, H. Additive Nanomanufacturing–A Review. *J. Materials Research*, 2014, *29*(17), pp.1792-1816.

[9] Fu, K.; Wang, Y.; Yan, C.; Yao, Y.; Chen, Y.; Dai, J.; Lacey, S.; Wang, Y.; Wan, J.; Li, T. and Wang, Z. Graphene Oxide-Based Electrode Inks for 3D-Printed Lithium-Ion Batteries. *Advanced Materials*, 2016, *28*(13), pp.2587-2594.

[10] Sun, K.; Wei, T.S.; Ahn, B.Y.; Seo, J.Y.; Dillon, S.J. and Lewis, J.A. 3D Printing of Interdigitated Li-Ion Microbattery Architectures. *Advanced Materials*, 2013, *25*(33), pp.4539-4543.

[11] Kim, S.H.; Choi, K.H.; Cho, S.J.; Choi, S.; Park, S. and Lee, S.Y. Printable Solid-State Lithium-Ion Batteries: A New Route Toward Shape-Conformable Power Sources with Aesthetic Versatility for Flexible Electronics. *Nano letters*, 2015, *15*(8), pp.5168-5177.

[12] Priimägi, P.; Brandell, D.; Srivastav, S.; Aabloo, A.; Kasemägi, H. and Zadin, V. Optimizing the Design of 3D-Pillar Microbatteries using Finite Element Modelling. *Electrochimica Acta*, 2016, *209*, pp.138-148.

[13] Martin, M.A.; Chen, C.F.; Mukherjee, P.P.; Pannala, S.; Dietiker, J.F.; Turner, J.A. and Ranjan, D. Morphological Influence in Lithium-Ion Battery 3D Electrode Architectures. *J. The Electrochem. Soc*, 2015, *162*(6), pp.A991-A1002.

[14] Das, S.; Li, J. and Hui, R.. Impact of Electrode Surface/Volume Ratio on Li-ion Battery Performance. In *Proceedings of the COMSOL Conference, Boston, MA, USA*, 2014, October. pp. 8-10.

[15] Lee, S.; Sastry, A.M. and Park, J. Study on Microstructures of Electrodes in Lithium-Ion Batteries using Variational Multi-scale Enrichment. *J. Power Sources*, 2016, *315*, pp.96-110.

[16] Park, J.; Li, J.; Lu, W. and Sastry, A.M. Geometric Consideration of Nanostructures for Energy Storage Systems. *J. Applied Physics*, 2016, *119*(2), p.025101.

[17] Doyle, M.; Newman, J.; Gozdz, A.S.; Schmutz, C.N. and Tarascon, J.M. Comparison of Modeling Predictions with Experimental Data from Plastic Lithium Ion Cells. *J. The Electrochem. Soc*, 1996, *143*(6), pp.1890-1903.

[18] Albertus, P.; Christensen, J. and Newman, J. Experiments on and Modeling of Positive Electrodes with Multiple Active Materials for Lithium-Ion Batteries. *J. The Electrochem. Soc*, 2009, *156*(7), pp.A606-A618.

[19] Golmon, S.; Maute, K. and Dunn, M.L. Numerical Modeling of Electrochemical–Mechanical Interactions in Lithium Polymer Batteries. *Computers & Structures*, 2009, *87*(23), pp.1567-1579.

[20] Subramanian, V.R.; Diwakar, V.D. and Tapriyal, D. Efficient Macro-Micro Scale Coupled Modeling of Batteries. *J. The Electrochem. Soc*, 2005, *152*(10), pp.A2002-A2008.

[21] Allu, S.; Kalnaus, S.; Simunovic, S.; Nanda, J.; Turner, J.A. and Pannala. A Three-Dimensional Meso-Macroscopic Model for Li-ion Intercalation Batteries. *J. Power Sources*, 2016, *325*, pp.42-50.

[22] Doyle, M.; Fuller, T.F. and Newman, J. Modeling of Galvanostatic Charge and Discharge of the Lithium/Polymer/Insertion Cell. *J. The Electrochem. Soc*, 1993, *140*(6), pp.1526-1533.

[23] Li, J.; Lotfi, N.; Landers, R.G. and Park, J., A Single Particle Model for Lithium-Ion Batteries with Electrolyte and Stress-Enhanced Diffusion Physics. *Journal of The Electrochemical Society*, 2017, *164*(4), pp.A874-A883.

IV. A SINGLE PARTICLE MODEL FOR LITHIUM-ION BATTERIES WITH ELECTROLYTE AND STRESS-ENHANCED DIFFUSION PHYSICS

ABSTRACT

A low-order battery model has been developed that incorporates stress-enhanced diffusion and electrolyte concentration distribution into a modified single particle model. This model addresses two important challenges of battery modeling for Battery Management Systems: accuracy and computational efficiency. The developed model improves accuracy by including the potential drop in the electrolyte based on the predicted li-ion concentration profile along the entire electrode thickness, and by including the enhanced diffusivity due to diffusion-induced stress. Incorporating analytical solutions into a conventional single particle model eliminates the need to sacrifice calculation efficiency. The voltage prediction by the proposed model is more accurate than the conventional single particle model. Compared to complex physics-based battery models, the proposed model significantly improves the computational efficiency of various discharge scenarios, including constant current, the Dynamic Stress Test, and the Highway Fuel Economy Test. Integrating mechanical responses into the single particle model not only increases model accuracy, but also makes it applicable to develop models for next-generation high energy density.

1. INTRODUCTION

Lithium Ion Batteries (LIBs) have the advantages of higher energy and power density, as compared to other rechargeable batteries, and are presently regarded as a core technology for energy storage and supply for Electric Vehicles (EV) and Hybrid Electric Vehicles (HEV) [1, 2]. However, as the usage of LIBs becomes more pervasive, increased concerns about their safety has become more critical. Consequently, a Battery Management System (BMS) is used to optimize storage capacity and balance the various systems to satisfy functional requirements and prevent catastrophic failures [3, 4]. In order to achieve these goals through a BMS, identification of the battery status is extremely important [5]. Therefore, advanced sensing and monitoring technologies are required to accurately predict the state of the battery and track the physical parameters. However, current sensing and monitoring technologies that rely heavily on voltage, current, and temperature are not sufficient to accurately predict the batteries' State of Charge (SOC) and State of Health (SOH). For this reason, a battery physical model is typically used in battery control and management systems, so that the internal battery status can be determined more accurately [6-9]. High-fidelity electrochemical models are ideal for detailed analysis of battery phenomena, but are too computationally intensive to use efficiently in BMS [3]. This has led to efforts to reduce the complexity of the electrochemical battery models. For example, the electrochemical model that was proposed by Doyle et al. [10] was reduced to a form suitable for a BMS [3, 11, 12]. However, for those simplified models, the process of identifying the model parameters, which is needed to construct these models, is difficult. One well-known simplified model

is the Equivalent Circuit Model (ECM), which describes battery dynamic behavior as a voltage source and a series of resistors and capacitors [13]. The common method for identifying ECM parameters is to use tests such as the Hybrid Power Pulse Characterization (HPPC) test [14]. However, these tests suffer from excessive measurement noise and lack of accurate initial estimates [15]. Most of all, the ECM model has limited prediction capability as it does not consider the electrochemical phenomena behind the battery performance [16]. The Single Particle (SP) model strikes the necessary balance between the electrochemical and equivalent circuit models. The SP model is described by a small series of ordinary differential equations, but it is derived directly from comprehensive electrochemical models, so it maintains many important battery characteristics explicitly. The SP model assumes that both electrodes are composed of spherical particles of the same shape and size, and the current distribution is uniform across both electrodes. Thus, each electrode can be approximated by a single spherical particle. The mass balance of li-ions in the intercalated particles of the electrode active material is described by Fick's law. One important drawback of the SP model is that it does not adequately describe the battery dynamics at high C-rates due to the absence of the electrolyte physics, even though it adequately describes the general charge-discharge behavior of the battery.[16-20].

In order to overcome this challenge, different approximations have been proposed for coupling the SP model with the electrolyte contribution by using different polynomial equations with various orders [21-25]. In general, the polynomial order determines the accuracy of the approximation. Higher-order polynomials will result in a higher accuracy; however, the numerical cost of the coefficient identification scheme will increase

accordingly. A quadratic equation describing the electrolyte concentration in the electrodes with a maximum error of approximately 4~8% was used in the refs. 22 and 25. Rahmian, et al. [23] reported a high charging rate with optimized pore wall flux using a third order polynomial for the electrolyte concentration in the electrodes. This model showed a maximum error of approximately 4% for a 5C discharge using a volume averaged flux. In addition, Naoki, et al. [24] studied battery thermal behavior using an SP model with electrolyte concentrations described by a parabolic profile. These models have been shown to be improved by adding the electrolyte physic model, but they are still not accurate (2-4% maximum error) compared to full-order electrochemical models. Further, some equations in the model were cumbersome and complicated for the BMS application.

Battery materials are inherently mechanical systems, where large and repeated strains develop inside the materials, and the corresponding stresses lead to cracks and fractures [26-32]. The basic function of electrochemical materials is fulfilled by ions' intercalating into the materials, meaning the ions enter the materials due to an electrochemical potential gradient [32]. During this intercalation process, there is a typical volume change of 10% for commercially available graphite materials, and even up to 300% for silicon materials [27, 33]. This volume change causes considerable stress inside the materials, leading to mechanical failures, such as material pulverization, and cracks and fractures in the materials. Further, the stress field inside a particle affects the diffusion process of li-ions. As a li-ion intercalates into the host material, a stress field builds due to displacement of the host atoms caused by the intercalated ion. This stress field affects the energy of the second intercalated ion, leading to an elastic interaction

between the two ions. This means that the diffusion process of ions in a particle under stress field is different from the stress-free diffusion behavior. Accordingly, these mechanical responses must be integrated into the SP model to determine the precise diffusivity of ions and their internal battery physics. It is also essential to predict the mechanical failure of battery electrodes.

In this study, we propose a new SP model that include electrolyte physics and a stress-diffusion coupling effect that improves the accuracy and computational efficiency of conventional SP models. To this end, a second-order analytical expression for electrolyte concentration distribution was developed based on electrochemical physics inside the entire battery cell, and the stress-enhanced diffusion was coupled to these physics. Simulation results of the proposed SP model were validated by comparing them with the results from a full-order electrochemical model and a conventional SP model. Further, galvanostatic constant discharge tests, the Dynamic Stress Test (DST), and the Highway Fuel Economy Test (HWFET) were conducted to demonstrate the accuracy of the new SP model for various operation scenarios.

2. PROPOSED SINGLE PARTICLE MODEL WITH ELECTROLYTE AND STRESS-ENHANCED DIFFUSION PHYSICS

Figure 1 is a schematic of a li-ion cell composed of two electrodes (solid matrix inside an electrolyte solution) and a separator (electrolyte solution). In the full order Pseudo-2D (P2D) electrochemical model, li-ion transport in the electrolyte phase is considered only in the *x* direction. The diffusional process in the solid phase is solved

based on a symmetric spherical particle assumption that the electrochemical reaction takes place on the surface of the particle.

The P2D electrochemical battery model consists of ten coupled nonlinear partial differential equations for the mass and charge balance in the solid and electrolyte phases [12]. The SP model is a simplified form of the P2D mode; however it does not include the electrolyte physics and mechanical responses. The following section presents the governing equations and assumptions for the proposed SP model.

2.1. SINGLE PARTICLE MODEL

In the conventional SP model, it is assumed that all particles in the electrode behave in a similar manner. Therefore, each electrode can be modeled as a single spherical particle, as shown in Fig. 1.

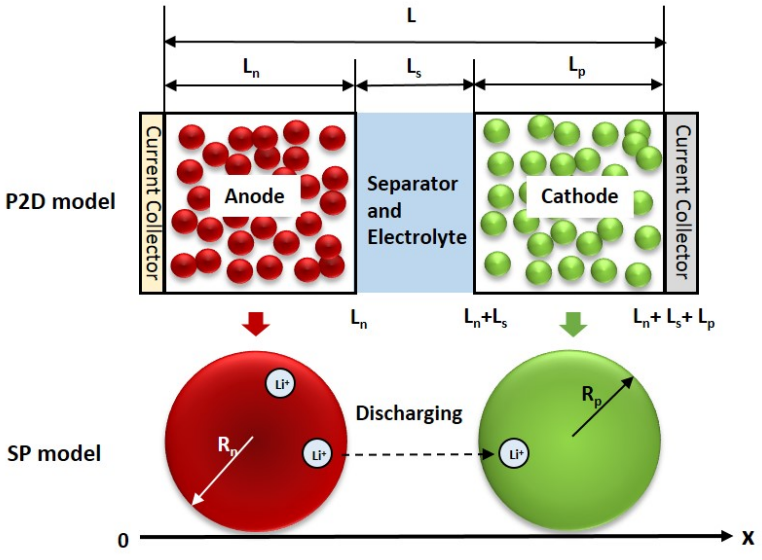

Figure 1. Schematic representation of three regions in li-ion cell.

Further, current passing through an electrode is assumed to be distributed uniformly over all of the particles [18, 34]. Each li-ion travels inside spherical solid particles by a diffusion process given by Fick's second law

$$\frac{\partial c_{s,j}(r,t)}{\partial t} = \frac{D_{s,j}}{r^2}\frac{\partial}{\partial r}\left[r^2\frac{\partial c_{s,j}(r,t)}{\partial r}\right] \tag{1}$$

where $c_{s,j}$ is the solid-phase li-ion concentration, t is time, r is the radial coordinate, $D_{s,j}$ is the solid-phase diffusion coefficient, and the subscript $j = p/n$ denotes the positive/negative electrode.

The boundary conditions for Eq. 1 are

$$D_{s,j}\frac{\partial c_{s,j}(r,t)}{\partial r}\Big|_{r=0} = 0,\ D_{s,j}\frac{\partial c_{s,j}(r,t)}{\partial r}\Big|_{r=R_j} = -J^{Li} \tag{2}$$

where R_j is the electrode particle radius.

The electrochemical reaction rate for the li-ion intercalation/(de)intercalation at the solid/solution interface, J^{Li}, can be expressed via the Butler-Volmer kinetics as [34]

$$J^{Li} = k_j c_{s,j,max} c_e^{0.5}\left[1-\frac{c_{s,j,surf}(t)}{c_{s,j,max}}\right]^{0.5}\left(\frac{c_{s,j,surf}(t)}{c_{s,j,max}}\right)^{0.5}\left\{\exp\left[\frac{0.5F}{RT}\eta_j(t)\right] - \exp\left[\frac{-0.5F}{RT}\eta_j(t)\right]\right\} \tag{3}$$

where k_j is the reaction rate constant, c_e is the electrolyte concentration, R is the universal gas constant, T is the temperature, F is Faraday's constant, and $c_{s,j,surf}(t)$ is expressed as a function of particle surface concentration $c_{s,j,surf}(t) = c_{s,j}(R_j,t)$.

The parameter η_j is the surface over-potential, defined as $\eta_j = \Phi_{1,j} - \Phi_{2,j} - U_j$, where

$\Phi_{1,j}$ is the solid-phase potential, $\Phi_{2,j}$ is solution-phase potential, and U_j is the Open Circuit Potential (OCP). The OCP, in general, is a function of the normalized surface concentration, $c_{s,j,surf}(t)/c_{s,j,max}(t)$, and temperature. Then, the potential difference can be obtained from Eq. 3

$$\eta_j(t) = \frac{2RT}{F} \ln\left[m_j(t) + \sqrt{m_j^2(t) + 1}\right] \tag{4}$$

where $m_j(t) = \frac{J^{Li}}{2k_j c_{s,j,max} c_e^{0.5} \left[1 - \frac{c_{s,j,surf}(t)}{c_{s,j,max}}\right]^{0.5} \left(\frac{c_{s,j,surf}(t)}{c_{s,j,max}}\right)^{0.5}}$.

Finally, the li-ion battery terminal voltage can be calculated based on the solid phase potential difference between both ends of the cell [34]

$$\begin{aligned} V_t(t) &= \Phi_{1,p}(t)\big|_{x=L} - \Phi_{1,n}(t)\big|_{x=0} \\ &= \left(\eta_p + \Phi_{2,p}(t)\big|_{x=L} + U_p\right) - \left(\eta_n + \Phi_{2,n}(t)\big|_{x=0} + U_n\right) \\ &= U_p\left[\frac{c_{s,p,surf}(t)}{c_{s,p,max}}\right] - U_n\left[\frac{c_{s,n,surf}(t)}{c_{s,n,max}}\right] \\ &+ \frac{2RT}{F}\left\{\ln\left[m_p(t) + \sqrt{m_p^2(t) + 1}\right]\right. \\ &\left. - \ln\left[m_n(t) + \sqrt{m_n^2(t) + 1}\right]\right\} + \Phi_{2,p}(t)\big|_{x=L} - \Phi_{2,n}(t)\big|_{x=0} \end{aligned} \tag{5}$$

where $\Phi_{2,p}(t)\big|_{x=L} - \Phi_{2,n}(t)\big|_{x=0}$ denotes the electrolyte potential difference.

In the SP model, the potential gradient inside the electrolyte is neglected. In such models, introducing a resistance term into the Butler-Volmer kinetics only aims at modeling the interface resistance and does not account for the potential distribution

within the electrolyte. The internal resistance is approximated as an ohmic voltage drop, $i_{app}R_{cell}$, where i_{app} is the applied current density. The resistance value R_{cell} depends on many complex mass and charge transfer phenomena. Guo et al. [34] approximated this resistance as an empirical function of the ambient temperature and the battery terminal current. In [35], the resistance R_{cell} is assumed as a function of electrode ionic conductivities and electrode thicknesses. This assumption is a critical drawback of the conventional SP model and, as a result, the model cannot adequately describe battery dynamics at high C-rates [16-20].

2.2. ELECTROLYTE CONCENTRATION DISTRIBUTION AND ELECTROLYTE POTENTIAL DIFFERENCE

In the proposed SP model, the li-ion concentration distribution is obtained by applying mass conservation in the electrolyte. Here, the electrolyte concentration distribution, $c_{e,i}(x,t)$, includes the lithium ionic concentration in both electrodes and the separator as a function of time, t, and position, x, where the subscript $i = p/s/n$ represents the positive electrode/separator/negative electrode. The transfer of li-ions in the electrolyte can be described by porous electrode theory. In the separator region, Fick's first law is used because there is no electrochemical reaction in that region. Consequently, the governing equations for the electrolyte concentration in the positive electrode, separator, and negative electrode, respectively, are [22,25]

$$\varepsilon_{e,n}\frac{\partial c_{e,n}}{\partial t} = D_{e,n}^{eff}\frac{\partial^2 c_{e,n}}{\partial x^2} + (1-t_+)\frac{i_{app}}{FL_n} \quad (0 \le x \le L_n) \tag{6}$$

$$\varepsilon_{e,s}\frac{\partial c_{e,s}}{\partial t} = D_{e,s}^{eff}\frac{\partial^2 c_{e,s}}{\partial x^2} \quad (L_n \le x \le L_n + L_s) \tag{7}$$

$$\varepsilon_{e,p}\frac{\partial c_{e,p}}{\partial t} = D_{e,p}^{eff}\frac{\partial^2 c_{e,p}}{\partial x^2} + (1 - t_+)\frac{i_{app}}{FL_p} \quad \left(L_n + L_s \le x \le L_n + L_s + L_p\right) \tag{8}$$

where $D_{e,i}^{eff} = D_e\varepsilon_{e,i}^{brug}$ is the effective diffusivity, $L_n/L_s/L_p$ and $\varepsilon_{e,n}/\varepsilon_{e,s}/\varepsilon_{e,p}$ are the thicknesses and the porosities for the anode, separator, and cathode, respectively, and *brug* denotes the bruggeman coefficient, which is 1.5.

The diffusion coefficient, D_e, and the cationic transport number in the electrolyte, t_+, are considered to be constant and independent of the electrolyte concentration. Considering the continuity of the concentration and mass flux, their boundary conditions can be expressed as:

1. No mass flux at the two ends of the cell in the *x*-direction

$$\left.\frac{\partial c_{e,n}}{\partial x}\right|_{x=0} = 0, \quad \left.\frac{\partial c_{e,p}}{\partial x}\right|_{x=L} = 0 \tag{9}$$

2. Continuity of the concentration and flux at the anode-separator interface

$$c_{e,n}(L_n, t) = c_{e,s}(L_n, t)\,, \quad D_{e,n}^{eff}\left.\frac{\partial c_{e,n}}{\partial x}\right|_{x=L_n} = D_{e,s}^{eff}\left.\frac{\partial c_{e,s}}{\partial x}\right|_{x=L_n} \tag{10}$$

3. Continuity of the concentration and flux at the separator-cathode interface

$$c_{e,s}(L_n + L_s, t) = c_{e,p}(L_n + L_s, t),$$
$$D_{e,s}^{eff} \frac{\partial c_{e,s}}{\partial x}\Big|_{x=L_n+L_s} = D_{e,p}^{eff} \frac{\partial c_{e,p}}{\partial x}\Big|_{x=L_n+L_s} \quad (11)$$

4. Electrolyte concentration balance inside the entire region

$$\int_0^{\mathrm{Ln}} c_{e,n}(x,t)\varepsilon_{e,n}\,dx + \int_{\mathrm{Ln}}^{\mathrm{Ln+Ls}} c_{e,s}(x,t)\varepsilon_{e,s}\,dx + \int_{\mathrm{Ln+Ls}}^{\mathrm{Ln+Ls+Lp}} c_{e,p}(x,t)\varepsilon_{e,p}\,dx = c_0(\mathrm{Ln} + \mathrm{Ls} + \mathrm{Lp}) \quad (12)$$

The continuous electrolyte concentration profiles (Eqs. 6-8) can be approximated, in general, by polynomial functions

$$c_{e,i}(x,t) = \alpha_k(t)x^m + \alpha_k(t)x^{m-1} \cdots + \alpha_k(t) + \beta \quad i = p,s,n \quad k = 1,2,3 \cdots \quad (13)$$

The polynomial orders for the electrolyte concentrations in the electrodes and separator can be different. It has been observed at steady state that the electrolyte concentration distribution can be approximated by a parabolic profile in the electrodes and a linear profile in the separator [22]. At the beginning of discharge, the li-ions deintercalate from the active particles to the electrolyte in the negative electrode, and intercalate from the electrolyte to the cathode particles in the positive electrode. Thus, the electrolyte concentration in the negative electrode increases, while it decreases in the positive electrode. As $t = \infty$, the cell stays a steady status and the competitive effects of the li-ions moving into/out of the electrolyte from the solid electrodes (i.e.

electrochemical reaction) and the concentration gradient (i.e. diffusion) are balanced [22, 23]. In this work, second-order polynomials are chosen for the electrolyte concentrations inside the negative electrode, the separator, and the positive electrode, respectively. For this, the general equation in Eq. (13) is further simplified with α_k as a form of $a_k(1 - e^{-b_k t})$ and β to be the initial concentration c_0

$$c_{e,n}(x,t) = a_1(1 - e^{-b_1 t})x^2 + a_2(1 - e^{-b_1 t}) + c_0 \tag{14}$$

$$c_{e,s}(x,t) = a_3(1 - e^{-b_3 t})x^2 + a_4(1 - e^{-b_3 t}) + c_0 \tag{15}$$

$$c_{e,p}(x,t) = a_5(1 - e^{-b_2 t})(L - x)^2 + a_6(1 - e^{-b_2 t}) + c_0 \tag{16}$$

The initial electrolyte concentration is

$$c_{e,i}(x,0) = c_0 \tag{17}$$

Under steady-state conditions, the electrolyte concentrations at different locations are independent of time; therefore, equations (14-16), respectively, become

$$c_{e,n}(x,t) = a_1x^2 + a_2 + c_0 \tag{18}$$

$$c_{e,s}(x,t) = a_3x^2 + a_4 + c_0 \tag{19}$$

$$c_{e,p}(x,t) = a_5(L-x)^2 + a_6 + c_0 \tag{20}$$

In addition, based on Eqs. 6-8, the total amount of Li^+ in the three regions can be expressed by the following equations [25]:

$$\frac{d}{dt}\left(\varepsilon_{e,n}\int_0^{L_n} c_{e,n}(x,t)\,dx\right) = D_{e,n}^{eff}\frac{dc_{e,n}(L_n,t)}{dx} + (1-t_+)\frac{i_{app}}{F} \tag{21}$$

$$\frac{d}{dt}\left(\varepsilon_{e,s}\int_{L_n}^{L_n+L_s} c_{e,s}(x,t)\,dx\right) = D_{e,s}^{eff}\left(\frac{dc_{e,s}(L_n+L_s,t)}{dx} - \frac{dc_{e,s}(L_n,t)}{dx}\right) \tag{22}$$

$$\frac{d}{dt}\left(\varepsilon_{e,p}\int_{L_n+L_s}^{L_n+L_s+L_p} c_{e,p}(x,t)\,dx\right) = -D_{e,p}^{eff}\frac{dc_{e,p}(L_n+L_s,t)}{dx} - (1-t_+)\frac{i_{app}}{F} \tag{23}$$

The coefficients a_k can be obtained from the boundary conditions in Eqs. 10-12 and from mass conservation (Eqs. 21-23)

$$a_1 = -\frac{\varepsilon_{e,n}^{-brug} J}{2\,D_e\,L_n} \tag{24}$$

$$a_2 = \frac{\left\{J\left[\varepsilon_{e,n}^{1-brug}L_n^2 + 2\varepsilon_{e,p}^{1-brug}L_p^2 + 6\varepsilon_{e,p}\varepsilon_{e,s}^{-brug}L_sL_p + 3\varepsilon_{e,s}^{1-brug}L_s^2 + 3\varepsilon_{e,n}^{1-brug}L_n(\varepsilon_{e,p}L_p + \varepsilon_{e,s}L_s)\right]\right\}}{6D_e(\varepsilon_{e,n}L_n + \varepsilon_{e,p}L_p + \varepsilon_{e,s}L_s)} \tag{25}$$

$$a_5 = \frac{\varepsilon_{e,p}^{-brug} J}{2 D_e L_p} \tag{26}$$

$$a_{6=} - \frac{J(2\varepsilon_{e,n}^{1-brug} L_n^2 + 3\varepsilon_{e,n}\varepsilon_{e,p}^{-brug} L_n L_p + \varepsilon_{e,p}^{1-brug} L_p^2 + 6\varepsilon_{e,n}\varepsilon_{e,s}^{-brug} L_n L_s + 3\varepsilon_{e,p}^{-brug} \varepsilon_{e,s} L_s L_p + 3\varepsilon_{e,s}^{1-brug} L_s^2)}{6 D_e(\varepsilon_{e,n} L_n + \varepsilon_{e,p} L_p + \varepsilon_{e,s} L_s)} \tag{27}$$

where $J = (1 - t_+)\frac{i_{app}}{F}$.

In the unsteady state, a linear concentration in the separator is assumed to simplify Eq. (15) using two values at the boundaries of the anode-separator and separator-cathode. As a result, the expression for electrolyte concentration distribution in the separator (Eq. 15) can be rewritten as

$$c_{e,s}(x,t) = \frac{(x - L_n - L_s)\{a_5(1 - e^{-b_2 t}) L_p{}^2 + a_6(1 - e^{-b_2 t}) - [a_1(1 - e^{-b_1 t}) L_n{}^2 + a_2(1 - e^{-b_1 t})]\}}{L_s} + a_5(1 - e^{-b_2 t}) L_p{}^2 + a_6(1 - e^{-b_2 t}) + c_0 \tag{28}$$

Then, based on flux continuity and approximated solution (Eqs. 10, 11, 14, 16 and 28), the coefficients b_1 and b_2 are

$$b_1 = \frac{6 \mathrm{D}_e \varepsilon_{e,n}^{\mathrm{brug}-1} \varepsilon_{e,p}^{\mathrm{brug}} \varepsilon_{e,s}^{\mathrm{brug}} (\varepsilon_{e,n} L_n + \varepsilon_{e,p} L_p + \varepsilon_{e,s} L_s)}{L_n \left[2\varepsilon_{e,n}^{\mathrm{brug}} \varepsilon_{e,p}^{\mathrm{brug}} \varepsilon_{e,s}^{\mathrm{brug}} \mathrm{L}_p^2 + 2\varepsilon_{e,p}^{1+\mathrm{brug}} L_p \left(\varepsilon_{e,s}^{\mathrm{brug}} L_n + 3\varepsilon_{e,n}^{\mathrm{brug}} L_s\right) + \varepsilon_{e,p}^{\mathrm{brug}} \varepsilon_{e,s} L_s \left(2\varepsilon_{e,s}^{\mathrm{brug}} L_n + 3\varepsilon_{e,n}^{\mathrm{brug}} L_s\right)\right]} \tag{29}$$

$$b_2 = \frac{6 \mathrm{D}_e \varepsilon_{e,n}^{\mathrm{brug}} \varepsilon_{e,p}^{\mathrm{brug}-1} \varepsilon_{e,s}^{\mathrm{brug}} (\varepsilon_{e,n} L_n + \varepsilon_{e,p} L_p + \varepsilon_{e,s} L_s)}{L_p \left[2\varepsilon_{e,n} \varepsilon_{e,p}^{\mathrm{brug}} \varepsilon_{e,s}^{\mathrm{brug}} \mathrm{L}_n^2 + 2\varepsilon_{e,n}^{1+\mathrm{brug}} L_n \left(\varepsilon_{e,s}^{\mathrm{brug}} L_p + 3\varepsilon_{e,p}^{\mathrm{brug}} L_s\right) + \varepsilon_{e,n}^{\mathrm{brug}} \left(2\varepsilon_{e,s}^{1+\mathrm{brug}} L_p L_s + 3\varepsilon_{e,p}^{\mathrm{brug}} \varepsilon_{e,s} \mathrm{L}_s^2\right)\right]} \tag{30}$$

Eqs. 14, 16, and 28 are the analytical solutions for the electrolyte concentration distribution in the cathode, electrolyte, and anode regions, respectively, as a function of the spatial coordinate *x* (Fig. 1).

Then the electrolyte potential and potential difference can be calculated as detailed in ref. 36. The analytical equations for electrolyte potential were derived based on the electrolyte charge conservation equation, and expressed as:

For the negative electrode region ($0 \leq x \leq L_n$)

$$\Phi_e(x) = \Phi_e(0) + (1 - t_+)\frac{2RT}{F}\ln\frac{c_e(x)}{c_e(0)} - \frac{i_{app}}{2L_n k_n^{eff}}x^2 \tag{31}$$

For the separator region ($L_n \leq x \leq L_n+Ls$)

$$\Phi_e(x) = \Phi_e(0) + (1 - t_+)\frac{2RT}{F}\ln\frac{c_e(x)}{c_e(0)} - \frac{i_{app}}{k_s^{eff}}(x - L_n) - \frac{i_{app}L_n}{2k_n^{eff}} \tag{32}$$

For the positive electrode region ($L_n+L_s \leq x \leq L_n+L_s+L_p$)

$$\Phi_e(x) = \Phi_e(0) + (1 - t_+)\frac{2RT}{F}\ln\frac{c_e(x)}{c_e(0)} + \frac{i_{app}}{2L_p k_p^{eff}}(L - x)^2 - \frac{i_{app}}{2}\left(\frac{L_n}{k_n^{eff}} + \frac{2L_s}{k_s^{eff}} + \frac{L_p}{k_p^{eff}}\right) \tag{33}$$

where $k_i^{eff} = k_i * \varepsilon_i^{\text{brug}}$, and k_n, k_s, and k_p are the electrolyte conductivities in the anode, separator, and cathode, respectively, which are functions of electrolyte concentration [36].

The electrolyte potential difference is obtained by the difference between the potentials taken from the electrode-current collector interface (i.e., $x = 0$ and $x = L$). In addition, the last part of Eq. 34 can be regarded as anohmic resistance, which is expressed as a function of electrode geometry and electrolyte effective conductivity. [36]

$$\Phi_{2,p}(t)\big|_{x=L} - \Phi_{2,n}(t)\big|_{x=0} = \Phi_e(L,t) - \Phi_e(0,t)$$
$$= (1 - t_+)\frac{2RT}{F}\ln\frac{c_{e,p}(L,t)}{c_{e,n}(0,t)} - \frac{i_{app}}{2}\left(\frac{L_n}{k_n^{eff}} + \frac{2L_s}{k_s^{eff}} + \frac{L_p}{k_p^{eff}}\right) \quad (34)$$

2.3. STRESS MODEL

In order to calculate the solid phase li-ion concentration due to a stress build-up, the insertion/extraction of ions are modeled as a diffusion-stress coupling process. By considering the chemical potential due to the concentration gradient and mechanical strain energy [28], the species flux, $J_{st,}$ can be expressed by

$$J_{st} = -D_{s,j}\left[\nabla c_{s,j}(r,t) - \frac{\Omega_j c_{s,j}(r,t)}{RT}\nabla\sigma_h\right] = \frac{i_{app}}{F} \quad (35)$$

$$\frac{\partial c_{s,j}(r,t)}{\partial t} + \nabla \cdot J_{st} = 0 \quad (36)$$

where Ω_j is the partial molar volume and σ_h is the hydrostatic stress.

Then, concentration can be rewritten bysubstituting Eq. 35 into Eq. 36

$$\frac{\partial c_{s,j}(r,t)}{\partial t} = D_{s,j}\left[\nabla^2 c_{s,j}(r,t) - \frac{\Omega_j}{RT}\nabla c_{s,j}(r,t)\cdot\nabla\sigma_h - \frac{\Omega_j c_{s,j}(r,t)}{RT}\nabla^2\sigma_h\right] \tag{37}$$

For the case of a spherical particle, the stress tensor contains two independent components [28]: radial stress σ_r and tangential stress σ_t.

$$\sigma_r = \frac{2\Omega_j E_j}{3(1-\nu_j)}\left(\frac{1}{R_j^3}\int_0^{R_j}\tilde{c}\,r^2\,dr - \frac{1}{r^3}\int_0^{r}\tilde{c}\,r^2\,dr\right) \tag{38}$$

$$\sigma_t = \frac{\Omega_j E_j}{3(1-\nu_j)}\left(\frac{2}{R_j^3}\int_0^{R_j}\tilde{c}\,r^2\,dr - \frac{1}{r^3}\int_0^{r}\tilde{c}\,r^2\,dr - \tilde{c}\right) \tag{39}$$

where $\tilde{c}$ is the concentration change from the initial value, ν_j is the Poisson's ratio, and E_j is the Young's modulus of active materials. The hydrostatic stress is [28]

$$\sigma_h = (\sigma_r + 2\sigma_t)/3 = \frac{2\Omega_j E_j}{9(1-\nu_j)}\left(\frac{3}{R_j^3}\int_0^{R_j}\tilde{c}\,r^2\,dr - \tilde{c}\right) \tag{40}$$

Substituting Eq. 40 into Eqs. 35 and 37

$$\begin{aligned}\frac{\partial c_{s,j}(r,t)}{\partial t} = D\Bigg[&\frac{\partial^2 c_{s,j}(r,t)}{\partial r^2} + \frac{2}{r}\frac{\partial c_{s,j}(r,t)}{\partial r} + \theta_j\left(\frac{\partial c_{s,j}(r,t)}{\partial r}\right)^2 \\ &+ \theta_j c\left(\frac{\partial^2 c_{s,j}(r,t)}{\partial r^2} + \frac{2}{r}\frac{\partial c_{s,j}(r,t)}{\partial r}\right)\Bigg]\end{aligned} \tag{41}$$

$$J_{st} = -D_{s,j}\left(1 + \theta_j c_{s,j}(r,t)\right)\frac{\partial c_{s,j}(r,t)}{\partial r} \quad at\ r = R_j \tag{42}$$

where $\theta_j = \frac{2{\Omega_j}^2 E_j}{9RT(1-\nu_j)}$.

Eqs. 1 and 2 are replaced by Eqs. 41 and 42, respectively, in the proposed SP model to calculate the solid phase concentration, and J^{Li} is replaced with J_{st} in Eq. 3. In this way, the stress model is coupled with the proposed SP model with accurate electrolyte physics.

3. RESULTS AND DISCUSSION

In order to demonstrate the effectiveness of the proposed model, the $LiMn_2O_4$-LiC_6 battery chemistry from Doyle et al. [10] was adopted in this work. The parameters used in the simulation are listed in Table 1. All of the models were simulated on a computer using the Windows operating system with a 1.9GHz Intel Xeon CPU and 24 GB of RAM. The P2D model (denoted "P2D"), conventional SP model (denoted "SP"), and proposed SP model (denoted "proposed model") with/without stress consideration were simulated in Matlab with a COMSOL-Matlab LiveLink function. The computation time was recorded via a Time Portions of Code in Matlab. Each model used the same sampling period (1s) and a 1C discharge rate for 2810s (4.2V to 3V) to compare the computational efficiency. The Matlab program execution times for each model are listed in Table 2. The computational time of the SP model (19.0s) and the proposed model (19.2s) were reduced by 65%, as compared to the P2D model (55.0s). In addition, when

the stress field is added, the computational time of the P2D and the proposed SP model increases by 14s and 3.1s, respectively, reducing the time by 68% with the SP model.

Table 1. Values of parameters used in the simulations.

Parameter	Value	Description	Ref
L_n	1×10^{-4}	Thickness of the negative electrode (m)	[10]
L_s	52×10^{-6}	Thickness of the separator (m)	[10]
L_p	183×10^{-6}	Thickness of the positive electrode (m)	[10]
ε_n	0.375	Porosity of the negative electrode	[10]
ε_s	1	Porosity of the separator	[10]
ε_p	0.444	Porosity of the positive electrode	[10]
D_e	7.5×10^{-11}	Diffusion coefficient in electrolyte (m^2s^{-1})	[10]
k_j	2×10^{-6}	Reaction rate constant ($m^{2.5}mol^{-0.5}s^{-1}$)	[10]
F	96487	Faraday's constant (C mol^{-1})	
t_+	0.363	Cationic transport number	[10]
i_{app}	17.5×C-rate	Crate times 1C discharge current density(Am^{-2})	[10]
c_0	2000	Initial concentration (mol m^{-3})	[10]
$D_{s,n}$	3.9×10^{-14}	Solid-phase Li diffusivity, negative electrode (m^2s^{-1})	[10]
$D_{s,p}$	1×10^{-13}	Solid-phase Li diffusivity, positive electrode (m^2s^{-1})	[10]
R_n	12.5×10^{-6}	Particle radius, negative electrode (m)	[10]
R_p	8×10^{-6}	Particle radius, positive electrode (m)	[10]
R	8.314	Universal gas constant (J mol^{-1} K^{-1})	
T	298.15	Ambient temperature (K)	
E_s	10	LMO Young's modulus (GPa)	[55]
E_n	60	LiC_6 Young's modulus (GPa)	[33]
v_s	0.3	LMO Poisson's ratio	[55]
v_n	0.25	LiC_6 Poisson's ratio	[33]
Ω_s	3.499×10^{-6}	LMO partial molar volume	[26]
Ω_n	4.926×10^{-6}	LiC_6 partial molar volume	[26]
$C_{max,\,pos}$	22860	Positive maximum concentration (mol m^{-3})	[10]
$C_{max,\,neg}$	26390	Negative maximum concentration (mol m^{-3})	[10]

Table 2. Comparison of P2D model, SP model, and proposed model computation times for 1C discharge.

Model	Computation time (s)	
	without stress consideration	with stress consideration
P2D	55.0	69.0
SP	19.0	22.0
Proposed model	19.2	22.3

3.1. ELECTROLYTE CONCENTRATION DISTRIBUTION AND ELECTROLYTE POTENTIAL DIFFERENCE

In order to verify the proposed model, the electrolyte concentration distributions of the analytical equations (Eqs. 14, 16 and 28) were compared with the numerical solutions of the governing equations with the boundary conditions given in Eqs. 6-12, 17. The results of the electrolyte concentration distribution are shown in Fig. 2a. Using the parameters in Table 1, the concentration change for a 1C discharge is displayed in Fig. 2a as a function of position, x, at different times, t. The prediction error between the second-order analytical equations and the P2D model is a result of reduced degrees of freedom in the empirical equation for the electrolyte concentration. In addition, the accuracy of the proposed model increased over time (0.82% maximum error at 30 s to 0.36% maximum error at 1500 s) because the coefficients a_k were derived based on steady-state conditions.

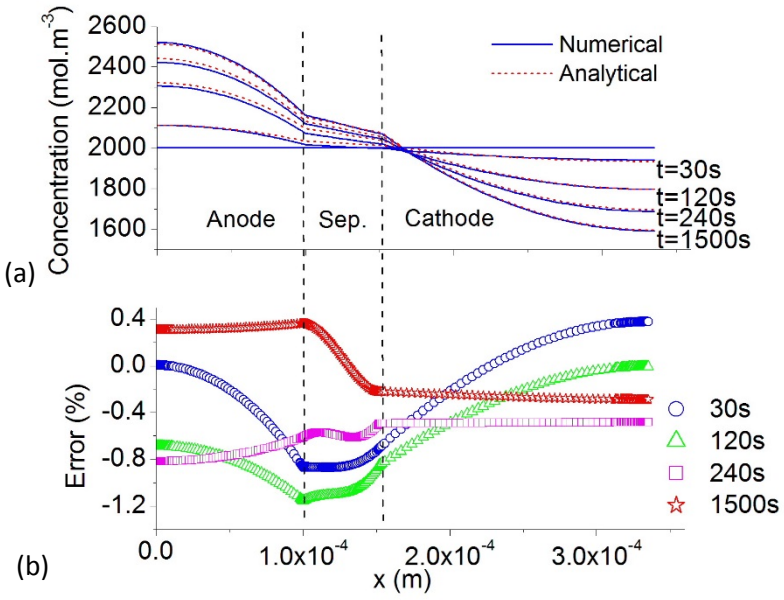

Figure 2. (a) Comparison of the electrolyte concentration distribution at different times for a 1C discharge rate, (b) percentile errors between solutions.

The electrolyte concentrations for a 1C discharge as a function of time at the interface regions within a cell as shown in Fig. 3. The four selected interfaces are the interface between the current collector and the negative electrode, the interface between the negative electrode and the separator, the interface between the separator and the positive electrode, and the interface between the positive electrode and the current collector. As shown in Fig. 3, the concentration profiles at the electrode-current collector and electrode-separator interface agreed well (< 0.1% error) with the numerical solution. Compared with similar second-order analytical solutions [22, 25], the model proposed in this paper improved the electrolyte profile in the positive electrode. At the electrode-current collector interface, the maximum concentration error is reduced from 2% [22] and 4% [5] to 0.8%, where the battery voltage is calculated from the electrolyte potential at this point. Further, when comparing the model based on the third-order solution [23], this model and the model in [23] can accurately capture the physics of the electrolyte concentration at C-rates below 1C. However, for higher C-rates, the voltage profile in [23] showed a maximum error of about 4% at a 5C discharge with the volumetric mean flux, while the results of this study showed a 1.9% maximum error at a 5C discharge with a simpler second-order expression. Additionally, this approximate solution can be applied to any type of operating condition, as well as the galvanostatic discharge condition.

In order to validate the model under dynamic loading, simulations of the Dynamic Stress Test (DST) and the Highway Fuel Economy Test (HWFET) were conducted. These tests are designed by the United States Advanced Battery Consortium to test EV and HEV batteries [37-39]. The electrolyte potential difference profiles for the DST and HWFET are plotted in Fig. 4. For the dynamic loading simulations, the initial electrolyte

concentration was updated by the last value from the previous step (i.e. $c_0 = c_e(x,0)$ at $t=0$ and $c_0 = c_e(x,t-\Delta t)$ at $t \neq 0$) to capture the electrolyte concentration dynamic profile. Compared to the HWFET simulation, the DST simulation are less fluctuating but have higher C-rate loads. Therefore, the error from electrolyte potential difference at high C-rates [22] will be more critical. For this reason, the errors will accumulate, leading to the deviation between the proposed SP and P2D models for the DST simulation. In general, Fig. 4 shows that the results from the proposed SP model agree well (average error < 0.03V) with those from the P2D model simulations. Therefore, the form for the approximate solution given by Eq. 31 is validated as being effective for the dynamic operating scenarios seen in EV and HEV applications. In summary, the approximate solution obtained in this study can be used to accurately describe the variation in the electrolyte concentration with respect to position and time for different operating scenarios.

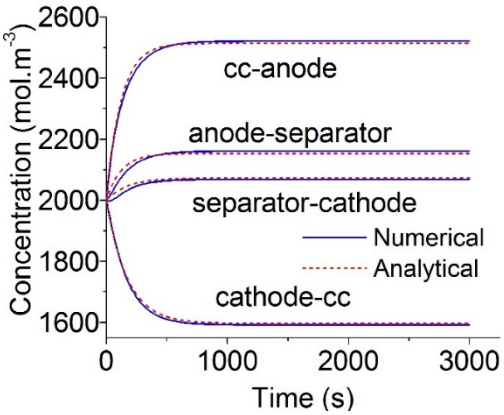

Figure 3. Comparison of concentrations that vary with time at selected interfaces for 1C charge rate.

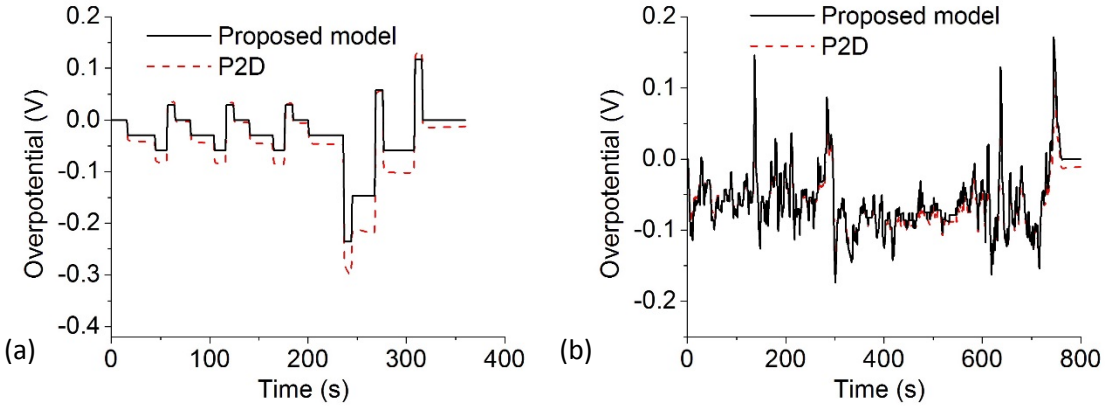

Figure 4. Electrolyte potential difference profile for (a) DST simulation and (b) HWFET simulation.

Table 3. Average error of proposed SP model and SP model.

Model	0.2C (%)	1C (%)	3C (%)	5C (%)	10C (%)
SP	0.049±0.035	0.183±0.101	0.975±0.574	1.533±0.887	8.041±0.434
Proposed model	0.032±0.023	0.146±0.064	0.630±0.331	0.935±0.608	4.417±0.841

3.2. CELL VOLTAGE RESPONSE

In this section, the cell voltage was simulated from 4.2 to 3 V for different C-rates (0.2C, 1C, 3C, 5C, and 10C) based on Eqs. 5 and 31. The results were then compared with the P2D model results in Fig. 5. As shown in Figs. 5a and 5b, both the SP and proposed SP models agree well with the P2D model results (0.0020 root mean square error (RMSE)) for a 0.2C discharge rate. However, for higher C-rates, the proposed SP model results (with RMSE of 0.0048 for 1C, 0.0249 for 3C, 0.0379 for 5C, and 0.1509 for 10C) were much closer than the SP results (RMSE of 0.0079 for 1C, 0.0380 for 3C, 0.0689 for 5C, and 0.2766 for 10C), as shown in Figs. 5c to 5j. The increased error at higher C-rates between the proposed SP and P2D models was because the electrolyte

potential difference error increases with increasing C-rates as discussed in Section 2. The uniform reaction distribution (Eqs. 1 and 4) used in the proposed SP model also differed from the results of the P2D model with non-uniform reaction distribution [22]. However, the proposed SP model reduced the average voltage error (shown in Table 3) compared to the SP model. In addition, with a short period of discharge time (at the beginning of discharge), the proposed model showed only a very small maximum error (0.01% to 0.21% for 0.2C to 3C), as compared to the rest of the discharge time. Thereby one of the shortcomings of the SP model has been overcome. Modern batteries, especially for HEVs, can operate at more than 10C, which is encountered during the DST [39, 40]. The case of 10C rate (Figs. 5g and 5h) demonstrated that the error rate increased considerably in the case of SP model, as compared to the case of the proposed SP model. In conclusion, results for the proposed SP model were in good agreement with those from the P2D model. The voltage error was reduced considerably (reduced 39.98% RMSE), as compared to the voltage errors resulting from the SP model.

The DST and HWFET were used to validate the proposed SP model for dynamic loads. As shown in Fig. 6, the proposed SP model for both the HWFET and the DST showed a considerable improvement in accuracy (reduced 55.8% RMSE for HWFET and 25% RMSE for DST) compared to the SP model. As previously discussed, the proposed SP model was more accurate at short periods of discharge time and higher C-rates, as compared to the SP model, indicating the proposed SP model is capable of accurately predicting cell voltage for dynamic loads.

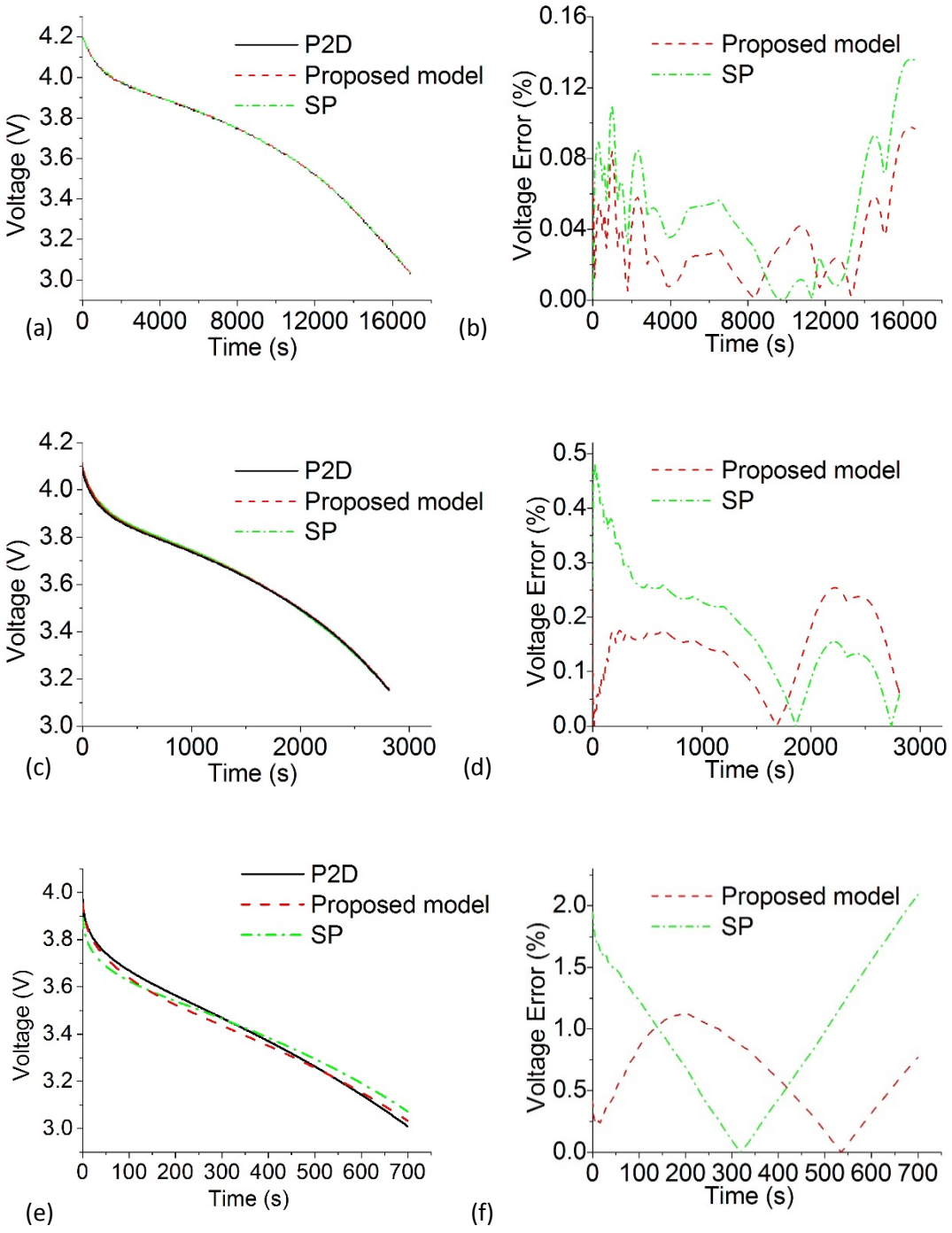

Figure 5. Comparison of time-dependent voltage responses and errors for P2D, SP, and proposed models for 0.2C (a and b), 1C (c and d), 3C (e and f), 5C (g and h), and 10C (i and j) galvanostatic discharges.

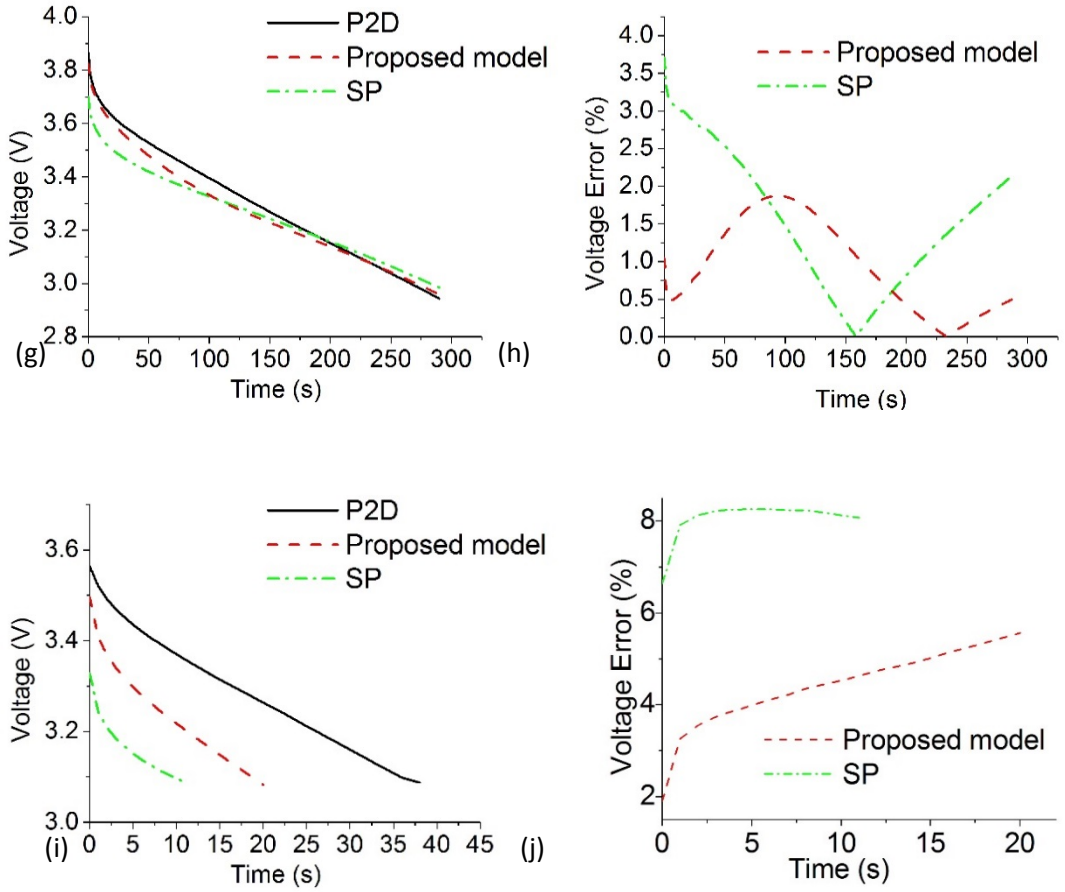

Figure 5. Comparison of time-dependent voltage responses and errors for P2D, SP, and proposed models for 0.2C (a and b), 1C (c and d), 3C (e and f), 5C (g and h), and 10C (i and j) galvanostatic discharges. (Cont.)

3.3. STRESS EFFECTS

Based on Eqs. 41 and 42, the stress model was coupled with the proposed SP model. In order to analyze the impact of stress on battery performance, three different galvanostatic discharge cases were conducted (i.e. 0.2, 1, and 3C). The results for simulations using the proposed SP model, with and without coupling to the stress model, are shown in Fig. 7.

Including the stress model produced negligible effects (maximum error < 0.01V) in the voltage profile for a 0.2C discharge. However, as shown in Figs. 7c, 7d, 7i, and 7j,

the voltage difference between the proposed SP model with and without stress increases with increasing C-rate, producing a maximum error of 0.16 V at the end of the 3C discharge. In addition, the effect of stress on anode surface concentration was more pronounced when the C-rate was higher, as shown in Figs. 7c, 7g, and 7k. However, the difference in cathode surface concentration was negligible, even for high C-rates, as shown in Figs. 7d, 7h, and 7l. To demonstrate the applicability of the stress model in online estimation, the stress effect was added in the DST and HWFET loading conditions and as shown in Figs. 7m and 7n, different voltage responses were also observed depending on whether or not the stress effect was included.

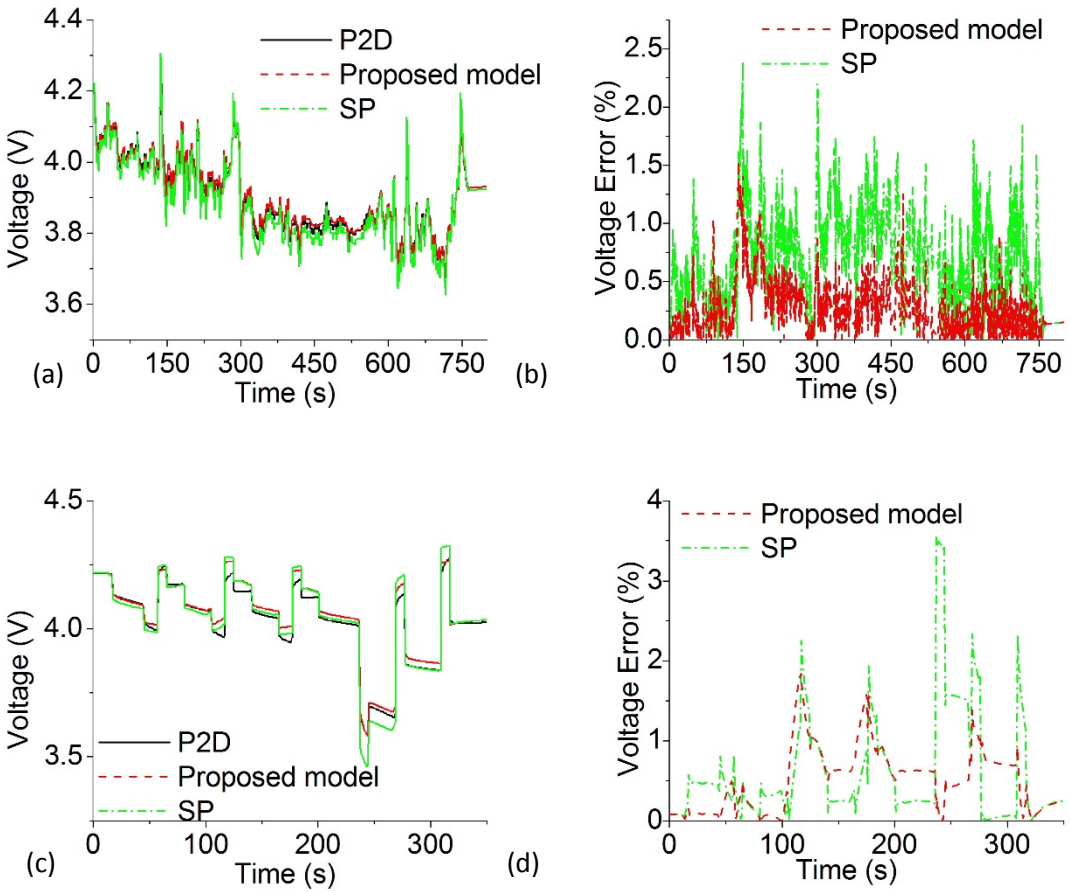

Figure 6. Cell voltage profile and errors for P2D, SP, and proposed models for HWFET operating scenario (a and b) and DST operating scenario (c and d).

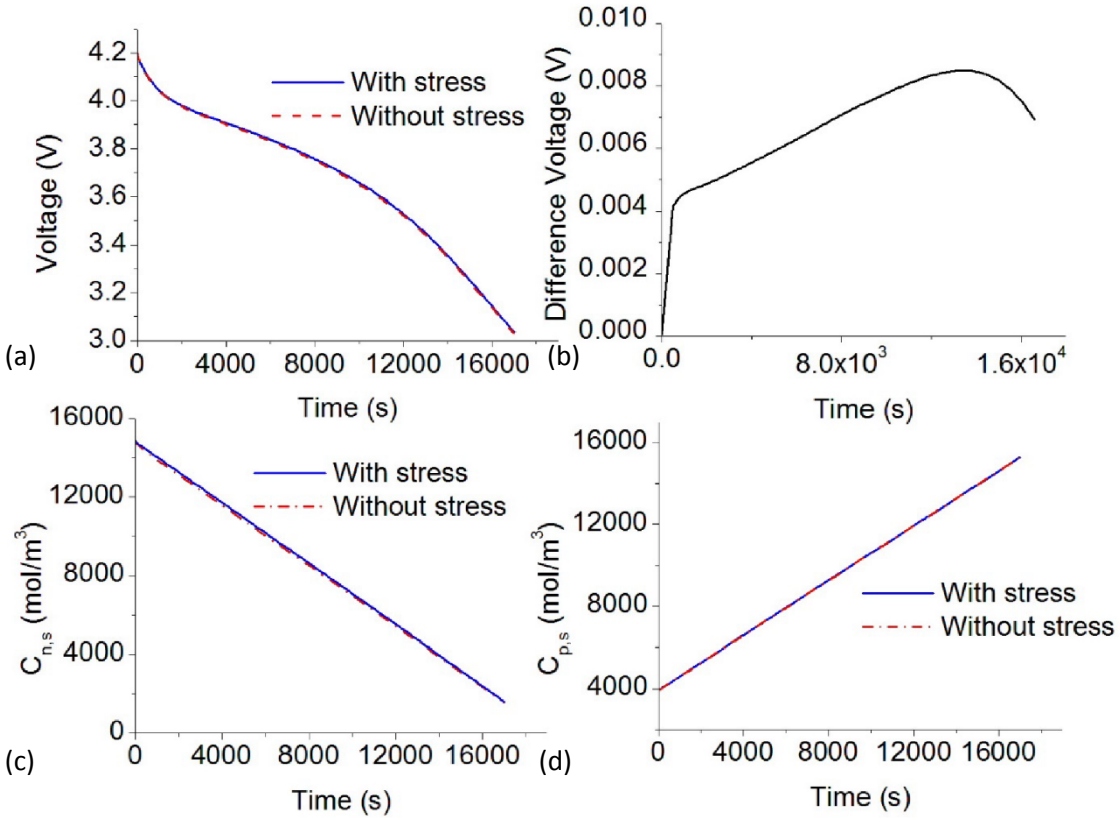

Figure 7. Comparison of proposed model with and without stress consideration (a) voltage comparison for 0.2C, (b) difference with and without stress consideration for 0.2C, (c) solid phase concentration in negative electrode surface for 0.2C, and (d) solid phase concentration in positive electrode surface for 0.2C; (e) voltage comparison for 1C, (f) difference with and without stress consideration for 1C, (g) solid phase concentration in negative electrode surface for 1C, and (h) solid phase concentration in positive electrode surface for 1C; (i) voltage comparison for 3C, (j) difference with and without stress consideration for 3C, (k) solid phase concentration in negative electrode surface for 3C, and (l) solid phase concentration in positive electrode surface for 3C; (m) voltage comparison for HWFET and (n) voltage comparison for DST.

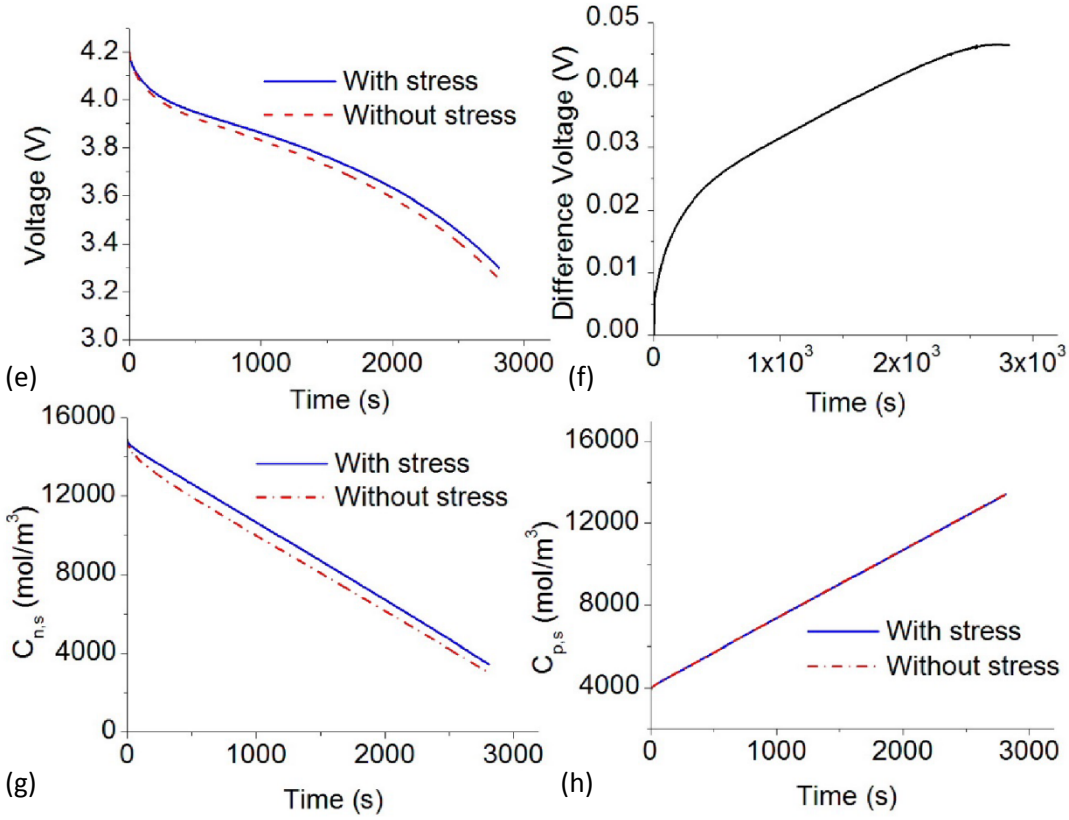

Figure 7. Comparison of proposed model with and without stress consideration (a) voltage comparison for 0.2C, (b) difference with and without stress consideration for 0.2C, (c) solid phase concentration in negative electrode surface for 0.2C, and (d) solid phase concentration in positive electrode surface for 0.2C; (e) voltage comparison for 1C, (f) difference with and without stress consideration for 1C, (g) solid phase concentration in negative electrode surface for 1C, and (h) solid phase concentration in positive electrode surface for 1C; (i) voltage comparison for 3C, (j) difference with and without stress consideration for 3C, (k) solid phase concentration in negative electrode surface for 3C, and (l) solid phase concentration in positive electrode surface for 3C; (m) voltage comparison for HWFET and (n) voltage comparison for DST. (Cont.)

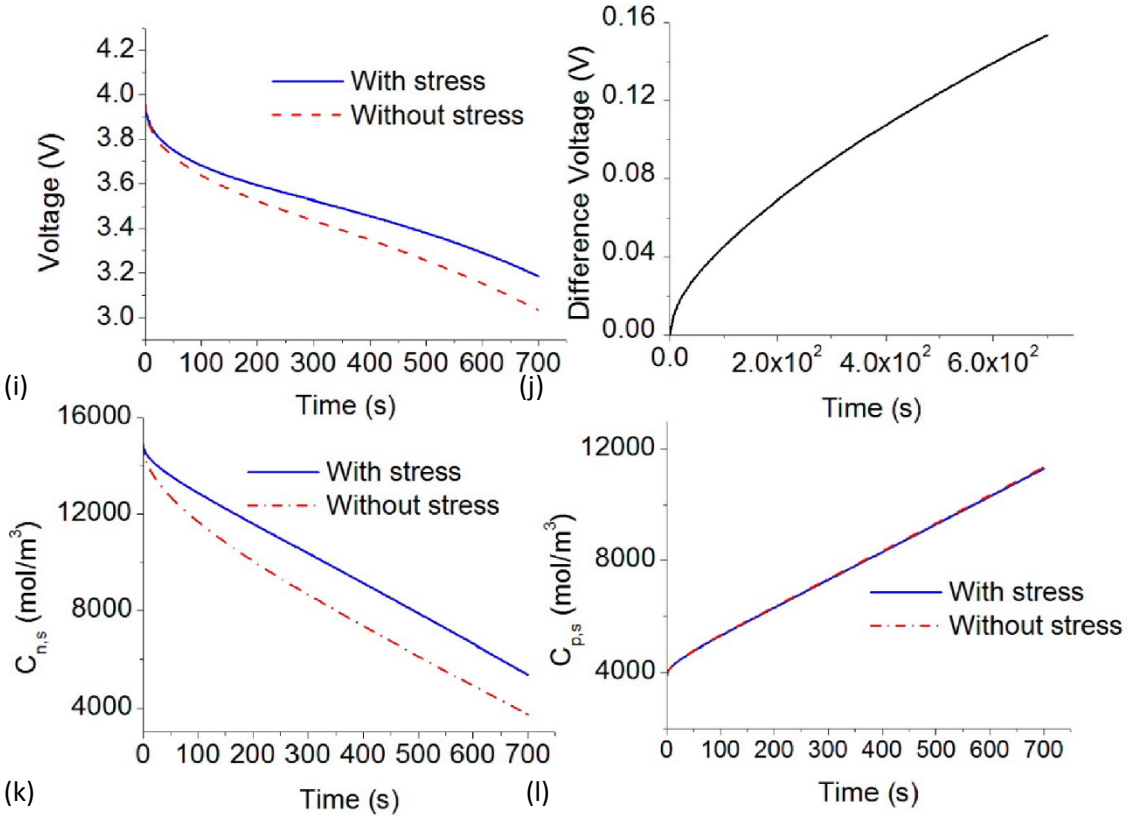

Figure 7. Comparison of proposed model with and without stress consideration (a) voltage comparison for 0.2C, (b) difference with and without stress consideration for 0.2C, (c) solid phase concentration in negative electrode surface for 0.2C, and (d) solid phase concentration in positive electrode surface for 0.2C; (e) voltage comparison for 1C, (f) difference with and without stress consideration for 1C, (g) solid phase concentration in negative electrode surface for 1C, and (h) solid phase concentration in positive electrode surface for 1C; (i) voltage comparison for 3C, (j) difference with and without stress consideration for 3C, (k) solid phase concentration in negative electrode surface for 3C, and (l) solid phase concentration in positive electrode surface for 3C; (m) voltage comparison for HWFET and (n) voltage comparison for DST. (Cont.)

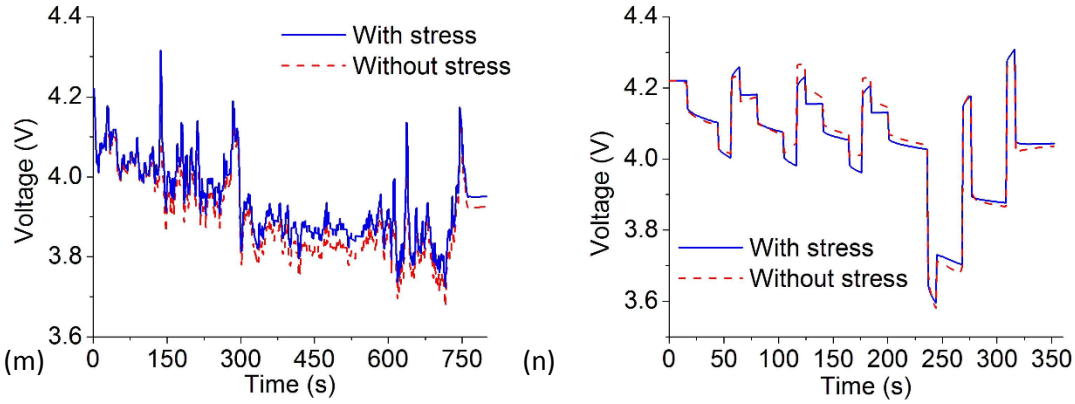

Figure 7. Comparison of proposed model with and without stress consideration (a) voltage comparison for 0.2C, (b) difference with and without stress consideration for 0.2C, (c) solid phase concentration in negative electrode surface for 0.2C, and (d) solid phase concentration in positive electrode surface for 0.2C; (e) voltage comparison for 1C, (f) difference with and without stress consideration for 1C, (g) solid phase concentration in negative electrode surface for 1C, and (h) solid phase concentration in positive electrode surface for 1C; (i) voltage comparison for 3C, (j) difference with and without stress consideration for 3C, (k) solid phase concentration in negative electrode surface for 3C, and (l) solid phase concentration in positive electrode surface for 3C; (m) voltage comparison for HWFET and (n) voltage comparison for DST. (Cont.)

Based on Eq. 42, it can be seen that stress increases diffusivity, leading to a considerable change in the anode surface concentration, thereby affecting the voltage responses. In Eq. 42, the diffusivity, $D_{s,j}(1+\theta_j C_{s,j}(r,t))$, depends on the coefficient θ_j and the li-ion concentration, $C_{s,j}(r,t)$, at each electrode [28], and θ_j, depends on materials' mechanical properties. Various mechanical properties for $LiMn_2O_4$ and LiC_6 have been reported. For instance, the Young's modulus of $LiMn_2O_4$ has been measured to be 25 GPa using a vibrating-reed measurement [41] and was measured to be 10 GPa using an elastic spectroscopy [42]. The difference was due to the fact that the chemical composition of each sample was different [41, 42]. Several battery modeling papers regarding $LiMn_2O_4$ [26, 42] have used a Young's modulus of 10 GPa that was measured using an elastic spectroscopy. In the present work, 10 GPa was selected because the target material was

similar to that used in the reported experiment, and it was assumed that it was independent of the amount of lithium content. For the $LiMn_2O_4$ cathode, the maximum increase in diffusivity is $\theta_p \times C_{s,p,max} = 0.358$, where $\theta_p = 1.56\times10^{-5}$ m^3/mol and $C_{s,p,max}$ = 22,860 mol/m^3. However, for the stiff graphite anode, the maximum increase in diffusivity is $\theta_p \times C_{s,n,max} = 4.59$, where $\theta_n = 1.74\times10^{-4}$ m^3/mol and $C_{s,n,max}$ = 26,390 mol/m^3. Therefore, the effect of stress on the anode diffusivity is much more significant than the effect of stress on the cathode diffusivity due to the order of magnitude difference in the coefficient, θ_j. The difference of θ_j is due to the difference at molar volume, Ω_j, Young's modulus, E_j, as shown in Eq. 42 and Table. 1. The trend of the stress-diffusion coupling impact on battery performance is in agreement with the published results.

Diffusion-Induced Stress (DIS) and Stress-Enhanced Diffusion (SED) have been carefully studied and analyzed for decades [28, 32, 43-50]. Experimentally, as evidence of DIS, mechanical failures of active materials (such as cracking, fracture, and delamination) have been observed through different approaches, such as SEM [43-45], AFM [45-47], and other *in situ* observation methods [48, 49]. For SED, most of the studies have been based on numerical simulations because it is difficult to decouple the effects of DIS and SED [28, 32, 45, 50, 51], and a few of experimental investigated were studied the effect of stress on diffusivity [52-53] and on the battery voltage profile [54]. The coupled SED and DIS phenomenon were also analyzed by a finite deformation model, thereby accounting for the full coupling between diffusion and stress evolution [50]. Ref. 50 indicated that the SED would increase the diffusion of the electrode and Ref. 28 also noted that considering SED effect would result in a lower concentration in

the cathode during discharge due to the enhanced solid phase diffusivity. The observed impact of stress field on diffusivity and voltage profile (Fig. 7) in this work agree quite well with the results in the literature [28, 50], in which the contribution of stress to diffusion was small at low lithium concentrations and SED became more pronounced as the lithium concentration increased. In conclusion, the proposed SP model, coupled with the stress model, indicated that it was necessary to consider an SED model capture the real battery physics governed by the coupling between stress and diffusion. This is especially important when using stiff materials or when operating at high charge and discharge rates as shown in Fig.7.

4. SUMMARY AND CONCLUSIONS

A low-order battery model was developed that incorporates stress-enhanced diffusion and electrolyte concentration distribution into a modified single particle model. An approximated analytical solution was derived for the electrolyte concentration distribution by solving the mass transport equation in the electrolyte of a li-ion cell. It has a simpler form than the P2D model and provided computational efficiency that is faster than that of the P2D model (almost 3 times faster in calculation time), and more accurate than that of the SP model (reduced 33.8% average voltage error). It was confirmed that this approximate solution can be applied to any combination of operating scenarios, including constant charge/discharge, short/long interval, and rest period, as well as the dynamic loads. From comparisons of the electrolyte concentration distributions and the potential difference profiles for various discharge conditions, it was concluded that the

approximate solution is reliable and can be used to predict cell voltages with less than 0.630±0.331% voltage error for C-rates up to 3C. In addition, coupling between the proposed SP model and a stress-model was considered. As a result, the effects of stress on cell voltage and solid phase concentrations was captured. The effect of stress has been found to non-negligible because it is important for medium to high C-rate operating conditions, and high-energy density materials or rigid materials. Therefore, the proposed model considering both nonuniformly dispersive electrolyte and stress-enhanced diffusivity is more accurate than the conventional SP model for predicting cell voltage without losing computational efficiency.

REFERENCES

[1] L. Lu, X. Han, J. Li, J. Hua, and M. Ouyang, *Journal of Power Sources*, 226, 272 (2013).

[2] V. Ramadesigan, P. W. Northrop, S. De, S. Santhanagopalan, R. D. Braatz, and V. R. Subramanian, *Journal of The Electrochemical Society*, 159, R31 (2012).

[3] D. Andrea, *Battery Management Systems for Large Lithium Ion Battery Packs*: Artech house, (2010).

[4] M. Woon, X. Lin, A. Ivanco, A. Moskalik, C. Gray, and Z. Filipi, in *SAE 2011 World Congress and Exhibition*, (2011).

[5] N. A. Chaturvedi, R. Klein, J. Christensen, J. Ahmed, and A. Kojic, *IEEE Control Systems,* 30, 49 (2010).

[6] R. Klein, N. A. Chaturvedi, J. Christensen, J. Ahmed, R. Findeisen, and A. Kojic, *American Control Conference*, 6618 (2010).

[7] J. Prins-Jansen, J. D. Fehribach, K. Hemmes, and J. De Wit, *Journal of The Electrochemical Society,* 143, 1617 (1996).

[8] K. Smith and C. Y. Wang, *Journal of Power Sources,* 161, 628 (2006).

[9] M. W. Verbrugge and B. J. Koch, *Journal of The Electrochemical Society,* 150, A374 (2003).

[10] M. Doyle, T. F. Fuller, and J. Newman, *Journal of the Electrochemical Society,* 140, 1526 (1993).

[11] S. Santhanagopalan and R. E. White, *Journal of Power Sources,* 161, 1346 (2006).

[12] V. R. Subramanian, V. Boovaragavan, V. Ramadesigan, and M. Arabandi, *Journal of The Electrochemical Society,* 156, A260 (2009).

[13] X. Hu, S. Li, and H. Peng, *Journal of Power Sources,* 198, 359 (2012).

[14] "FreedomCAR battery test manual for power-assist hybrid electric vehicles", *US Department Of Energy/ID-11069*, (2003).

[15] D. Dees, E. Gunen, D. Abraham, A. Jansen, and J. Prakash, *Journal of The Electrochemical Society,* 155, A603(2008).

[16] M. Schlesinger, *Modeling and Numerical Simulations,* Springer-Verlag, New York, (2009).

[17] G. Ning and B. N. Popov, *Journal of The Electrochemical Society,* 151, A1584 (2004).

[18] S. Santhanagopalan, Q. Guo, P. Ramadass, and R. E. White, *Journal of Power Sources,* 156, 620 (2006).

[19] V. R. Subramanian, V. D. Diwakar, and D. Tapriyal, *Journal of The Electrochemical Society,* 152, A2002 (2005).

[20] Q. Zhang and R. E. White, *Journal of Power Sources,* 165, 880 (2007).

[21] A. Guduru, P. W. Northrop, S. Jain, A. C. Crothers, T. R. Marchant, and V. R. Subramanian, *Journal of Applied Electrochemistry,* 42, 189 (2012).

[22] W. Luo, C. Lyu, L. Wang, and L. Zhang, *Microelectronics Reliability,* 53, 797 (2013).

[23] S. K. Rahimian, S. Rayman, and R. E. White, *Journal of Power Sources,* 224, 180 (2013).

[24] N. Baba, H. Yoshida, M. Nagaoka, C. Okuda, and S. Kawauchi, *Journal of Power Sources,* 252, 214 (2014).

[25] X. Han, M. Ouyang, L. Lu, and J. Li, *Journal of Power Sources*, 278, 802 (2015).

[26] J. Dahn, *Physical Review B,* 44, 9170 (1991).

[27] L. Beaulieu, S. Beattie, T. Hatchard, and J. Dahn, *Journal of The Electrochemical Society,* 150, A419 (2003).

[28] X. Zhang, W. Shyy, and A. M. Sastry, *Journal of The Electrochemical Society,* 154, A910 (2007).

[29] W. H. Woodford, Y. M. Chiang, and W. C. Carter, *Journal of The Electrochemical Society,* 157, A1052 (2010).

[30] K. Zhao, M. Pharr, J. J. Vlassak, and Z. Suo, *Journal of Applied Physics,* 108, 073517 (2010).

[31] J. Li, A. K. Dozier, Y. Li, F. Yang, and Y. T. Cheng, *Journal of The Electrochemical Society,* 158, A689 (2011).

[32] J. Park, W. Lu, and A. M. Sastry, *Journal of The Electrochemical Society,* 160, X3 (2013).

[33] Y. Qi, H. Guo, L. G. Hector, and A. Timmons, *Journal of The Electrochemical Society,* 157, A558 (2010).

[34] M. Guo, G. Sikha, and R. E. White, *Journal of The Electrochemical Society,* 158, A122 (2011).

[35] D. Di Domenico, A. Stefanopoulou, and G. Fiengo, *ASME Journal of Dynamic Systems, Measurement, and Control,* 132, 061302 (2010).

[36] E. Prada, D. Di Domenico, Y. Creff, J. Bernard, V. Sauvant-Moynot, and F. Huet, *Journal of The Electrochemical Society,* 159, A1508 (2012).

[37] C. Silva, M. Ross, and T. Farias, *Energy Conversion and Management*, 50, 1635 (2009).

[38] H. He, R. Xiong, and J. Fan, *Energies,* 4, 582 (2011).

[39] Electric vehicle battery test procedures manual, *U.S. Advanced Battery Consortium*, Southfield, MI, USA, (2006).

[40] J. Wang, P. Liu, J. Hicks Garner, E. Sherman, S. Soukiazian, M. Verbrugge, H. Tataria, J. Musser, and P. Finamore, *Journal of Power Sources*, 196, 3942 (2011).

[41] J. Christensen and J. Newman, *Journal of The Electrochemical Society*, 153, A1019 (2006).

[42] X. Zhang, A. M. Sastry, and W. Shyy, *Journal of The Electrochemical Society*, 155, A542 (2008).

[43] M. R. Lim, W. I. Cho, and K. B. Kim, *Journal of Power Sources*, 92, 168 (2001).

[44] D. Wang, X. Wu, Z. Wang, and L. Chen, *Journal of Power Sources*, 140, 125 (2005).

[45] M. Chung, J. Seo, X. Zhang, and A. Sastry, *Journal of The Electrochemical Society*, 158, A371 (2011).

[46] J. Hun, M. Chung, M. Park, S. Woo, X. Zhang, and A. Marie, *Journal of The Electrochemical Society*, 158, A434 (2011).

[47] A. Clemencon, A. Appapillai, S. Kumar, and Y. Shao Horn, *Electrochimica Acta*, 52, 4572 (2007).

[48] V. A. Sethuraman, N. Van Winkle, D. P. Abraham, A. F. Bower, and P. R. Guduru, *Journal of Power Sources*, 206, 334 (2012).

[49] V. A. Sethuraman, M. J. Chon, M. Shimshak, V. Srinivasan, and P. R. Guduru, *Journal of Power Sources*, 195, 5062 (2010).

[50] Y. Gao and M. Zhou, *Journal of Applied Physics*, 109, 014310 (2011).

[51] R. Xu, and K. Zhao, *Journal of Electrochemical Energy Conversion and Storage*, 13. 030803 (2016).

[52] K.B. McAfee Jr, *The Journal of Chemical Physics*, 28, 218 (1958).

[53] F. Célarié, M. Ciccotti, and C. Marliere, *Journal of Non-Crystalline solids*, 353, 51 (2007).

[54] B. Lu, Y. Song, Q. Zhang, J. Pan, Y.T. Cheng, and J. Zhang, *Physical Chemistry Chemical Physics*, *18*, 4721 (2016).

[55] A. Paolone, R. Cantelli, G. Rousse, and C. Masquelier, *Journal of Physics: Condensed Matter*, 15, 457 (2003).

V. A SINGLE PARTICLE MODEL WITH CHEMICAL/MECHANICAL DEGRADATION PHYSICS FOR LITHIUM ION BATTERY STATE OF HEALTH (SOH) ESTIMATION

ABSTRACT

State of Health (SOH) estimation of lithium ion batteries is critical for Battery Management Systems (BMSs) in Electric Vehicles (EVs). Many estimation techniques utilize a battery model; however, the model must have high accuracy and high computational efficiency. Conventional electrochemical full-order models can accurately capture battery states, but they are too complex and computationally expensive to be used in a BMS. A Single Particle (SP) model is a good alternative that addresses this issue; however, existing SP models do not consider degradation physics. In this work, an SP-based degradation model is developed by including Solid Electrolyte Interface (SEI) layer formation, coupled with crack propagation due to the stress generated by the volume expansion of the particles in the active materials. A model of lithium ion loss from SEI layer formation is integrated with an advanced SP model that includes electrolytic physics. This low-order model quickly predicts capacity fade and voltage profile changes as a function of cycle number and temperature with high accuracy, allowing for the use of online estimation techniques. Lithium ion loss due to SEI layer formation, increase in battery resistance, and changes in the electrodes' open circuit potential operating windows are examined to account for capacity fade and power loss. In addition to the low-order implementation to facilitate on-line estimation, the model proposed in this paper provides quantitative information regarding SEI layer formation

and crack propagation, as well as the resulting battery capacity fade and power dissipation, which are essential for SOH estimation in a BMS.

1. INTRODUCTION

Lithium Ion Batteries (LIBs) are key energy storage devices for many applications due to their high energy and power densities, and are widely used in Electric Vehicles (EVs) and Hybrid Electric Vehicles (HEVs). A critical challenge, however, is the capacity degradation experienced during repeated charge/discharge cycles. Battery performance declines over time due to irreversible physical and chemical changes that naturally occur until the battery can no longer be used. Therefore, State of Health (SOH) estimation is an essential component of a Battery Management System (BMS) for a variety of energy storage systems in transportation and stationary applications [1, 2]. However, there are challenges in performing SOH estimation in a BMS. First, SOH cannot be directly measured. Here, SOH refers to the state of a battery's condition compared to its initial condition, and is expressed as a loss of capacity relative to the initial value. For instance, when the battery capacity in EVs/HEVs reaches 80% of its initial capacity, the battery is no longer considered usable [1].

Secondly, battery performance continuously degrades due to various mechanisms, both mechanical and chemical, which affect LIBs during their lifetime. Therefore, studying these mechanisms require long-term, in situ testing that typically requires the battery to be destroyed. Moreover, it is challenging to decouple the effects of each of these mechanisms on battery health and performance. Modern LIBs, which are fabricated

from a variety of anode and cathode materials, degrade due to a number of mechanisms that depend on the chemical nature of their constituent materials. In general, battery degradation mechanisms [3-6] include current collector corrosion, morphological changes of active materials, electrolyte decomposition, Solid Electrolyte Interphase (SEI) layer formation, and material dissolution. For example, carbonaceous materials, which are the most common anode materials in modern LIBs, have a significant amount of irreversible capacity loss during initial cycling as the SEI layer is formed on the carbon surface [3-5, 7].

Moreover, the SEI layer continues to grow due to the continuous reduction of the electrolyte and the reformation of the SEI layers, which re-consumes lithium ions and results in irreversible battery capacity loss. For instance, about 8-15% irreversible capacity loss due to lithium ion loss is expected for MesoCarbon MicroBeads [5]. Further, mechanical damage to the battery will accelerate chemical degradation. The basic function of an electrochemical material is fulfilled by ions entering the active materials due to an electrochemical potential gradient [8]. During this intercalation process, volume change causes considerable stresses inside the particles, leading to mechanical failures such as pulverization of, or cracks and fractures in, the active materials. These cracks generate new surfaces on the particle, which are then exposed to the electrolyte, leading to additional SEI layer formation and the acceleration of capacity fade and power loss [8-14].

Despite these difficulties, the foundation of many models of different battery aging mechanisms has been presented by the research community to predict battery life. The studies in [15-20] utilized physics-based models that provide very detailed

information regarding the battery electrochemical response. Capacity loss due to SEI layer formation was simulated through a continuum-scale mathematical model by considering the flux of the side reaction at the anode particle surface [15, 16] or by modifying the solid phase concentration to be a function of the cycle according to lithium ion loss [17-19]. The effect of mechanical degradation on capacity fade has also been simulated using a full order physics-based model [20]. These models solve governing physical equations, which include mass conservation and charge conservation in the solid and electrolyte phases, as well as kinetic reactions at the interface between the solid and electrolyte.

A comprehensive and detailed state-of-the-art review of SOH estimation for LIBs has been conducted in [21]. These methods can be categorized as experimental techniques and adaptive methods. Experimental techniques depend on recorded experimental data and previous knowledge about the effect of the operating conditions such as temperature, cycle number, SOC, current magnitude, etc. on the battery cycle life [21]. Although these methods are easy to implement onboard BMSs, their validity is limited to the calibration data used in their development.

Furthermore, the wide range of operating conditions encountered in different battery applications, such as EVs, necessitates the use of an adaptive SOH estimation methods. Adaptive methods utilize parameters from battery models to estimate the SOH. Electrochemical models can provide highly accurate predictions of the battery behavior while providing insight into internal battery phenomena. Due to these advantages, these models are gaining popularity in recent years in the development of different BMS

functionalities, such as SOH estimation. For BMSs, however, there is still a challenge in incorporating battery physics and degradation during on-line estimation.

Although a high fidelity electrochemical modes are ideal for the detailed analysis of battery phenomena, they are too computationally intensive to be efficiently utilized in a BMS [22]. This has led to efforts to reduce the complexity of electrochemical models, such as the studies in [23, 24] that reduced the electrochemical model proposed by Doyle et al. [25] into a form suitable for a BMS.

To further simplify battery models, most studies employ an Equivalent Circuit Model (ECM), which describes the battery dynamic behavior as a voltage source and a series of resistors and capacitors [26] and is widely used in BMSs due to the model's low complexity and ease of online implementation. However, ECM models have no physical significance, which leads to low fidelity and limited prediction capability. In addition, the prediction of battery side-reactions is not feasible due to the difficulty of obtaining the battery internal dynamic characteristics. Therefore, higher accuracies can be attained only by considering time-variant model parameters.

The Single Particle (SP) model is a common type of reduced-order model. The SP model strikes the necessary balance between full order electrochemical models and ECMs, and is becoming a popular model in recent years for SOC and SOH estimation [27-31]. It assumes both electrodes are composed of multiple uniform sized spherical particles, and that the current distribution is uniform across both electrodes. Thus, each electrode can be approximated by a single spherical particle. The SP model is described by a set of ordinary differential equations, yet it is directly derived from comprehensive electrochemical models and, thus, explicitly retains many important battery properties

with high computational efficiency. The drawbacks of the SP model are that the accuracy of the SP model suffers at high C-rates due to the lack of electrolyte physics and degradation is not taken into account [28].

In this work, to address these issues, a capacity degradation model with chemical/mechanical degradation mechanisms [17] is modified and integrated with an advanced SP model. This capacity degradation model is able to predict battery capacity loss as a function of cycle number and temperature, including SEI layer formation and growth, coupled with mechanical fatigue analysis.

Further, the proposed model is able to predict voltage responses based on a physical analysis, which is an advanced method for predicting the voltage profiles as a function of cycle, compared to the existing method based on a look-up table [17, 18]. The method utilizing a look-up table limited the model to the cases with well-defined tables. Also, the existing models did not consider the kinetic reactions associated with the SEI layer.

In particular, the stress model in the existing approach was idealized as it was based on a single particle, which could lead to unrealistic results in certain cases. In general, the SOH of lithium ion batteries is related to capacity fade due to lithium loss and power fade due to impedance increase. Then, the capacity loss and impedance rise affect the voltage profile, which is critical information for battery management. However, most SOH estimation studies only consider the capacity change without any prediction of the voltage profile change [27-30].

Our proposed model can be directly applied to SOH estimation for battery management systems. In addition, the model is well validated with different loading

conditions, including static and dynamic loadings. Further, the coupling between different physical behaviors, such as mechanical response and electrochemical reaction, is important physics in several energy related materials. The proposed approach can be applied to many other similar systems. In this paper, therefore, three unsolved challenges in the literature are addressed:

(1) Capacity fade due to multiple degradation mechanisms and corresponding voltage change is predicted based on the physical analysis of an SP model, which does not require any lookup tables, unlike existing models.

(2) Realistic boundaries between multiple particles are considered to calculate particle stress, which is then linked to capacity degradation. Note: the idealized single particle used for the electrochemical model is different from the single-particle based stress model in [17].

(3) A systematic study is conducted by analyzing the relationship between the battery system's parameters (e.g., particle size, C-rate, temperature) and capacity loss due to SEI layer formation and growth on the particle and cracked surfaces.

The remainder of this paper is organized as follows. Section 2 describes the proposed methods to integrate lithium ion loss with an advanced SP model, the stress evaluation based on multiple surrounding particles, and the prediction of capacity fade due to chemical and mechanical degradation.

In Section 3, the degradation model validation and the analysis of model parameter effects on capacity and power losses are given, followed by a summary and conclusions in Section 4.

Nomenclature

a	crack length (m)	l_{cr0}	Initial crack width (m)
a_0	Initial crack length (m)	L_{SEI}^0	initial SEI layer thickness (m)
$brug$	Bruggeman coefficient	L_i	Electrode thickness (m)
c_0	Initial concentration (mol m^{-3})	M_{SEI}	Molecular weight of compounds constituting SEI (gm mol^{-1})
$C_{max,\ pos}$	Positive maximum concentration (mol m^{-3})	n_{Li}	Initial total number of lithium ions inside battery
$C_{max,\ neg}$	Negative maximum concentration (mol m^{-3})	n_{SEI}	Consumed lithium ion for 1 mol of SEI layer formation
D_e	Diffusion coefficient in electrolyte (m^2s^{-1})	N	Cycle number
$D_{s,j}$	Solid-phase Li diffusivity (m^2s^{-1})	Q_0	Battery capacity after formation cycle
E_{a1}	Activation energy for crack propagation (kcal mol^{-1})	Q_{in}	Battery capacity before SEI layer formation cycle
E_{a2}	Activation energy for SEI layer growth (kcal mol^{-1})	Q_g	Graphite specific capacity (Ah g^{-1})
E	Young's modulus of electrode material (N m^{-2})	Q_N	Capacity after N^{th} cycle
F	Faraday's constant (C mol^{-1})	R	Universal gas constant (J mol^{-1} K^{-1})
$i = p/s/n$	Positive/separator /negative	r_j	Particle radius (m)
I_{app}	Applied current density (Am^{-2})	R_{SEI}^0	Initial SEI layer resistance (Ω)
$j = p/n$	Positive/negative	t_+	Cationic transport number
J_j^{Li}	Molar flux density (mol $s\ m^{-2}$)	$V(0)\|_N$	Initial voltage at each cycle (V)
k_i	Electrolyte conductivities (S m^{-1})	ε_i	Electrode porosity
k_j	Reaction rate constant ($m^{2.5}mol^{-0.5}s^{-1}$)	ρ_{cr}	Number of cracks per unit area of particle (m^{-2})
k_0	Crack propagation coefficient	ρ_g	Graphite density (g cm^{-3})
K_{SEI0}	SEI layer growth coefficient	ρ_{SEI}	Density of SEI films (g m^{-3})
k_{SEI}	SEI layer conductivity (S m^{-1})	Ω	Partial molar volume of solute (m^3mol^{-1})

2. CAPACITY FADE MECHANISM MODELING

2.1. SINGLE PARTICLE MODEL COUPLED WITH CAPACITY DEGRADATION

Figure 1a is a schematic overview of the simulation process in this paper. The model requires the initial battery voltage, temperature, and current input. Those initial values can be obtained from measurements. Next, the model predicts capacity fade by

calculating lithium loss due to SEI layer formation and growth on the surface of particles and cracks. Then, the capacity changes are coupled with the SP model to predict the voltage profile based on the change in the lithium ion concentration. These steps are repeated for each cycle.

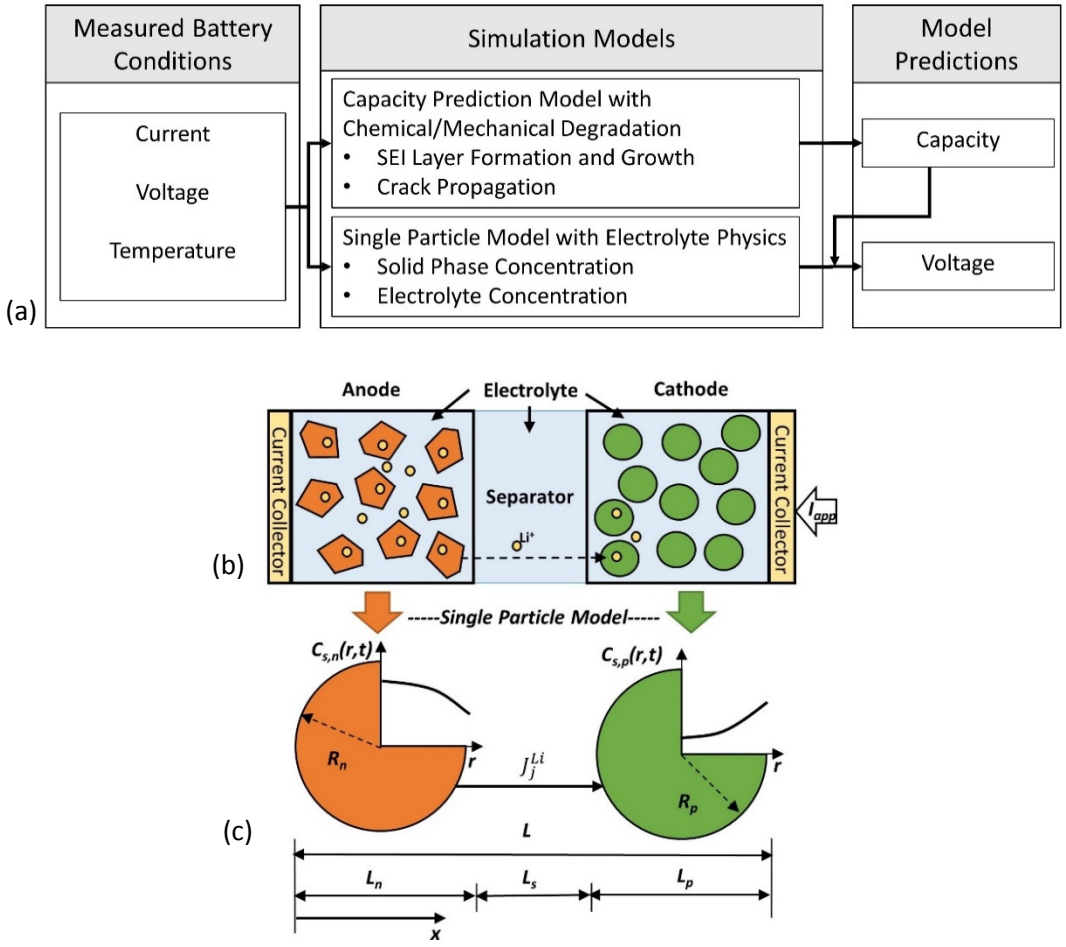

Figure 1. Schematic diagrams for (a) overview of the proposed simulation processes, (b) a lithium ion battery composed of an anode, a separator, and a cathode, (c) representing two single particles for each electrode in the SP model, (d and e) coupled degradation mechanism between SEI layer formation and crack propagation on particle, and (f) capacity fade due to the lithium loss caused by SEI layer formation and growth.

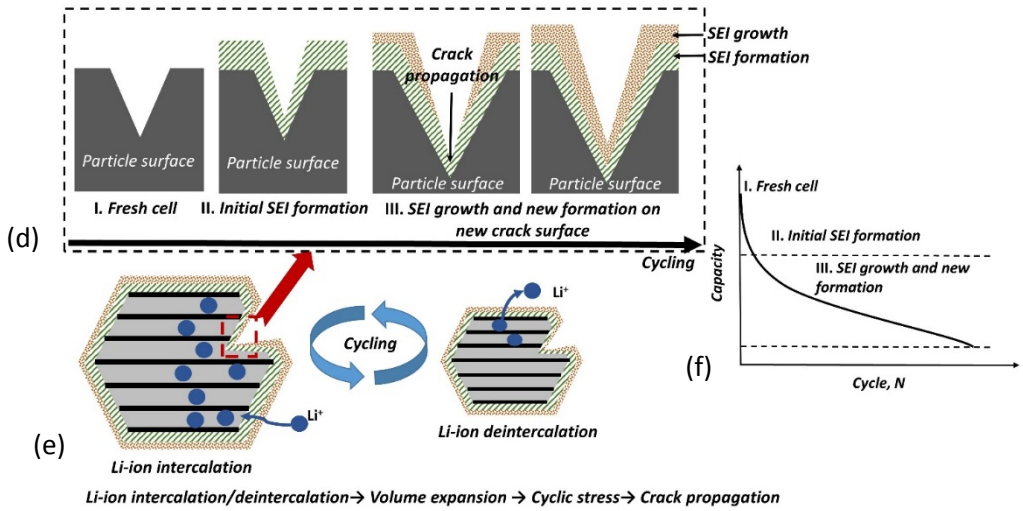

Figure 1. Schematic diagrams for (a) overview of the proposed simulation processes, (b) a lithium ion battery composed of an anode, a separator, and a cathode, (c) representing two single particles for each electrode in the SP model, (d and e) coupled degradation mechanism between SEI layer formation and crack propagation on particle, and (f) capacity fade due to the lithium loss caused by SEI layer formation and growth. (Cont.)

Figure 1b is a schematic diagram of a lithium ion cell composed of two electrodes (a solid matrix in an electrolyte solution) and a separator (electrolyte solution), while Figure 1c shows the concept of the SP model, which represents each electrode with a single particle. Pesudo-2D (P2D) models, which are based on porous electrode theory using concentrated solutions, are widely used for battery modeling [24,25]. This model describes lithium ion transport through the use of one-dimensional (battery thickness, *x*, direction) charge and mass conservation laws along with the thickness direction, as well as the diffusion process for individual active particles, which is implemented in the radial direction of the particles,. The kinetic reaction at the particle surfaces is described by the Butler-Volmer equation. The P2D model consists of ten coupled nonlinear partial differential equations for the mass and charge balance in the solid and electrolyte phases [24,25].

In the SP model it is assumed that the current passing through the electrode is uniformly distributed over all of the particles inside the electrode. Therefore, as shown in Figure 1c, each electrode can be modeled as a single spherical particle, and the governing partial differential equations can be simplified into a set of algebraic equations. Further, the complex multi-physics of the battery can be implemented in a relatively simple manner based on the assumption of uniformity of intercalation flux in the SP model [32], which leads to each reaction inside electrode, such as diffusion, transportation, diffusion-induced stress, and side-reactions, has a uniform impact on each particle. However, the existing SP models do not consider the concentration and potential distribution in electrolyte phase; therefore, model accuracy suffers at high C-rates. In order to overcome this limitation and increase model accuracy, this study uses the authors' recently developed SP model [33], in which the electrolyte physics was added.

The remaining challenge is to consider battery degradation, in particular, the coupled degradation mechanisms between mechanical crack propagation and SEI layer formation and growth. Figures 1d and 1e show the proposed SP model considering the coupling between them. In the mechanical part (Figure 1e), the repeated stress due to the (de)intercalation is calculated, and corresponding crack propagation is predicted. In the SEI layer formation and growth model, the updated crack propagation is used to estimate the new SEI layer formation on the surface of newly-formed cracks. More details are discussed in Section 2.2.

To calculate the terminal voltage, the SP model considers the solid phase potential difference between the end sides of both electrodes based on Bulter-Volmer equation [33]

$$V_t(t) = \Phi_{1,p}(t)\big|_{x=L} - \Phi_{1,n}(t)\big|_{x=0}$$
$$= \left(\eta_p + \Phi_{2,p}(t)\big|_{x=L} + U_p\left[\frac{c_{s,p,surf}(t)}{c_{s,p,max}}\right]\right) \quad (1)$$
$$- \left(\eta_n + \Phi_{2,n}(t)\big|_{x=0} + U_n\left[\frac{c_{s,n,surf}(t)}{c_{s,n,max}}\right]\right)$$

$$\eta_j(t) = \frac{2RT}{F}\ln\left[m_j(t) + \sqrt{m_j^2(t)+1}\right] \quad (2)$$

where $m_j(t) = \frac{J_j^{Li}}{2k_j c_{s,j,max} c_e^{0.5}\left[1-\frac{c_{s,j,surf}(t)}{c_{s,j,max}}\right]^{0.5}\left(\frac{c_{s,j,surf}(t)}{c_{s,j,max}}\right)^{0.5}}$.

$$\Phi_{2,p}(t)\big|_{x=L} - \Phi_{2,n}(t)\big|_{x=0}$$
$$= (1-t_+)\frac{2RT}{F}\ln\frac{c_{e,p}(L,t)}{c_{e,n}(0,t)} - \frac{I_{app}}{2}\left(\frac{L_n}{k_n^{eff}} + \frac{2L_s}{k_s^{eff}} + \frac{L_p}{k_p^{eff}}\right) \quad (3)$$

where $c_{s,j,max}$ is the maximum solid phase concentration, k_j is the reaction rate constant and $j = p/n$ denotes the positive/negative electrode, respectively, R is the universal gas constant, T is temperature, F is Faraday's constant, $\Phi_{1,j}$ is the solid-phase potential, and U_j is the Open-Circuit Potential (OCP).

The OCP, in general, is a function of the normalized surface concentration, $c_{s,j,surf}(t)/c_{s,j,max}$. The variable $k_i^{eff} = k_i\varepsilon_i^{brug}$, *brug* denotes the bruggeman coefficient, where k_i is the electrolyte conductivities [34]. The variable L_i is the electrode thickness, $i = p/s/n$ denotes the positive/separator /negative electrode, respectively, I_{app} is the applied current density, t_+ is cationic transport number in the electrolyte, J_j^{Li} is the electrochemical reaction rate, and $c_{e,i}(x,t)$ is the electrolyte concentration [33].

Equation 1 does not include battery capacity reduction effects and, therefore, does not exhibit changes in the voltage profile as the battery is cycled. In order to integrate capacity loss mechanisms into the SP model, the initial concentrations, $c_{s,p}(0)\big|_{N+1}$ and $c_{s,n}(0)\big|_{N+1}$ for the cathode and anode, respectively, at the beginning of the $(N+1)^{th}$ cycle must be calculated. Here, one cycle is when the battery is fully discharged and then fully charged. The number of available lithium ions inside the battery after the N^{th} cycle can be calculated based on the capacity after the N^{th} cycle, Q_N, and the initial total number of lithium ions inside the battery, n_{Li}. From charge conservation in the anode and cathode at the $(N+1)^{th}$ cycle

$$\varepsilon_{s,p} L_p c_{s,p}(0)\big|_{N+1} + \varepsilon_{s,n} L_n c_{s,n}(0)\big|_{N+1} = \frac{Q_N}{Q_0} n_{Li} \tag{4}$$

where Q_0 is the battery capacity after the formation cycle (described below).

In general, battery vendors suggest a maximum voltage for charging; therefore, a scenario of full charging to that voltage was assumed in this paper. The initial voltage at the N^{th} cycle, $V(0)$, which is constant at the beginning of each discharge cycle, is

$$U_p\left[\frac{c_{s,p}(0)\big|_{N+1}}{c_{s,p,max}}\right] - U_n\left[\frac{c_{s,n}(0)\big|_{N+1}}{c_{s,n,max}}\right] = V(0) \tag{5}$$

The initial concentrations in the anode and cathode are estimated by solving Equations 4 and 5. It should be noted that as the battery capacity decreases with each cycle, the corresponding OCP curve windows change, affecting the concentration

polarization. The reduction in capacity can be attributed to lithium ion loss during the formation and growth of SEI layers on the surfaces of anode active material particles and cracks.

2.2. SINGLE PARTICLE BASED CHEMICAL/MECHANICAL DEGRADATION MODEL

2.2.1. Capacity Degradation. A schematic diagram of SEI formation, growth, and additional formation and its growth due to crack propagation is shown in Figures 1d and 1e. A fresh battery cell (Stage I) undergoes a process called ‘formation cycle’ to stabilize the cell by forming an initial SEI layer. During the formation cycle, a uniform SEI layer, mainly containing Li_2O, LiF, and Li_2CO_3, is formed on the freshly exposed particle surfaces and initial crack surface due to electrolyte reduction (Stage II). Once the battery is in use, the SEI layer tends to grow, especially when the battery is used at high temperatures (Stage III). In addition, the diffusion-induced stress due to changes in the battery volume causes cracks to propagate on the particle surface, creating new surfaces that are exposed to the electrolyte and on which new SEI layers will form. This repeated process continuously consumes lithium ions, causing capacity fade as shown Figure 1f. The growth model developed by Rutooj et al. [17] is utilized in this work and coupled with the SP model given in this paper to include degradation mechanisms due to SEI layer formation and growth.

Solid electrolyte interface layer formation and growth can be categorized into four different mechanisms including: (1) initial SEI layer formation during the formation cycle; (2) growth on the initially formed SEI layer; (3) initial SEI layer formation on

newly formed surfaces due to cracking; and (4) growth of the initially formed SEI layers on the surfaces created by cracking.

During the formation cycle, the particle will be fully covered with an SEI layer. The initial SEI layer thickness, L_{SEI}^{0}, can be estimated based on the capacity loss after the formation cycle, which is assumed to be 10% [5, 17]

$$L_{SEI}^{0} = \frac{0.1 Q_{in} M_{SEI}}{A_{initial} n_{SEI} \rho_{SEI} F} \tag{6}$$

where the Q_{in} is the battery capacity before the SEI layer formation cycle process is conducted, $A_{initial}$ is the particle surface area before the SEI layer formation cycle, n_{SEI} is the number of lithium moles lost for every mole of SEI layer formed, ρ_{SEI} is the SEI layer density, and M_{SEI} is the molecular weight of compounds constituting the SEI layer.

To evaluate the surface area of the SEI layer, defects must be considered that exist in active material particles and will be the seeds that initiate cracks. The initial surface area of the single particle is the surface area of a sphere with initial defects [17]

$$A_{initial} = 4\pi r_n^2 (1 + 2\rho_{cr} l_{cr0} a_0) \tag{7}$$

where l_{cr0} is the initial defect width, a_0 is the initial defect length, r_n is the particle radius, and ρ_{cr} is the number of cracks per unit area.

Since SEI layer growth generally follows a parabolic pattern, SEI layer thickness, L_{SEI}, growth rate per cycle number (N) can be expressed as

$$\frac{dL_{SEI}}{dN} = \frac{1}{2} K_{SEI} N^{-\frac{1}{2}} \tag{8}$$

where $K_{SEI} = K_{SEI0} e^{\frac{-E_{a2}}{RT}}$, E_{a2} is the activation energy for SEI layer thickness growth, and K_{SEI0} is the SEI layer growth coefficient [17].

The SEI layer will grow on the initial particle surface, thus, combining Equations 6-8, the volume change of the SEI layer growth on the initial SEI layer, i.e., the second degradation mechanism, is

$$\frac{dV_{SEI,2}}{dN} = 2\pi r_n^2 (1 + 2\rho_{cr} l_{cr0} a_0) K_{SEI} N^{-\frac{1}{2}} \tag{9}$$

As the number of battery cycles increases, not only does the formed SEI layer continue to grow, the initial defects also grow and form cracks on the surfaces of the particles due to repeated stress on the active material particles. These cracks result in new interface area with the electrolyte. Paris' law is used here to model such crack propagation [35]

$$\frac{da}{dN} = k\left(\sigma_{\theta,cor} b\sqrt{\pi a}\right)^m \tag{10}$$

where a is the crack length and m and b are empirical constants that depend on material properties [36]. The crack propagation coefficient can be expressed based on the Arrhenius form, $k = k_0 e^{\frac{-E_{a1}}{RT}}$, where E_{a1} is the activation energy for crack propagation and k_0 is the crack propagation coefficient [17].

In order to determine the crack growth rate, the maximum cyclic stress on the particle surface is used. Most studies concerning stress analysis in battery models are

based on a single isolated particle under a steady-state condition and calculate the maximum tensile stress to be [37]

$$\sigma_{\theta,max} = \frac{-E\Omega I_{app}}{45(1-\nu)\varepsilon_n l_n}\left(\frac{r_n^2}{FD_{s,n}}\right)^2 \tag{11}$$

where E is Young's modulus, ν is Poisson's ratio of the electrode material, and Ω is the partial molar volume of the solute. This model computes the stress levels in a single particle caused by diffusion; however, it does not consider the constraint imposed on a particle's boundary when it is in contact with other particles. This analysis is extended in this paper to a more realistic situation where there is a network of particles and calculates the maximum stress at the particle surface based on the strain during charge and discharge.

The driving force for lithium ion diffusion can be obtained by the gradient of the concentration and mechanical strain energy and, correspondingly, the mass conservation of lithium ions becomes [11]

$$\frac{\partial c_{s,j}(r,t)}{\partial t} = D_{s,j}D\left[\nabla^2 c_{s,j}(r,t) - \frac{\Omega}{RT}\nabla c_{s,j}(r,t)\cdot\nabla\sigma_h - \frac{\Omega c_{s,j}(r,t)}{RT}\nabla^2\sigma_h\right] \tag{12}$$

where σ_h is the hydrostatic stress of a spherical particle [11]. The stress-strain relationship considering the effect of intercalation is [38,39]

$$\varepsilon_{mn} = \frac{1}{E}[(1+\nu)\sigma_{mn} - \nu\sigma_{kk}\delta_{mn}] + \frac{\left(c_{s,j}(r,t) - c_{s,j}(r,0)\right)\Omega}{3}\delta_{mn} \tag{13}$$

where ε_{mn} is the components of strain tensor (m, n, k = 1, 2, 3), σ_{mn}/σ_{kk} are components of stress tensor, and δ_{mn} is the Kronecker delta.

The stress acting on a particle is now calculated based on a network of particles, and the particle surface stress ratios are normalized based on the stress of a single particle with a radius of 5 μm [17]. The schematic of a network of 5 particles is shown in Figure 2a and the stress increase ratio for networks with 3-7 particles is shown in Figure 2b as a function of particle size. As shown in Figure 2b, when using a network of particles the stress increases linearly with particle size, which is in stark contrast to the quadratic relationship between the stress and particle radius for a single particle as given in Equation 11. Comparing to a network of seven particles, the stress ratio differences for 3-6 particles are 9.58%, 3.77%, 1.45%, and 1.3%, respectively; therefore, a network of 5 particles is used in this study. The stress equation for a single particle (Equation 11) is calibrated using a correction factor, β, which is based on the stress calculation with a network of 5 particles divided by the stress calculated from Equation 11. The corrected maximum stress is

$$\sigma_{\theta,cor} = \beta \left[\frac{-E\Omega I_{app}}{45(1-\nu)\varepsilon_n l_n} \left(\frac{r_n^2}{FD_{s,n}} \right)^2 \right] \tag{14}$$

The total area change associated with crack propagation due to stress for each cycle is

$$\frac{dA_{cr}}{dN} = 8\pi r_n^2 \rho_{cr} l_{cr0} k \left(\sigma_{\theta,cor} b \sqrt{\pi a_0} \right)^m \left(\frac{a}{a_0} \right)^{\frac{m}{2}} \tag{15}$$

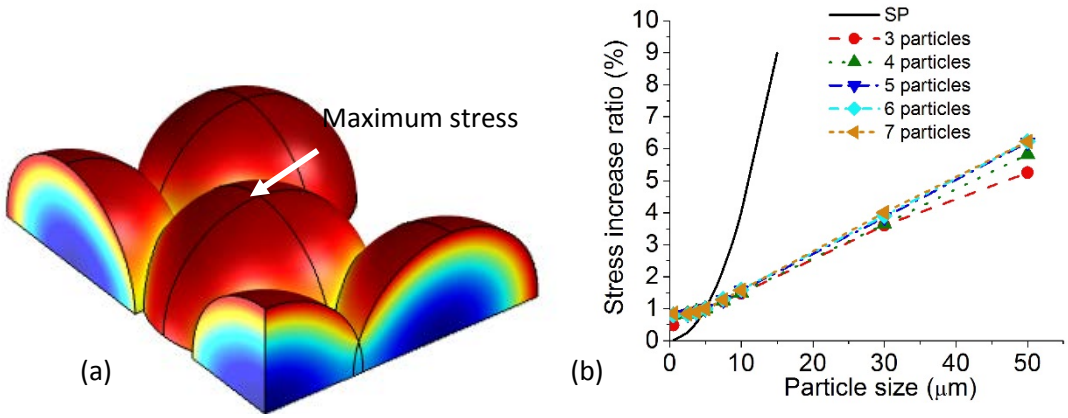

Figure 2. (a) Schematic of five particles and (b) Particle surface stress ratio as a function of particle size for various numbers of particles.

Correspondingly, the volume change of the SEI layer formation at newly exposed surfaces per cycle, i.e., the third degradation mechanism, is

$$\frac{dV_{SEI,3}}{dN} = L_{SEI}^{0} 8\pi r_n^2 \rho_{cr} l_{cr0} k\left(\sigma_{\theta,cor} b\sqrt{\pi a_0}\right)^m \left(1 + \frac{2-m}{2} k\left[\sigma_{\theta,cor} b\sqrt{\pi}\right]^m a_0 \left(\frac{m}{2-m}\right) N\right)^{\frac{m}{2-m}} \tag{16}$$

The growth rate of the SEI layer formed on cracks as they grow, i.e., the fourth degradation mechanism, is

$$\frac{dV_{SEI,4}}{dN} = \sum_{i=1}^{N-1} \left(8\pi r_n^2 \rho_{cr} l_{cr0} k\left(\sigma_{\theta,cor} b\sqrt{\pi a_0}\right)^m \left(1 + \frac{2-m}{2} k\left[\sigma_{\theta,cor} b\sqrt{\pi}\right]^m a_0 \left(\frac{m}{2-m}\right) N\right)^{\frac{m}{2-m}} \right)_i \left(\frac{1}{2} K_{SEI} N^{-\frac{1}{2}}\right)_{N-i} \tag{17}$$

Finally, the total SEI layer growth rate is

$$\frac{dV_{SEI}}{dN} = \frac{dV_{SEI,2}}{dN} + \frac{dV_{SEI,3}}{dN} + \frac{dV_{SEI,4}}{dN} \tag{18}$$

Capacity decay can be calculated based on SEI layer growth. The initial battery capacity of a fresh cell, Q_{in} in Equation 6, is estimated to be

$$Q_{in} = q_r Q_g \left(\frac{4}{3}\pi r_n^3 \rho_g\right) \tag{19}$$

where Q_g is the specific capacity of graphite, ρ_g is the density of graphite. In a conventional lithium ion cell employing a substantially graphitic negative electrode, the negative's capacity is about 10% greater than that of the positive in order to avoid lithium plating on overcharge of the negative. For such a cell, q_r is assumed to be 0.9. [17].

The formation cycle is generally considering has 8 to 10% capacity loss, and then the battery capacity after the SEI formation cycle is

$$Q_0 = 0.9 Q_{in} \tag{20}$$

Then, the capacity fade rate per cycle after the formation cycle is

$$\frac{dQ_N}{dN} = -\frac{n_{SEI}\rho_{SEI}F}{M_{SEI}}\frac{dV_{SEI}}{dN} \tag{21}$$

2.2.2. Resistance Due To SEI Layer Formation And Growth. The SEI layer growth may also increase the cell resistance and impact battery power. Battery resistance increase is estimated by leveraging the work of Ning et al. [19]. The SEI layer resistance at the N^{th} cycle is

$$R_{SEI}|_N = \frac{L_{SEI}|_N}{k_{SEI}} \tag{22}$$

where k_{SEI} is the SEI layer conductivity and the SEI layer thickness at the N^{th} cycle is

$$L_{SEI}|_N = \frac{V_{SEI}|_N}{A_{cr}|_N} \tag{23}$$

The initial SEI layer resistance, R_{SEI}^0, is assumed to be on the same order as the electrolyte resistance [40]. Thus, k_{SEI} is calculated based on the initial SEI layer thickness and resistance

$$k_{SEI} = \frac{L_{SEI}^0}{R_{SEI}^0} \tag{24}$$

Finally, the cell terminal voltage, including the impact of initial concentration change (Equations 4 and 5), SEI layer resistance (Equation 22), and other polarizations effects such as activation and diffusion, is

$$V_t(t)|_{N+1} = U_p\left[\frac{c_{s,p,surf}(t)\big|_{N+1}}{c_{s,p,max}}\right] - U_n\left[\frac{c_{s,n,surf}(t)\big|_{N+1}}{c_{s,n,max}}\right] + \frac{2RT}{F}\left\{\ln\left[m_p(t) + \sqrt{m_p^2(t)+1}\right] - \ln\left[m_n(t) + \sqrt{m_n^2(t)+1}\right]\right\} + (1 - t_+)\frac{2RT}{F}\ln\frac{c_{e,p}(L,t)}{c_{e,n}(0,t)} - \frac{I_{app}}{2}\left(\frac{L_n}{k_n^{eff}} + \frac{2L_s}{k_s^{eff}} + \frac{L_p}{k_p^{eff}}\right) + R_{SEI}|_N I_{app} \quad (25)$$

In order to demonstrate the effectiveness of the developed model, the $LiFePO_4$/C battery chemistry is adopted in this work. The parameters used in the simulation studies conducted in this paper are listed in Table 1.

3. RESULTS AND DISCUSSION

3.1. VALIDATION OF DEGRADATION MODEL

3.1.1. Capacity Degradation Under a Constant Loading. To verify the proposed model, predicted battery capacity is compared with previously observed experimental data for a $LiFePO_4$/Graphite battery [41] as a function of cycle number and temperature from 15-60 ^oC for a discharge rate of 0.5C. As shown in Figure 3a, the simulated capacity fade matches the measured data well with fractional capacity Root Mean Square Errors (RMSEs) of 7.21×10^{-3}, 7.43×10^{-3}, and 10.3×10^{-3} at 15, 45, and 60 ^oC, respectively. As expected, the capacity fades at a faster rate as the temperature

increases. Despite its low-order structure, the developed model is in good agreement with the experimental data, indicating that the proposed capacity fade model based on single particle assumptions can describe the degradation of lithium ion batteries at different temperatures.

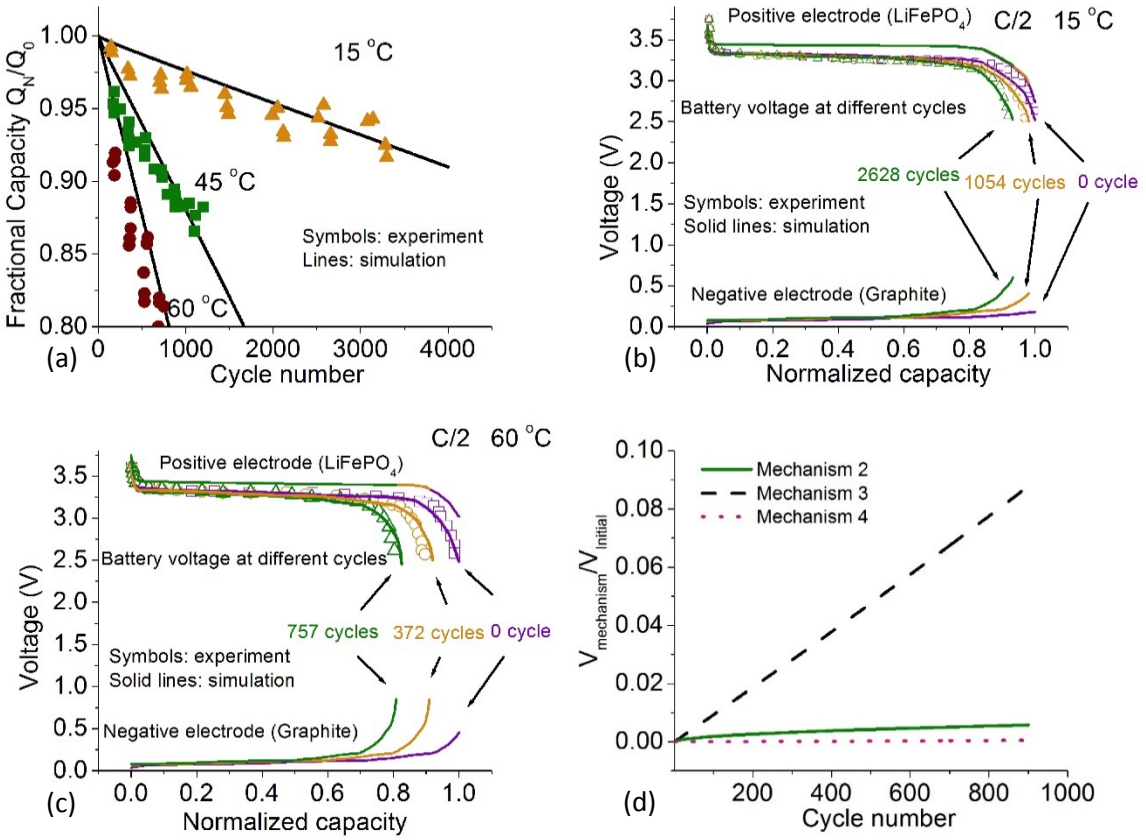

Figure 3. (a) Cell fractional capacity as a function of number of cycles with 0.5C, and simulation and experimental results for $LiFePO_4$/Graphite battery: open circuit voltages and voltage profiles for (b) 15 °C and (c) 60 °C, and (d) SEI layer volume ratio $V_{mechanism}/V_{initial}$ for mechanism 2 SEI layer growth on the initial SEI layer, mechanism 3 SEI layer formation on new crack surfaces, and mechanism 4 SEI layer growth on SEI layers formed on crack surfaces as a function of cycle number.

Table 1. Model parameters used in simulation studies.

Parameter	Value	Description	Reference
a_0	2×10^{-9}	Initial crack length (m)	[17]
$brug$	1.5	Bruggeman coefficient	[17]
c_0	1000	Initial concentration (mol m^{-3})	[17]
$C_{max,\,pos}$	22806	Positive maximum concentration (mol m^{-3})	[17]
$C_{max,\,neg}$	30555	Negative maximum concentration (mol m^{-3})	[17]
D_e	7.5×10^{-11}	Diffusion coefficient in electrolyte (m^2s^{-1})	[17]
$D_{s,n}$	10×10^{-14}	Solid-phase Li diffusivity, negative electrode (m^2s^{-1})	[17]
$D_{s,p}$	5.9×10^{-20}	Solid-phase Li diffusivity, positive electrode (m^2s^{-1})	[17]
E_{a1}	10.1	Activation energy for crack propagation (kcal mol^{-1})	Fitted
E_{a2}	5.791	Activation energy for SEI layer growth (kcal mol^{-1})	Fitted
E	3.3×10^{10}	Young's modulus of electrode material (N m^{-2})	[17]
F	96487	Faraday's constant (C mol^{-1})	
k_j	2×10^{-11}	Reaction rate constant ($m^{2.5}mol^{-0.5}s^{-1}$)	[17]
k_0	$1.62\text{x}10^{-16}$	Crack propagation coefficient	Fitted
K_{SEI0}	$7.195\text{x}10^{-11}$	SEI layer growth coefficient	Fitted
l_{cr0}	2×10^{-9}	Initial crack width (m)	[17]
L_n	$3.\ 8\times10^{-5}$	Negative electrode thickness (m)	[17]
L_p	8×10^{-5}	Positive electrode thickness (m)	[17]
L_s	2.5×10^{-5}	Separator thickness (m)	[17]
M_{SEI}	78.89	Molecular weight of compounds constituting SEI (gm mol^{-1})	[17]
n_{SEI}	2	Consumed lithium ion for 1 mol SEI layer formation	[17]
Q_g	0.339	Graphite specific capacity (Ah g^{-1})	[17]
R	8.314	Universal gas constant (J mol^{-1} K^{-1})	
r_n	5×10^{-6}	Particle radius, negative electrode (m)	[17]
r_p	5×10^{-8}	Particle radius, positive electrode (m)	[17]
R^0_{SEI}	$1\text{x}10^{-3}$	Initial SEI layer resistance (Ω)	[39]
t_+	0.363	Cationic transport number	
$V(0)\|_N$	4.2	Initial voltage at each cycle (V)	
ε_n	0.248	Negative electrode porosity	[17]
ε_p	0.367	Positive electrode porosity	[17]
ε_s	1	Separator porosity	[17]
ρ_{cr}	2.542×10^{18}	Number of cracks per unit area of particle (m^{-2})	[17]
ρ_g	2.26	Graphite density (g cm^{-3})	[17]
ρ_{SEI}	2.11×10^{6}	Density of SEI films (g m^{-3})	[17]
Ω	8.9×10^{-6}	Partial molar volume of solute (m^3mol^{-1})	[17]

Accurate voltage profile prediction as the battery goes through cycles of charging and discharging is a critical function of the BMS. The proposed model predicts the voltage profile based on the physics described in Equations 4, 5, and 25, which is different from the work in [17] that relied on a look-up table. Lithium ion losses due to SEI layer formation and growth affect not only the available battery capacity, but also the operating voltage window due to shifts in the OCP curves. Figures 3b and 3c show that the range of the anode (Li_xC_6) OCP curve shifts to the left due to lithium ion losses. On the other hand, the cathode (Li_xFePO_4) OCP curve does not shift despite the loss of lithium ions due to the unique long plateau of this curve. As a result of the coupling between the anode and cathode, the voltage profiles vary with the cycle number. The simulation results are in good agreement with an RMSE on the order of 1×10^{-2} (Table 2) compared to the experimental voltage profile in [41, 42]. Additionally, the simulation is able to capture the same behavior as the experimental observations in which they observed that the anode OCP window shifted to the left as the battery capacity decreased, and the cathode OCP window did not shift [17, 18].

Table 2. Root Mean Square Errors of voltage profile at C/2 with 15 ºC and 60 ºC.

	0^{th} cycle	1054^{th} cycle	2628^{th} cycle
C/2 and 15 ºC	54.4×10^{-3}	39.9×10^{-3}	35.0×10^{-3}
	0^{th} cycle	372^{th} cycle	757^{th} cycle
C/2 and 60 ºC	24.5×10^{-3}	57.8×10^{-3}	44.2×10^{-3}

Capacity fade is mainly due to the lithium ion loss resulting from the four mechanisms described above. The first mechanism (i.e., initial SEI layer formation) occurs before the battery is put into operation. Next, the effect of the other three

degradation mechanisms is analyzed in details. Figure 3d shows the contributions of mechanisms 2-4 as a ratio of the SEI volume formed due to each mechanism to the initial SEI volume formed during the formation cycle (i.e., mechanism 1). The newly-formed SEI volume ratio due to new crack surfaces (i.e., mechanism 3) reaches approximately 9% after 900 cycles, which is when the battery reaches 80% of its initial capacity, with a rate of 9.76×10^{-5} volume ratio per cycle, while the volume increase due to the growth of the initial SEI layer (i.e., mechanism 2) and the SEI volume formation due to growth on newly-formed crack surfaces (i.e., mechanism 4) are less than 1% after 900 cycles with rates of 5.25×10^{-6} and 5.68×10^{-7} volume ratio per cycle, respectively. Therefore, SEI layers formed on the cracks dominate the battery degradation.

3.1.2. Capacity Fade Under Dynamic Loading Conditions. The SEI layer formation mainly occurs during the charging process and, for typical EVs, batteries are charged using a Constant Current/Constant Voltage (CCCV) mode. Section 3.1.1 focused on a constant current case, while this section considers a case in which the charging current may be different at each cycle. For this dynamic loading condition, a random current loading (from 0 to 0.5 C-rate) is applied during changing at each cycle at 25 ^{o}C. Battery degradation results are shown in Figure 4 for a dynamic current profile and the corresponding average constant current profile. As shown in Figure 4b, the capacity fade when subjected to dynamic loading results in greater capacity fade (0.7% greater at 80% capacity loss) than when subjected to the dynamic profile's average current. This phenomenon, in which a dynamic current produces a faster degradation rate ($1.16\text{x}10^{-4}$ per cycle) than the constant current ($1.10\text{x}10^{-4}$ per cycle) as shown in Figure 4c, was observed in experimental data [43] for an electric vehicle battery under highway driving

loading profiles. In this experiment, the capacity fade with highway driving load profiles is slightly greater (approximately 0.1%) than the case with a constant current.

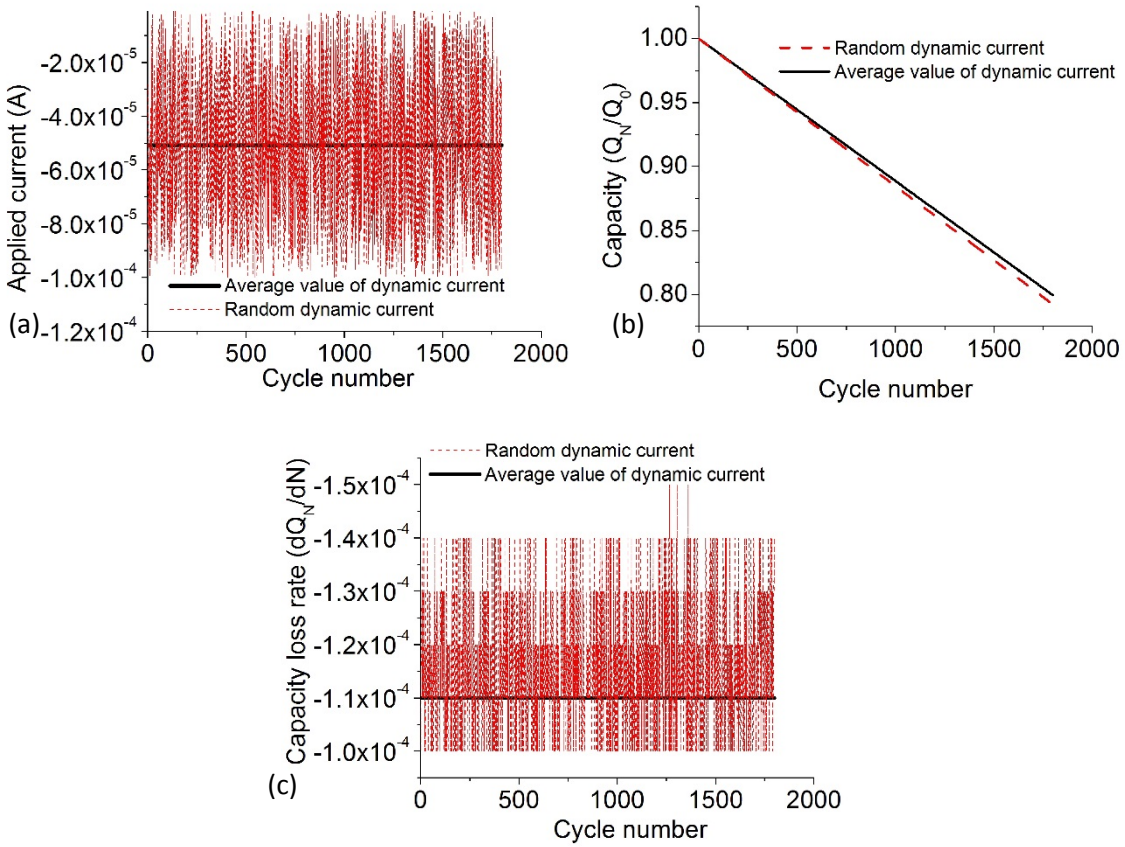

Figure 4. Battery degradation results: (a) dynamic and constant average applied currents, (b) cycle history of normalized capacity prediction for dynamic and constant applied currents, and (c) cycle history of capacity change cycle for dynamic and constant applied currents.

3.2. CAPACITY LOSS AND POWER LOSS ANALYSES

Crack propagation, $\Delta a/a_0$, defined as the ratio of the change in crack length to the initial crack length, is plotted in Figure 5 as a function of temperature, C-rate, and particle size (with β = 3.3, 1, and 0.4 for $0.5r_n$, r_n, and $2r_n$, respectively). As shown in this figure, all of the parameters have a significant impact on crack propagation and, hence, battery

cycle life. Lower temperatures can slow the growth of the SEI layer (Equation 8), and lower C-rates or smaller particle sizes can lower the stress level (Equation 14), both of which slow the crack growth rate (Equation 10) and, correspondingly, extend battery life. There is a lot of experimental evidence that stress can build up inside battery materials and there are also some experimental studies characterize the developed stress and cracks based on measurements from SEM and AFM [41, 44-47]. However, in all of the prior work, the crack growth inside particles was not monitored and, practically, it will be very hard to monitor stress at the particle level based on in-situ measurement. The predicted crack propagation rate in this work are in the range of values from the reference [41, 44-46].

Figure 6 shows examples of voltage profiles for three cases at two specific cycle numbers, N = 372 (Figure 6a) and N = 757 (Figure 6b). Case 1 does not consider crack propagation, i.e., degradation mechanisms 3 and 4 (solid line) are not included. Case 2 does not consider SEI layer growth on previously formed SEI layers, i.e., degradation mechanisms 2 and 4 (dashed line) are not included. Case 3 considers all four degradation mechanisms (dotted line). As shown in Figure 6, capacity reduction and power loss are slightly less for Case 2 as compared to Case 1. However, in the absence of crack propagation (Case 1), there are significant differences in capacity fade and power loss as compared to Case 3. Details of capacity fade and power loss differences are discussed below.

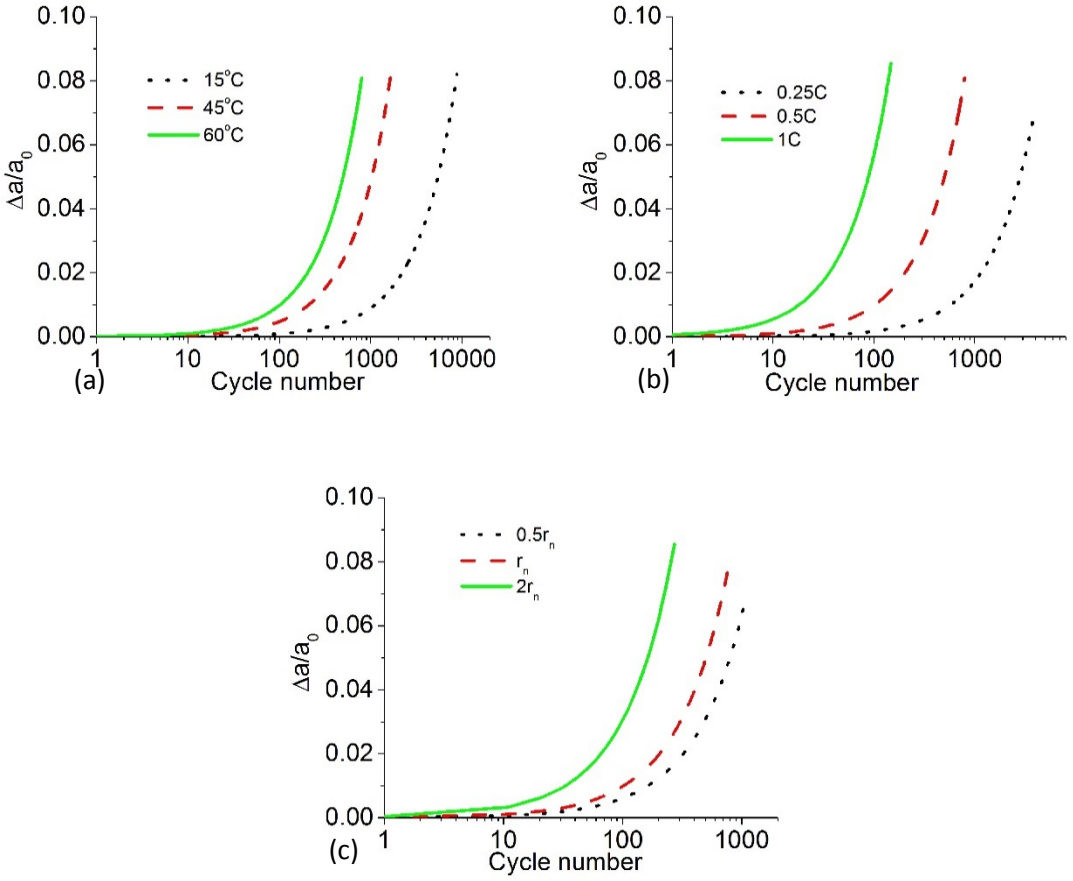

Figure 5. Crack propagation $\Delta a/a_0$ versus cycle number (a) different temperatures with 0.5C and r_n, (b) different C-rates with 60°C and r_n, and (c) different particle sizes with 0.5C and 60°C.

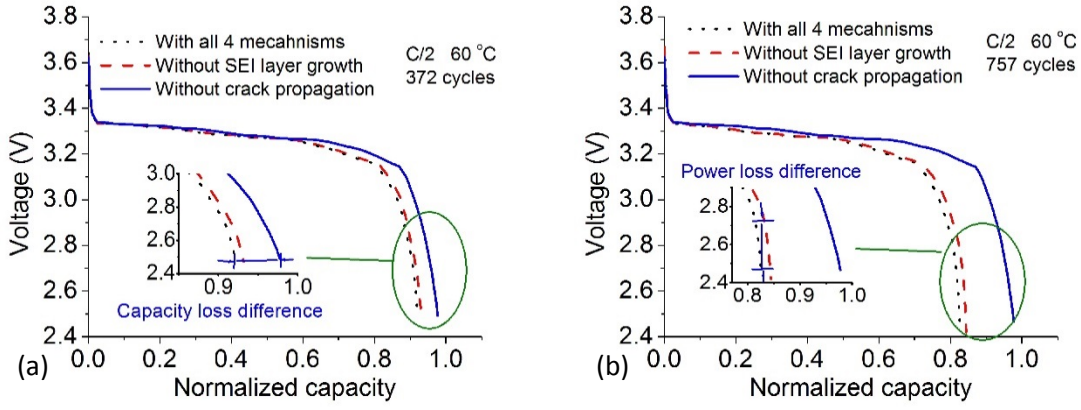

Figure 6. Voltage profiles and resulting capacity fade and power loss when considering a variety of degradation mechanisms at (a) 372 and (b) 757 cycles.

3.2.1. Capacity Loss Analysis. Capacity Fade Deviation (CFD) percentage is defined as

$$CFD = \frac{Q_{case,3} - Q_{case,i}}{Q_{case,3}} \times 100 \quad (26)$$

where $Q_{case,3}$ is the calculated capacity fade for Case 3 and $Q_{case,i}$ is the calculated capacity fade for Case 1 or Case 2.

Therefore, the greater the CFD, the greater the influence of crack propagation (Case 1) or SEI layer growth (Case 2) on battery capacity fade. Compared to the results that take all degradation mechanisms into account, the results for Case 2 show little change in the capacity fade, the CFD values are 0.9% and 1.8% at 372 and 757 cycles, respectively. In contrast, there is a relatively large difference in the capacity fade, i.e., the CFD values are 6.2% and 18.3% at 372 and 757 cycles, respectively, for Case 1. This result indicates that crack propagation accelerates SEI layer formation and, thus, capacity fade, significantly.

Issues such as crack propagation, SEI layer growth, capacity fade, and power loss can be affected by other factors, such as C-rate, temperature, and particle size. Additional studies were conducted to explore these effects and the results are shown in Figure 7, which includes the impact of temperature (Figures 7a and 7b), C-rate (Figures 7c and 7d), and particle size (Figures 7e and 7f). The results in Figures 7a, 7c, and 7e exclude the effect of crack propagation and the results in Figures 7b, 7d, and 7f exclude the effect of SEI layer growth. All of the simulations are terminated assuming battery life is over when the battery capacity reaches 80% of the initial capacity.

Temperature is an important factor determining battery life, as it directly affects the SEI layer formation rate (Equation 8) and the crack propagation rate (Equation 10). As shown in Figures 7a and 7b, for the original particle size (5 μm) at 0.5C, higher temperatures increase the crack growth rate and SEI layer growth rate, resulting in more SEI layer formation on the cracked surfaces. Case 1 shows the CFD values are 23.29% and 22.95% at 15 and 60 ^{o}C, respectively (Figure 7a); however, the results of Case 2 show that the CFD values are 1.01% and 1.99% at 15 and 60 ^{o}C, respectively (Figure 7b).

The C-rate impacts capacity fade because it affects not only the battery electrochemical reaction (Equation 1) but also the maximum stress on the particle surface (Equation 14). As shown in Figures 7c and 7d, a higher C-rate results in shorter battery life. For instance, the cycle life is 4,000 cycles at 0.25C while the life is only 150 cycles at 1C. This is due to the fact that higher C-rates promote crack propagation by increasing the maximum stress at the particle surface. In Case 1, 1C results in a CFD value of 23.99%, which is 4.19% greater than the case for 0.25C. Additionally, the results from Case 2 for all of the C-rates show smaller values of CFD than the corresponding results for Case 1.

Particle size will also impact capacity fade because it affects the maximum stress at the particle surface (Equation 14) and the total surface area (Equation 7). Larger particles undergo greater volume change, causing higher stresses. As a result, the CFD value is much greater for Case 1, as compared to the CFD values for Case 2 at all C-rates. As shown in Figures 7e and 7f, the deviation of larger particles ($2r_n$, 23.98% CFD) used in Case 1 is 4.18% greater for the smaller particle ($0.5r_n$, 19.80% CFD); however, the larger particles ($2r_n$, 0.38% CFD) used in Case 2 have a value of CFD that is 4.33%

smaller than the CFD value for the smaller particle ($0.5r_n$, 4.77% CFD), which could be explained by higher current density on the smaller particles.

3.2.2. Power Loss Analysis. Power is another important measure of battery performance.

Similar to capacity fade deviation, a Power Loss Deviation (PLD) percentage is defined as

$$PLD = \frac{I_{app}V_{case,i} - I_{app}V_{case,3}}{I_{app}V_{case,3}} \times 100 = \frac{V_{case,i} - V_{case,3}}{V_{case,3}} \times 100 \quad (27)$$

where $V_{case,3}$ is the calculated voltage for Case 3 and $V_{case,i}$ is the calculated voltage for Cases 1 or 2.

The PLD values were calculated based on the voltage profiles changes (Figure 6) at different operating conditions and the results are given in Figure 8 for a variety of temperatures, C-rates, and particle sizes.

As can be seen in Figure 8, the PLDs indicate that the voltages for Cases 1 and 2 are always greater than the voltage for Case 3. In addition, the PLD value is always significantly larger for higher normalized capacities.

This means that the voltage profile changes significantly due to the capacity fade at the end of discharge, which is related to a high concentration polarization resulting from the shift of the OCP window as mentioned above.

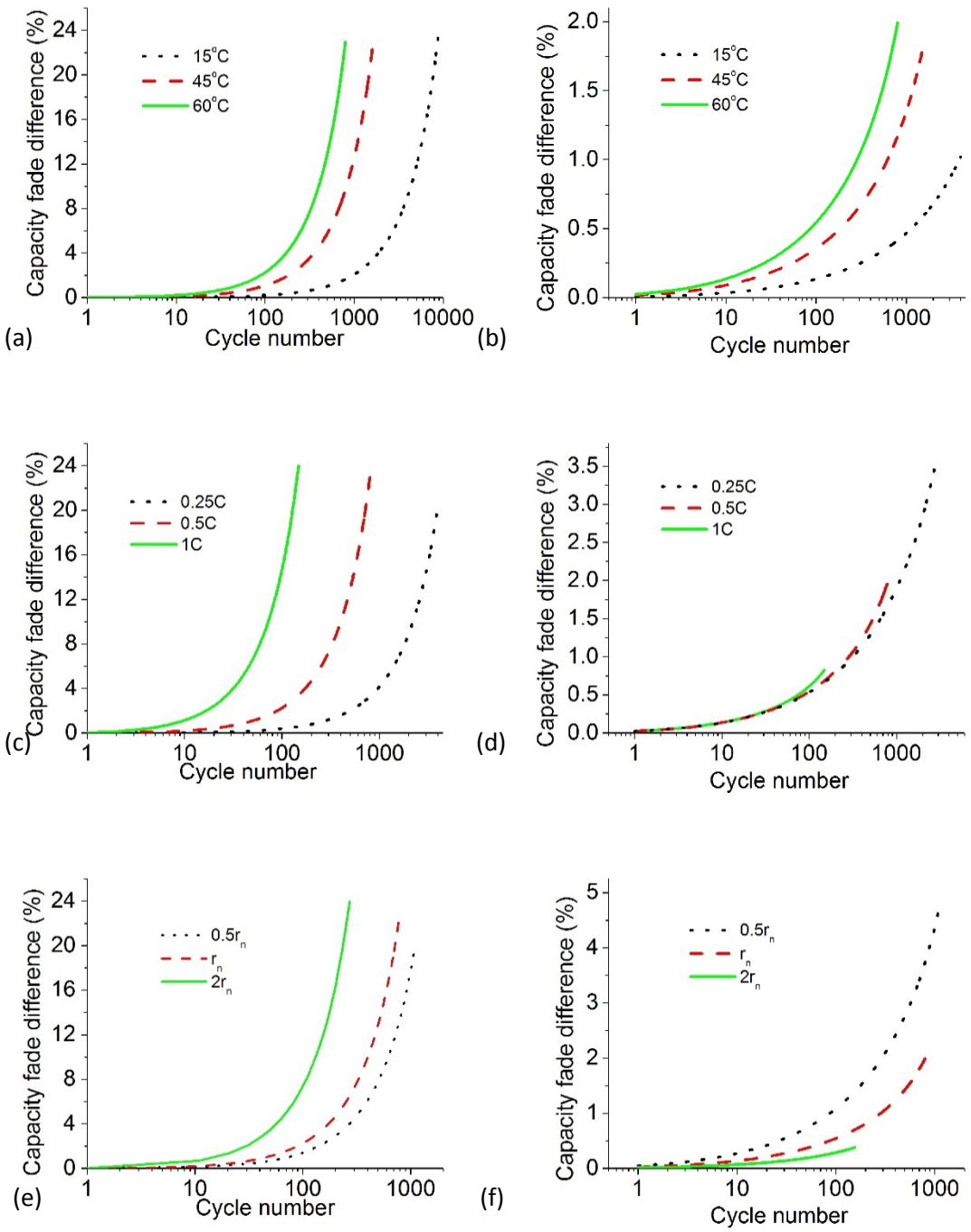

Figure 7. Capacity fade difference between Cases 1 and 3 at (a) different temperatures with 0.5C and r_n, (c) different C-rates with 60 ºC and r_n, and (e) different particle sizes with 0.5C and 60 ºC. Capacity fade difference between Cases 2 and 3 at (b) different temperatures with 0.5C and r_n, (d) different C-rates with 60 ºC and r_n, and (f) different particle sizes with 0.5C and 60 ºC.

The effects of temperature on the voltage loss were similar to the effects of temperature on the capacity fade. Similar to the CFD results for Case 2 where low C-rates caused increased capacity fade due to prolonged battery cycling life, low C-rates will also cause increased battery power loss. In addition, the PLD values for Case 1 (Figure 8c) have 28.18% and 29.53% differences at the end of discharge for 0.25 and 0.5C, respectively, similar to the trend of CFD with C-rates. The PLD value for Case 1 at 1C (13.86%), however, is much smaller than the CFD value for Case 1 (23.99%), which could be due to the fact that the total number of lithium ion loss is not sufficient to affect the voltage profile as calculated by Equations 4 and 5. For particle sizes of $0.5r_n$, r_n, and $2r_n$, the results also generally follow the CFD trends for both Cases 1 and 2.

In summary, the maximum CFD and PLD values at different conditions in Table 3 demonstrate that the effect of SEI layer growth on capacity fade strongly depends on temperature (Figures 7a and 7b), C-rate (Figures 7c and 7d), and particles size (Figures 7e and 7f). Also, the effect of SEI layer growth on power loss strongly depends on C-rate (Figures 8c and 8d) and particle size (Figures 8e and 8f), but it is less sensitive to temperature (Figures 8a and 8b). The effect of crack propagation on capacity fade decreases as the C-rate and particle size decrease. It also can be concluded that the effect of crack propagation is more important than the effect of SEI layer growth on capacity fade and power loss for all of the operating conditions considered here.

3.2.3. SEI Layer Resistance. The SEI layer can interfere with ion transport and may result in increased internal battery resistance. In this study, the SEI layer resistance is integrated with the SP model via Equations 22-25 to study the effect of SEI layer resistance on the voltage curve profile and capacity fade. Figure 9 shows the voltage

profiles for two different C-rates with and without considering SEI layer resistance, R_{SEI}, in Equation 25. At 0.5C, the effect of SEI layer resistance on voltage drop at the start of discharge is very small (0.1%) and has no effect on the final capacity, which is consistent with experimental observations at 0.5C [40]. However, as shown in Figure 9b, the initial voltage drop increases by 2% (0.03 V) and shows a 0.3% capacity fade at 3C when the capacity decayed to 80%. Therefore, it can be concluded that SEI layer resistance has a greater impact on the voltage profile as the C-rate increases.

Table 3. Maximum CFD and PLD values for different conditions.

Parameters	Capacity Fade Deviation		Power Loss Deviation	
	No crack propagation	No SEI layer growth	No crack propagation	No SEI layer growth
15 ^{o}C, 0.5C, r_n	23.29%	1.01%	27.42%	11.36%
45 ^{o}C, 0.5C, r_n	23.06%	1.78%	27.64%	12.12%
60 ^{o}C, 0.5C, r_n	22.95%	1.99%	29.53%	15.25%
60 ^{o}C, 0.25C, r_n	20.32%	3.53%	28.18%	18.42%
60 ^{o}C, 1C, r_n	23.99%	0.82%	13.86%	1.77%
60 ^{o}C, 0.5C, 0.5r_n	19.80%	4.77%	25.90%	19.52%
60 ^{o}C, 0.5C, 2r_n	23.98%	0.38%	29.29%	7.86%

4. SUMMARY AND CONCLUSIONS

In this paper, an advanced capacity fade model, coupled with chemical and mechanical degradation mechanisms, was developed based on an SP model. This SP model includes electrolyte physics, alleviating the problem of low accuracy at high C-rates. The proposed model was able to accurately predict battery capacity fade and voltage profile as a function of cycle number over a broad temperature range with an error of 10.3×10^{-3} RMSE compared to experimental results. The key findings can be summarized as follows:

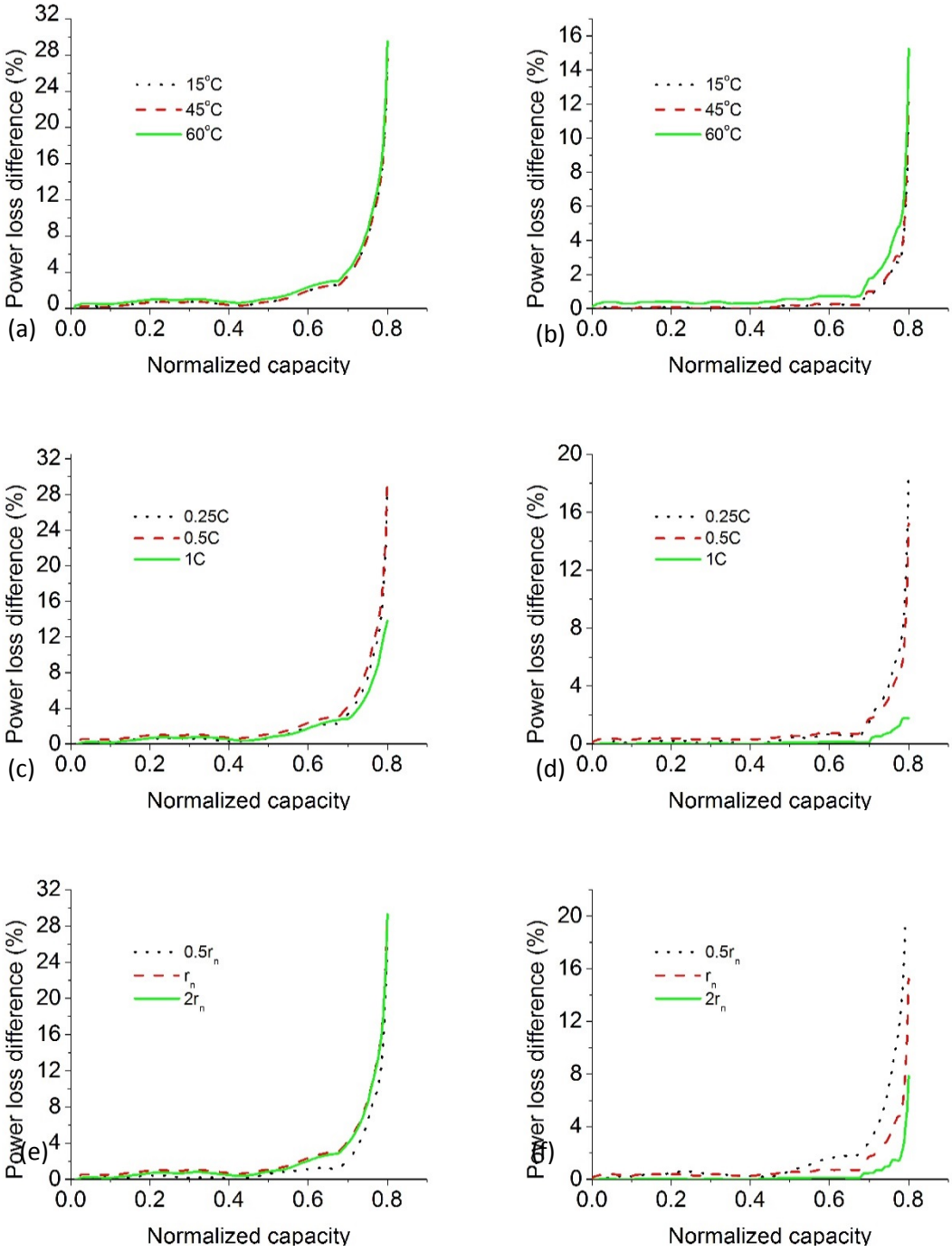

Figure 8. Power loss differences between Cases 1 and 3 at (a) different temperatures with 0.5C and r_n, (c) different C-rates with 60 °C and r_n, and (e) different particle sizes with 0.5C and 60 °C. Power loss differences between Cases 2 and 3 at (b) different temperatures with 0.5C and r_n, (d) different C-rates with 60 °C and r_n, and (f) different particle sizes with 0.5C and 60 °C.

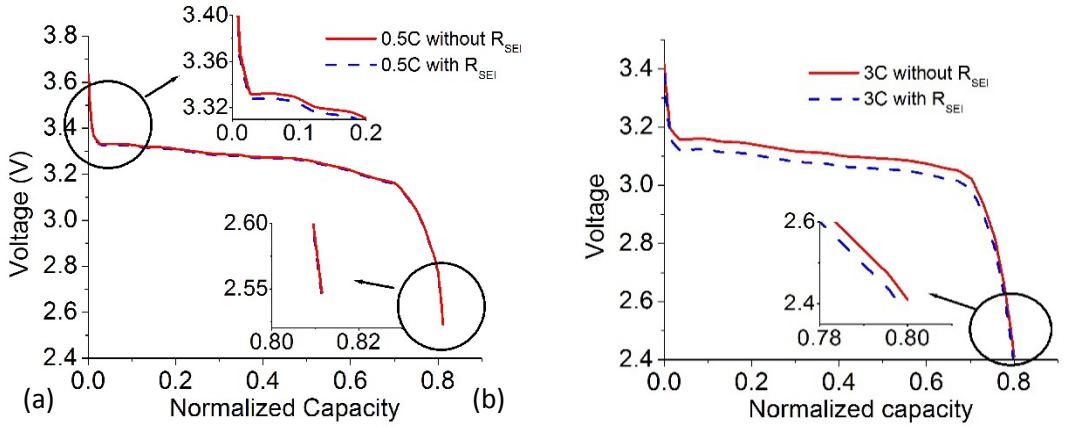

Figure 9. Voltage profiles with and without consideration of SEI layer resistance at 60 ^{o}C for (a) 0.5C and (b) 3C after 757 cycles.

(1) The SEI layer formation on newly formed surfaces due to the crack propagation dominates the capacity degradation during cycling; it had a 9 times greater effect on capacity fade than the growth of the existing SEI layer on all surfaces (i.e., particle and cracks).

(2) The effect of crack propagation on capacity strongly depends on temperature, C-rate, and particle size, and the effect of crack propagation on power loss increases at higher temperatures, lower C-rates, and smaller particle sizes.

(3) Battery resistance increased slightly (0.1%) with cycling at low C-rate (0.5C) and had minimal impact on battery capacity fade, which agrees well with the experimental observations from the literature. At higher C-rates (3C), the SEI layer resistance had more impact (2% voltage drop) on voltage profiles.

In future studies, this model will be further extended by including additional side reactions such as lithium plating. One key challenge in fast charging is lithium plating and its interaction with other side reactions. This means fast charging needs an adaptive

charging protocol as a function of cycle. This model will be a very important foundation for the creation of a fast charging protocol.

REFERENCES

[1] L. D. Couto, J. Schorsch, M. M. Nicotra, and M. Kinnaert, "SOC and SOH estimation for Li-ion batteries based on an equivalent hydraulic model. Part I: SOC and surface concentration estimation," in *2016 American Control Conference (ACC)*, pp. 4022-4028, 2016.

[2] H. Rahimi-Eichi, U. Ojha, F. Baronti, and M.Y. Chow, "Battery management system: an overview of its application in the smart grid and electric vehicles," *IEEE Industrial Electronics Magazine*, vol. 7, pp. 4-16, 2013.

[3] J. Vetter, P. Novák, M. Wagner, C. Veit, K.C. Möller, J. Besenhard, M. Winter, M. Wohlfahrt-Mehrens, C. Vogler, and A. Hammouche, "Ageing mechanisms in lithium-ion batteries," *Journal of Power Sources*, vol. 147, pp. 269-281, 2005.

[4] V. Agubra and J. Fergus, "Lithium ion battery anode aging mechanisms," *Materials*, vol. 6, pp. 1310-1325, 2013.

[5] P. Arora, R. E. White, and M. Doyle, "Capacity fade mechanisms and side reactions in lithium-ion batteries," *Journal of the Electrochemical Society*, vol. 145, pp. 3647-3667, 1998.

[6] R. Hausbrand, G. Cherkashinin, H. Ehrenberg, M. Gröting, K. Albe, C. Hess, and W. Jaegermann, "Fundamental degradation mechanisms of layered oxide Li-ion battery cathode materials: Methodology, insights and novel approaches," *Materials Science and Engineering*: *B*, vol. 192, pp. 3-25, 2015.

[7] M. B. Pinson and M. Z. Bazant, "Theory of SEI formation in rechargeable batteries: capacity fade, accelerated aging and lifetime prediction," *Journal of the Electrochemical Society*, vol. 160, pp. A243-A250, 2013.

[8] J. Li, A. K. Dozier, Y. Li, F. Yang, and Y. T. Cheng, "Crack pattern formation in thin film lithium-ion battery electrodes," *Journal of the Electrochemical Society*, vol. 158, pp. A689-A694, 2011.

[9] J. Dahn, "Phase diagram of Li_xC_6," *Physical Review B*, vol. 44, p. 9170, 1991.

[10] L. Beaulieu, S. Beattie, T. Hatchard, and J. Dahn, "The electrochemical reaction of lithium with tin studied by in situ AFM," *Journal of the Electrochemical Society*, vol. 150, pp. A419-A424, 2003.

[11] X. Zhang, W. Shyy, and A. M. Sastry, "Numerical simulation of intercalation-induced stress in Li-ion battery electrode particles," *Journal of the Electrochemical Society*, vol. 154, pp. A910-A916, 2007.

[12] K. Zhao, M. Pharr, J. J. Vlassak, and Z. Suo, "Fracture of electrodes in lithium-ion batteries caused by fast charging," *Journal of Applied Physics*, vol. 108, p. 073517, 2010.

[13] X. Lin, J. Park, L. Liu, Y. Lee, A. Sastry, and W. Lu, "A comprehensive capacity fade model and analysis for Li-ion batteries," *Journal of the Electrochemical Society*, vol. 160, pp. A1701-A1710, 2013.

[14] G. Ning, B. Haran, and B. N. Popov, "Capacity fade study of lithium-ion batteries cycled at high discharge rates," *Journal of Power Sources*, vol. 117, pp. 160-169, 2003.

[15] J. Christensen and J. Newman, "A mathematical model for the lithium-ion negative electrode solid electrolyte interphase," *Journal of the Electrochemical Society*, vol. 151, pp. A1977-A1988, 2004.

[16] E. Prada, D. Di Domenico, Y. Creff, J. Bernard, V. Sauvant-Moynot, and F. Huet, "A simplified electrochemical and thermal aging model of LiFePO4-graphite li-ion batteries: power and capacity fade simulations," *Journal of the Electrochemical Society*, vol. 160, pp. A616-A628, 2013.

[17] R. Deshpande, M. Verbrugge, Y. T. Cheng, J. Wang, and P. Liu, "Battery cycle life prediction with coupled chemical degradation and fatigue mechanics," *Journal of the Electrochemical Society*, vol. 159, pp. A1730-A1738, 2012.

[18] C. Delacourt and M. Safari, "Mathematical Modeling of Aging of Li-Ion Batteries," in *Physical Multiscale Modeling and Numerical Simulation of Electrochemical Devices for Energy Conversion and Storage*, ed: Springer, pp. 151-190, 2016.

[19] G. Ning and B. N. Popov, "Cycle life modeling of lithium-ion batteries," *Journal of the Electrochemical Society*, vol. 151, pp. A1584-A1591, 2004.

[20] K. Takahashi, and V.Srinivasan, "Examination of graphite particle cracking as a failure mode in lithium-ion batteries: a model-experimental study, " *Journal of the Electrochemical Society*, *162*(4), pp.A635-A645, 2015.

[21] M.Berecibar, I. Gandiaga, I. Villarreal, N. Omar, J. Van Mierlo, and P. Van den Bossche, "Critical review of state of health estimation methods of Li-ion batteries for real applications." *Renewable and Sustainable Energy Reviews*, *56*, pp.572-587, 2016.

[22] V. R. Subramanian, V. D. Diwakar, and D. Tapriyal, "Efficient macro-micro scale coupled modeling of batteries," *Journal of the Electrochemical Society*, vol. 152, pp. A2002-A2008, 2005.

[23] S. Santhanagopalan and R. E. White, "Online estimation of the state of charge of a lithium ion cell," *Journal of Power Sources*, vol. 161, pp. 1346-1355, 2006.

[24] V. R. Subramanian, V. Boovaragavan, V. Ramadesigan, and M. Arabandi, "Mathematical model reformulation for lithium-ion battery simulations: Galvanostatic boundary conditions," *Journal of the Electrochemical Society*, vol. 156, pp. A260-A271, 2009.

[25] M. Doyle, T. F. Fuller, and J. Newman, "Modeling of galvanostatic charge and discharge of the lithium/polymer/insertion cell," *Journal of the Electrochemical Society*, vol. 140, pp. 1526-1533, 1993.

[26] X. Hu, S. Li, and H. Peng, "A comparative study of equivalent circuit models for Li-ion batteries," *Journal of Power Sources*, vol. 198, pp. 359-367, 2012.

[27] C. Lin, A. Tang, and J. Xing, "Evaluation of electrochemical models based battery state-of-charge estimation approaches for electric vehicles." *Applied Energy*. May 29, 2017.

[28] C. Ozkurt, F. Camci, V. Atamuradov, and C. Odorry, "Integration of sampling based battery state of health estimation method in electric vehicles. " *Applied Energy*, *175*, pp.356-367, 2016.

[29] X. Li, J. Jiang, L.Y. Wang, D. Chen, Y. Zhang, and C. Zhang, "A capacity model based on charging process for state of health estimation of lithium ion batteries. " *Applied Energy*, *177*, pp.537-543, 2016.

[30] N. Lotfi, J. Li, R.G. Landers, and J. Park, “Li-ion battery state of health estimation based on an improved Single Particle model.” In *American Control Conference (ACC)*, pp. 86-91, 2017.

[31] N. Lotfi, R.G. Landers, J. Li, and J. Park, "Reduced-order electrochemical model-based SOC observer with output model uncertainty estimation. " *IEEE Transactions on Control Systems Technology*, *25*(4), pp.1217-1230, 2017.

[32] M. Guo, G. Sikha, and R. E. White, "Single-particle model for a lithium-ion cell: Thermal behavior," *Journal of the Electrochemical Society*, vol. 158, pp. A122-A132, 2011.

[33] J. Li, N. Lotfi, R. Landers, and J. Park, "A single particle model for lithium-Ion batteries with electrolyte and stress-enhanced diffusion Physics," *Journal of the Electrochemical Society*, vol. 164, pp. A874-A883, 2017.

[34] E. Prada, D. Di Domenico, Y. Creff, J. Bernard, V. Sauvant-Moynot, and F. Huet, "Simplified electrochemical and thermal model of LiFePO4-graphite Li-ion batteries for fast charge applications," *Journal of the Electrochemical Society*, vol. 159, pp. A1508-A1519, 2012.

[35] P. Paris and F. Erdogan, "A critical analysis of crack propagation laws," *Journal of Basic Engineering*, vol. 85, pp. 528-533, 1963.

[36] T. L. Anderson and T. Anderson, *Fracture mechanics: fundamentals and applications*: CRC press, 2005.

[37] Y. T. Cheng and M. W. Verbrugge, "Evolution of stress within a spherical insertion electrode particle under potentiostatic and galvanostatic operation," *Journal of Power Sources*, vol. 190, pp. 453-460, 2009.

[38] M. Zhu, J. Park, and A. M. Sastry, "Fracture analysis of the cathode in li-ion batteries: a simulation study," *Journal of the Electrochemical Society*, vol. 159, pp. A492-A498, 2012.

[39] J. Park, W. Lu, and A.M. Sastry, "Numerical simulation of stress evolution in lithium manganese dioxide particles due to coupled phase transition and intercalation. " *Journal of The Electrochemical Society*, *158*(2), pp.A201-A206, 2011.

[40] L. Lu, X. Han, J. Li, J. Hua, and M. Ouyang, "A review on the key issues for lithium-ion battery management in electric vehicles," *Journal of Power Sources*, vol. 226, pp. 272-288, 2013.

[41] P. Liu, J. Wang, J. Hicks-Garner, E. Sherman, S. Soukiazian, M. Verbrugge, H. Tataria, J. Musser, and P. Finamore, "Aging mechanisms of LiFePO4 batteries deduced by electrochemical and structural analyses," *Journal of the Electrochemical Society*, vol. 157, pp. A499-A507, 2010.

[42] W. John, P. Liu, J. Hicks-Garner, E. Sherman, S. Soukiazian, M. Verbrugge, H. Tataria, J. Musser, and P. Finamore, "Cycle-life model for graphite-LiFePO 4 cells." *Journal of Power Sources* 196, no. 8: 3942-3948, 2011.

[43] P. Keil, and A. Jossen, "Impact of Dynamic Driving Loads and Regenerative Braking on the Aging of Lithium-Ion Batteries in Electric Vehicles." *Journal of The Electrochemical Society* 164.13 : A3081-A3092, 2017.

[44] J. Hun, M. Chung, M. Park, S. Woo, X. Zhang, and A. Marie, "Generation of realistic particle structures and simulations of internal stress: A numerical/AFM study of LiMn2O4 particles." *Journal of The Electrochemical Society*, *158*(4), pp.A434-A442, 2011.

[45] V.A. Sethuraman, N. Van Winkle, D.P. Abraham, A.F. Bower, and P.R. Guduru, "Real-time stress measurements in lithium-ion battery negative-electrodes." *Journal of Power Sources*, *206*, pp.334-342, 2012.

[46] M.R. Lim, W.I. Cho, and K.B. Kim, "Preparation and characterization of gold-codeposited $LiMn_2O_4$ electrodes." *Journal of power sources*, *92*(1), pp.168-176, 2001.

[47] J. Park, S. Kalnaus, S. Han, Y.K. Lee, G.B. Less, N.J. Dudney, C. Daniel, and A.M. Sastry, "In situ atomic force microscopy studies on lithium (de) intercalation-induced morphology changes in Li x CoO 2 micro-machined thin film electrodes. " *Journal of Power Sources*, *222*, pp.417-425, 2013.

VI . A SINGLE PARTICLE-BASED BATTERY DEGRADATION MODEL AND LIFE ESTIMATION FOR $LiMn_2O_4$/GRAPHITE BATTERY

ABSTRACT

State of Health (SOH) estimation of Li-ion batteries is a critical function in Battery Management Systems (BMSs). Many estimation techniques utilize a battery model, which require high accuracy and high computational efficiency. Conventional electrochemical full-order models can accurately capture battery states, but they are too complex and computationally expensive to be used in the BMS. A Single Particle (SP) model is a good alternative to addresses this issue. In this work, an SP model for $LiMn_2O_4$/Graphite batteries is developed by including the key degradation mechanisms of (1) Mn dissolution in the cathode and (2) Li-ion loss due to SEI layer formation in the anode coupled with mechanical degradation mechanism. The model proposed in this paper provides quantitative information regarding, Mn dissolution and Li-ion loss as well as the resulting battery capacity fade. Two stages of capacity fade are observed: The Li-ion loss due to SEI layer formation dominated the cell capacity loss, and then the Mn dissolution dominated the cell degradation due to the volume fraction changes. This model, quickly and accurately predicts capacity/voltage, can be used for SOH estimation.

1. INTRODUCTION

Li-ion battery is one of the most important components of for portable devices, electric vehicles (EV), and many applications. The most important concerning of the

usage of Li-ion battery is the degradation. Due to irreversible physical and chemical changes, battery performance decreases over time until the battery can no longer be used. For example, when the battery capacity of an electric vehicle reaches 80% of its initial capacity, the battery is no longer considered to be available.[1] The Battery State of Health (SOH) have been used to indicate the state of a battery's condition compared to its initial condition, which is represented by the capacity of the battery after certain charge-discharge cycles. Therefore, SOH estimation is an essential component to control Li-ion battery usage.[1, 2] In order to estimate the SOH, the degradation mechanisms, depended on the chemical nature of the materials for a variety of anode and cathode materials, have to be considered. Battery degradation mechanisms [3-6] can be generally included as current collector corrosion, morphological changes or dissolution of active materials, electrolyte decomposition, and Solid Electrolyte Interphase (SEI) layer formation. The most known processes leading to capacity fade in Li-ion batteries are SEI layer formation and growth on the anode particles and manganese (Mn) dissolution of the cathode materials.

On the anode active material particle surface, the SEI layer will form on the first few cycles with a significant amount of irreversible capacity loss and will grow during charge-discharge cycling, which results in further irreversible ion loss [3-5, 7]. Moreover, mechanical damage due to the stress generated on particle surface will accelerate chemical degradation [8]. During the intercalation/de-intercalation process, volume change causes considerable stresses inside the particles, leading to mechanical failures such as pulverization of, or cracks and fractures in, the active materials. These cracks growth will generate new surfaces on the particle and the new surface is exposed

to the electrolyte [8-14], which leading to additional SEI layer formations and then the acceleration of capacity. The amount of Li-ions loss depending on the type of carbon used as the anode. For the graphitic material (MCMB), the irreversible capacity is about 8 to 15%, and for hard carbons, it can archive 50% of reversible capacity [5]. For the cathode side, Lithium Manganese Oxide (LMO) spinel is a commonly used active material due to its economic and non-toxic features. However, the capacity loss of LMO during cycling is a critical issue in most applications. Among the several degradation mechanisms, such as surface film formation and electrolyte decomposition, Mn dissolution is the primary reason for capacity fade in the LMO cathode [15].

The foundation of many battery degradation prediction models developed in current decades is physics-based models that provide very detailed information regarding the battery electrochemical responses [16-23]. SEI layer formation was simulated through a full order model by considering the flux of the side reaction at the anode particle surface [16, 17] or by modifying the solid phase concentration to be a function of the cycle according to Li-ion loss [18-20]. The effect of mechanical degradation on capacity fade was also simulated using a full order electrochemical model [21]. The dissolution of Mn has been studied with the full order model for LMO cathode degradation [22] and also the dissolution was coupled with side-reactions from anode [23] to predict the battery capacity fade. Even though the full order model is ideal for the detailed analysis of battery performance and able to accurately capture the degradation of LMO/graphite phenomena, it is too computationally intensive to be efficiently utilized in a BMS [24, 25]. These degradation model, based on the full order electrochemical model, solve ten more coupled partial differential equation for the mass conservation and charge

conservation in the solid and electrolyte phases, as well as kinetic reactions at the interface between the solid and electrolyte. This has led to a requirement to reduce the complexity of electrochemical models. For instance, the studies in [26, 27] reduced the electrochemical model proposed by Doyle et al. [28] into a form suitable for a BMS; however, the model parameter identification process required to construct these models is unwieldy. To simply the model identification process, an Equivalent Circuit Model (ECM) have been used for BMS, which describes the battery dynamic behavior as a voltage source and a series of resistors and capacitors [29]. The disadvantage of ECM models are low fidelity, limited prediction capability, and their states have no physical significance, which leads to limitations of the usage for different applications. A physical-based reduced-order model, called Single Particle (SP) model, shows the balance between full order electrochemical models and ECMs. The SP model assumes multiple uniform sized spherical particles in both electrodes, and then the current distribution is uniform across both electrodes. Therefore, each electrode can be approximated by a single spherical particle. The SP model includes a set of ordinary differential equations which are directly derived from comprehensive electrochemical models. Thus, the SP model is able to explicitly and physically represent many battery properties.

In this paper, we present a side-reaction coupled SP model for capacity degradation analysis of Li-ion batteries. This side-reaction coupled model includes the SEI layer formation on the anode side for graphite material, and the Mn dissolution on the cathode side for LMO material. The cell internal resistance increase due to SEI layer formation and diffusion change due to dissolution is also included. The effects of

different degradation mechanisms on capacity fade and battery performance area studied quantitatively. As a result, three stages are found for the degradation of LMO/graphite battery: (1) SEI layer formation dominant cycles, (2) SEI layer stabilizing cycles, and (3) dissolution dominant cycles.

2. EXPERIMENTAL METHOD

In this work, a $LiMn_2O_4$ (LMO) paste were prepared by first mixing 85.5 wt% LMO powder (MTI, 13 μm) with 6.5 wt% carbon black (CB, Alfa Aesar) and 8 wt% Polyvinylidene fluoride (PvdF, Sigma-Aldrich), and that was then dispersed in N-Methyl-2-pyrrolidone solvent (NMP, Sigma-Aldrich), similarly MCMB paste was prepared by mixing MCMB powder) with 6.5 wt% CB and 8 wt% PvdF in NMP. The pastes were mixed by a SpeedMixer (FlackTeck Inc) at 2000 RMP for 20 minutes at room temperature. A CR2032 coin cell (Wellcos Corp) was used to assemble the battery in an argon-filled glove box (Mbraun). LMO was used as a cathode, MCMB as an anode, and commercial PP/PE/PP membrane (Celgard) as a separator; the battery was filled with liquid electrolyte 1M $LiFP_6$ EC:DMC 1:1 (Sigma-Aldrich). The electrochemical behavior of the assembled batteries was measured from 3 V to 4.2 V by using a battery testing station (IVIUMnSTAT, Ivium Tech). The cycling performances were conducted under 0.1 C-rate at room temperature.

3. COMPUTATIONAL METHODOLOGY AND IMPLEMENTATION

Figure 1a is the schematic diagram of a Li-ion cell composed of two electrodes (a solid matrix in an electrolyte solution) and a separator (electrolyte solution), while Figure 1b shows the concept of the SP model, which represents each electrode as a single particle. Pesudo-2D (P2D) models, which are based on porous electrode theory using concentrated solutions, are widely used for battery modeling [14]. This model describes Li-ion transport through the use of one-dimensional (battery thickness, *x*, direction) charge and mass conservation laws along with the thickness direction, as well as the diffusion process for individual active particles, which is implemented in the radial direction of the particles,. The kinetic reaction at the particle surfaces is described by the Butler-Volmer equation. The P2D model consists of ten coupled nonlinear partial differential equations for the mass and charge balance in the solid and electrolyte phases [16].

In the SP model it is assumed that the current passing through the electrode is uniformly distributed over all of the particles inside the electrode. Therefore, as shown in Figure 1b, each electrode can be modeled as a single spherical particle [17], and the governing partial differential equations can be simplified into a set of algebraic equations. Further, the complex multi-physics of the battery can be implemented in a relatively simple manner based on the assumption of uniformity of intercalation flux in the SP model [30], which leads to each reaction inside electrode, such as diffusion, transportation, diffusion-induced stress, and side-reactions, has a uniform impact on each

particle. In addition, the SP models can be extend to include the concentration and potential distribution in electrolyte phase to improve model accuracy at high C-rates. [30]

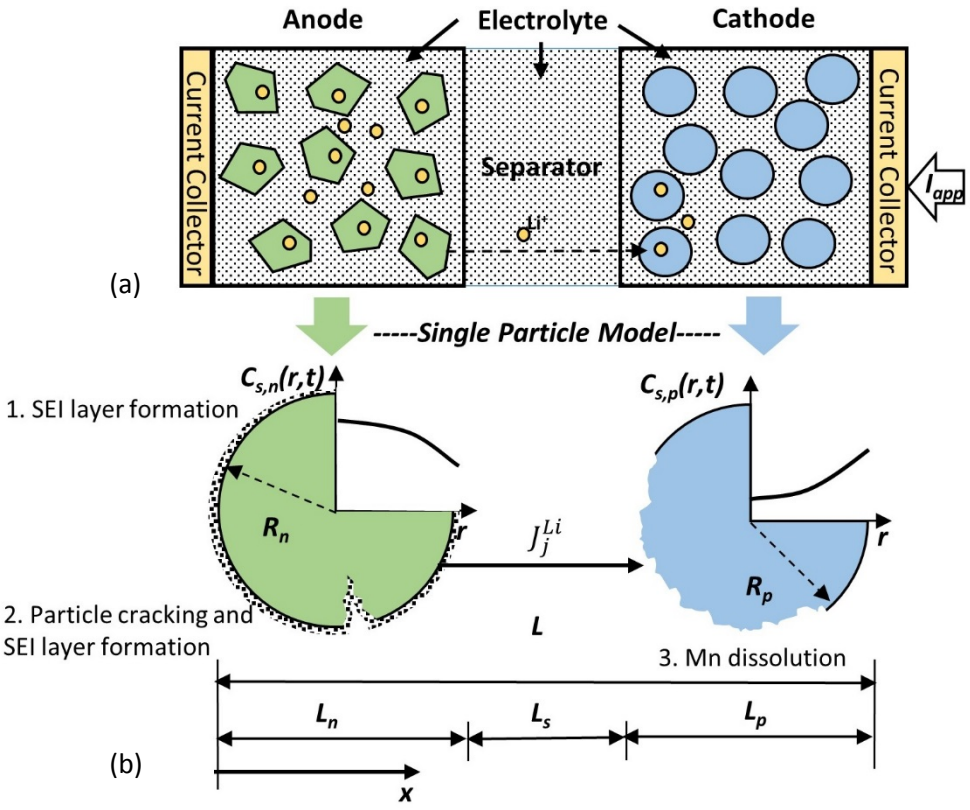

Figure 1. Schematic of anode, separator, and cathode in a Li-ion battery for P2D and SP models, and schematic of SEI layer formation, crack propagation, and dissolution on a particle surface.

The remaining challenge of SP model is to consider battery degradation. On the anode side, the degradation is due to the coupled mechanisms between mechanical crack propagation and SEI layer formation and growth. In the SEI layer formation and growth model, the crack propagation is used to estimate the new SEI layer formation on the surface of newly-formed cracks. One the cathode side, the Mn dissolution leads to the

reduction of solid phase volume fraction of the active material, which impact the kinetic reaction and diffusivity of the active material.

In the SP mode, to calculate the terminal voltage, the SP model considers the solid phase potential difference between the end sides of both electrodes based on Bulter-Volmer equation [30]

$$\begin{aligned} V_t(t) &= \Phi_{1,p}(t)\big|_{x=L} - \Phi_{1,n}(t)\big|_{x=0} \\ &= \left(\eta_p + \Phi_{2,p}(t)\big|_{x=L} + U_p\left[\frac{c_{s,p,surf}(t)}{c_{s,p,max}}\right]\right) \\ &\quad - \left(\eta_n + \Phi_{2,n}(t)\big|_{x=0} + U_n\left[\frac{c_{s,n,surf}(t)}{c_{s,n,max}}\right]\right) \end{aligned} \tag{1a}$$

$$\eta_j(t) = \frac{2RT}{F}\ln\left[m_j(t) + \sqrt{m_j^2(t)+1}\right] \tag{1b}$$

where $m_j(t) = \dfrac{J_j^{Li}}{2k_j c_{s,j,max} c_e^{0.5}\left[1-\frac{c_{s,j,surf}(t)}{c_{s,j,max}}\right]^{0.5}\left(\frac{c_{s,j,surf}(t)}{c_{s,j,max}}\right)^{0.5}}$.

The electrolyte potential difference is considered as:

$$\begin{aligned} &\Phi_{2,p}(t)\big|_{x=L} - \Phi_{2,n}(t)\big|_{x=0} \\ &\quad = (1-t_+)\frac{2RT}{F}\ln\frac{c_{e,p}(L,t)}{c_{e,n}(0,t)} - \frac{I_{app}}{2}\left(\frac{L_n}{k_n^{eff}} + \frac{2L_s}{k_s^{eff}} + \frac{L_p}{k_p^{eff}}\right) \end{aligned} \tag{1c}$$

where $c_{s,j,max}$ is the maximum solid phase concentration, k_j is the reaction rate constant and $j = p/n$ denotes the positive/negative electrode, respectively. R is the universal gas constant, T is temperature, and F is Faraday's constant, $\Phi_{1,j}$ is the solid-phase potential and U_j is the Open-Circuit Potential (OCP). The OCP, in general, is a function of the

normalized surface concentration, $c_{s,j,surf}(t)/c_{s,j,max}$. $k_i^{eff} = k_i \varepsilon_i^{brug}$, *brug* denotes the bruggeman coefficient and k_i is the electrolyte conductivities [18]. L_i is the thickness, i = p/s/n denotes the positive/separator /negative electrode, respectively. I_{app} is the applied current density, t_+ is cationic transport number in the electrolyte, J_j^{Li} is the electrochemical reaction rate and $c_{e,i}(x,t)$ is the electrolyte concentration [18].

3.1. LI-ION LOSS DUE TO SEI LAYER FORMATION

Equation 1 does not include battery capacity reduction effects and, therefore, does not exhibit changes in the voltage profile as the battery is cycled. In order to implement capacity loss mechanisms into the SP model, the initial concentrations, $c_{s,p}(0)\big|_{N+1}$ and $c_{s,n}(0)\big|_{N+1}$ for the cathode and anode, respectively, at the beginning of the $(N+1)^{th}$ cycle must be calculated. Here, a fully charged status of the battery is assumed. Then, the number of available Li-ions inside the battery after the N^{th} cycle can be calculated based on the capacity after the N^{th} cycle, Q_N, and the initial total number of Li-ions inside the battery, n_{Li}. From charge conservation in the anode and cathode at the $(N+1)^{th}$ cycle

$$\varepsilon_{s,p} L_p c_{s,p}(0)\big|_{N+1} + \varepsilon_{s,n} L_n c_{s,n}(0)\big|_{N+1} = \frac{Q_N}{Q_0} n_{Li} \tag{2}$$

where Q_0 is the battery capacity after the formation cycle (described below). In addition, the initial voltage at the N^{th} cycle, $V(0)$, is constant at the beginning of discharge at each cycle, is

$$U_p\left[\frac{c_{s,p}(0)\big|_{N+1}}{c_{s,p,max}}\right] - U_n\left[\frac{c_{s,n}(0)\big|_{N+1}}{c_{s,n,max}}\right] = V(0) \quad (3)$$

Therefore, the initial concentrations in the anode and cathode are estimated by solving Eqs. 2 and 3. It should be noted that as the battery capacity decreases with each cycle, the corresponding OCP curve windows change, affecting the concentration polarization. The reduction in capacity can be attributed to Li-ion loss during the formation and growth of SEI layers on anode active material particle surfaces.

A fresh battery cell undergoes a process called 'formation cycle' to stabilize the cell by forming an initial SEI layer. During the formation cycle, a uniform SEI layer is formed on the freshly exposed particle surfaces due to electrolyte reduction. Once the battery is in use, the SEI layer tends to grow, and stresses developed due to changes in the battery volume cause crack propagation on the particle surface, creating new surfaces that are exposed to the electrolyte and on which new SEI layers will form. We utilized the growth model developed by Rutooj et al. [20] in our work and extended our SP model to include degradation mechanisms due to SEI layer formation and growth [31].

Solid electrolyte interface layer formation and growth can be categorized into four different mechanisms including (1) initial SEI layer formation during the formation cycle; (2) growth on the initially formed SEI layer; (3) initial SEI layer formation on newly formed surfaces due to cracking; and (4) growth of the initially formed SEI layers on the surfaces created by cracking, and the total SEI layer growth rate is [31]

$$\frac{dV_{SEI}}{dN} = \frac{dV_{SEI,2}}{dN} + \frac{dV_{SEI,3}}{dN} + \frac{dV_{SEI,4}}{dN} \quad (4)$$

Then, the capacity fade rate per cycle after the formation cycle is

$$\frac{dQ_N}{dN} = -\frac{n_{SEI}\rho_{SEI}F}{M_{SEI}}\frac{dV_{SEI}}{dN} \tag{5}$$

The SEI layer growth also increase the cell resistance and impact battery power. We estimated battery resistance increase by leveraging the work of Ning et al. [21]. The SEI layer resistance at the Nth cycle is

$$R_{SEI}|_N = \frac{L_{SEI}|_N}{k_{SEI}} \tag{6}$$

where k_{SEI} is the SEI layer conductivity and the SEI layer thickness at the Nth cycle is

$$L_{SEI}|_N = \frac{V_{SEI}|_N}{A_{cr}|_N} \tag{7}$$

The initial SEI layer resistance, R_{SEI}^0, is assumed to be on the same order as the electrolyte resistance. Thus, k_{SEI} is calculated based on the initial SEI layer thickness and resistance

$$k_{SEI} = \frac{L_{SEI}^0}{R_{SEI}^0} \tag{8}$$

Finally, the cell terminal voltage, including the impact of initial concentration change (Eqs. 2 and 3), SEI layer resistance (Eq. 6), and other polarizations effects such as activation and diffusion, is

$$V_t(t)|_{N+1} = U_p\left[\frac{c_{s,p,surf}(t)\big|_{N+1}}{c_{s,p,max}}\right] - U_n\left[\frac{c_{s,n,surf}(t)\big|_{N+1}}{c_{s,n,max}}\right] + \frac{2RT}{F}\left\{\ln\left[m_p(t) + \sqrt{m_p^2(t)+1}\right] - \ln\left[m_n(t) + \sqrt{m_n^2(t)+1}\right]\right\} + (1 - t_+)\frac{2RT}{F}\ln\frac{c_{e,p}(L,t)}{c_{e,n}(0,t)} - \frac{I_{app}}{2}\left(\frac{L_n}{k_n^{eff}} + \frac{2L_s}{k_s^{eff}} + \frac{L_p}{k_p^{eff}}\right) + R_{SEI}|_N I_{app} \quad (9)$$

3.2. CAPACITY LOSS DUE TO ACTIVE MATERIAL LOSS IN CATHODE

For the LMO battery, the Mn dissolution is the critical factor for the capacity degradation, and the loss of active material would increase the resistance and reduce solid phase diffusivity. The generated acid inside the cell is responsible for the Mn dissolution as:

$$Solvent \xrightarrow{Oxidation} Sl_o + H^+ + e^- \quad (10)$$

where Sl_o represents the overall products of the solvent oxidation and includes soluble species and solid species. The rate of the solvent decomposition is charge-transfer-kinetic controlled and can be expressed by a Butler-Volmer expression. The H+ production rate due to the reaction given in Eq. 10 can be written as follows:

$$R_{s,1} = \frac{i_o}{F} exp\left(\frac{0.5F}{RT}\eta_{p,avg}\right) \quad (11)$$

The parameter η_j is the reaction over-potential defined as $\eta_j = \Phi_{1,j} - \Phi_{2,j} - U_j$, where $\Phi_{1,j}$ is the solid-phase potential, $\Phi_{2,j}$ is solution-phase potential, and U_j is the open-circuit

potential. The OCP, in general, is a function of the normalized surface concentration, $c_{s,j,surf}/c_{s,j,max,}$ and temperature. In order to calculate the average overpotential, $\eta_{p,avg}$ at cathode, it is assuming that

$$\eta_{p,avg} = \Phi_{1,p} - \Phi_{2,p} - U_p^{eq} \tag{12}$$

where the U_p^{eq} is the equilibrium potential of the side reaction, and $U_p^{eq} = 4.1$. [23]

To cancel out the term $\Phi_{1,p}$- $\Phi_{2,p}$, which cannot be obtained in SP model, the potential along the electrode is calculated as

$$\eta_p = \Phi_{1,p} - \Phi_{2,p} - U_p \tag{13}$$

Then Eq. 12 subtract Eq. 13, it can obtain the averaged potential at cathode

$$\eta_{p,ave} = avg\left(U_p - U_p^{eq}\right) + \eta_p \tag{14}$$

The reaction over-potential can be obtained by rewriting Bulter-Volmer equation as

$$J_j^{Li} = k_j c_{s,j,max} c_e^{0.5} \left[1 - \frac{c_{s,j,surf}}{c_{s,j,max}}\right]^{0.5} \left[\frac{c_{s,j,surf}}{c_{s,j,max}}\right]^{0.5} \left\{exp\left[\frac{0.5F}{RT}\eta_j\right] - exp\left[\frac{-0.5F}{RT}\eta_j\right]\right\} \tag{15}$$

where i_0 is the exchange current density, k_j is the reaction rate constant, c_e is the electrolyte concentration, R is the universal gas constant, T is the temperature, F is

Faraday's constant, $c_{s,j,surf}$ is the particle surface concentration, and $c_{s,j,max}$ is maximum solid phase concentration.

Then the reaction potential can be obtained from Eq. 1b

$$\eta_p = \frac{2RT}{F} \ln\left[m_p + \sqrt{m_p^2 + 1}\right] \tag{16}$$

where $m_p = \frac{J_j^{Li}}{2k_p c_{s,p,max} c_e^{0.5} \left[1 - \frac{c_{s,p,surf}}{c_{s,p,max}}\right]^{0.5} \left(\frac{c_{s,p,surf}}{c_{s,p,max}}\right)^{0.5}}$

The i_0 in Eq. 11 can be calculated as

$$i_0 = k_p c_{s,p,max} {c_{e,j}}^{0.5} \left[1 - \frac{c_{s,p,surf}}{c_{s,p,max}}\right]^{0.5} \left(\frac{c_{s,p,surf}}{c_{s,p,max}}\right)^{0.5} \tag{17}$$

In order to calculate the dissolution as a function of cycle numbers, the value of $\eta_{p,avg}$ and i_0 are averaged to a constant value during cycling. Based on the Eqs. 14 and 17 for one cycle, the i_0 = 1.92 A/m, and $\eta_{p,avg}$ = 0.0047 V, is used for cycling.

The acid attack on the active material in the cathode, $LiMn_2O_4$, is assumed to occur as follows:

$$4H^+ + 2LiMn_2O_4 = 2Li^+ + Mn^{2+} + \frac{3}{2}Mn_2O_4 + 2H_2O \tag{18}$$

It is supposed that the reaction rate for acid attack on the active material shown in Eq. 18 is dominated by the acid concentration in the solution. Consequently, the reaction rate for the reaction in Eq. 18 is given by:

$$R_{s,2} = k_{dis} c_{H^+} \tag{19}$$

where k_{dis} is the reaction rate constant for the acid attack on the active material.

In addition, the concentration of H^+ also affected by $LiPF_6$ salt decomposition:

$$LiPF_6 \rightarrow LiF + PF_5 \tag{20}$$

$$PF_5 + H_2O \rightarrow POF_3 + 2HF \tag{21}$$

$$R_{s,3} = k_{decom} c_{H_2O}^2 c_{Li^+} \tag{22}$$

c_{H^+} is concentration of H^+, c_{Li^+} is concentration of Li^+, c_{H_2O} is the H_2O concentration, and k_{decom} is the salt decomposition coefficient. Then, it is assumed:

$$\varepsilon_{s,p} \frac{\partial c_{H^+}}{\partial t} = 10R_{s,1} - 4a_{pos}R_{s,2} + 2R_{s,3} \tag{23}$$

$$\varepsilon_{s,p} \frac{\partial c_{H_2O}^2}{\partial t} = 2a_{pos}R_{s,2} - R_{s,3} \tag{24}$$

$$\varepsilon_{s,p} \frac{\partial c_{Li^+}}{\partial t} = \frac{1 - t_+}{F} a_{pos} i_p - R_{s,3} \tag{25}$$

$$i_p = i_0 \left\{ exp\left[\frac{0.5F}{RT}\eta_{p,avg}\right] - exp\left[\frac{-0.5F}{RT}\eta_{p,avg}\right] \right\} \tag{26}$$

where $\varepsilon_{s.pos}$ is the positive electrode porosity and a_{pos} represents the specific surface area.

The governing equation for the volume fraction of the active material in the matrix phase which accounts for the acid induced Mn dissolution (side reaction in Eq.18) is given by:

$$\frac{\partial \varepsilon_{s,p}}{\partial t} = -a_{pos} R_{s,2} V_m \tag{27}$$

where V_m is the molar volume of LMO.

Based on the following equations, the solid phase volume fraction change could be implemented into SP model. The volume fraction will affect the Li-ion molar flux density at the surface as:

$$J_p^{Li} = \frac{I_{app} R_p}{3\varepsilon_{s,p} l_p F} \tag{28}$$

where R_p is the particle radius, and I_{app} is applied current.

The change of flux density would affect the concentration diffusion and the potential difference.

$$\frac{\partial c_{s,p}(r,t)}{\partial t} = \frac{D_s}{r^2} \frac{\partial}{\partial r} \left[r^2 \frac{\partial c_{s,p}(r,t)}{\partial r} \right] \tag{29}$$

where $c_{s,p}$ is the solid-phase li-ion concentration, t is time, r is the radial coordinate, D_s is the solid-phase diffusion coefficient. The boundary conditions for Eq. 29 are:

$$D_s \frac{\partial c_{s,j}(r,t)}{\partial r}\Big|_{r=0} = 0 \ , \ D_s \frac{\partial c_{s,j}(r,t)}{\partial r}\Big|_{r=R_p} = -J_j^{Li} \tag{30}$$

The Li-ion diffusion coefficient in the solid phase changes due to the plugging of pores and the formation of the film on the LMO particles surface in the cathode. The reduction of Li-ion diffusion coefficient is given by an empirical equation. That is, the effective diffusion coefficient in the solid phase is given by:

$$D_s = D_{s,0}\left[1 - \left(\frac{\varepsilon_{1,pos}^0 - \varepsilon_{1,pos}}{\varepsilon_{1,pos}^0}\right)^{n1}\right] \quad (31)$$

where $D_{s,0}$ is the initial solid phase diffusion coefficient, $\varepsilon_{s,p}^0$, is the initial solid volume fraction , *n1*, 0.75, is an empirical factor which represents the effect of the formation of the film on the Li ion diffusion.

4. RESULTS AND DISCUSSIONS

4.1. EXPERIMENTAL OBSERVATION

Two cells were tested under 0.1C, cell 1 is used to find fitting parameters and cell 2 is used to validate the simulation results. As shown in Fig. 2a, for cell 1, the capacity fade 10% after first 10 cycles and the capacity fade ratio is stabilized at 0.3% per cycle, thus the first 10 cycles could be considered as the formation cycles, and then the 11th cycle could be assumed as the 2nd cycle for simulation. The results of cell 2 showing results with 0.22% capacity fading rate, the formation cycle can be considered for the first 15 cycles (Fig. 2b). The capacity fade in cells 1 and 2 is assumed only affect by the Li-ion loss due to SEI layer formation on anode graphite material with crack propagation, and dissolution from cathode LMO active material.

The results at 20th, 40th, and 60th cycle are used to compare the capacity fade and voltage profile. In general, cell 2 has 2% more capacity at the three cycles, which could be caused by the slower capacity fading ratio of cell 2 comparing to cell 1 as shown in Table 2.

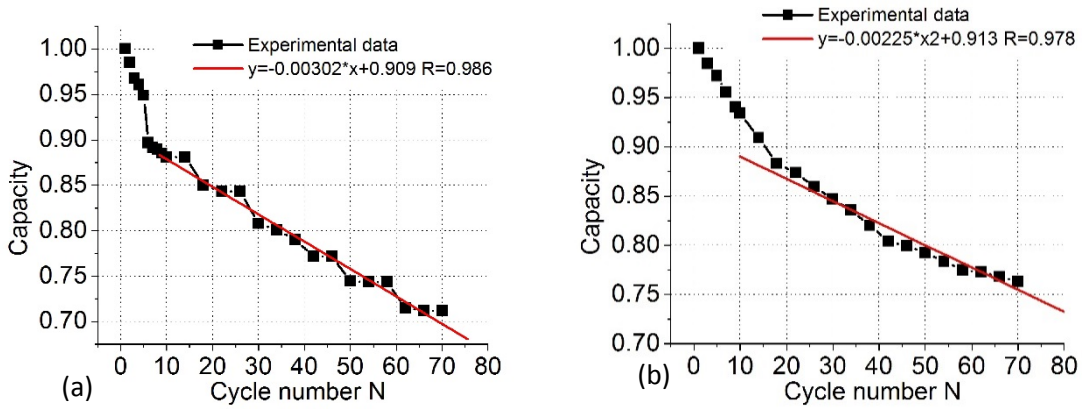

Figure 2. Capacity for different batches (a) cell #1 and (b) cell #2.

Table 1. Capacity fade of cell 1 and cell 2

	Formation cycles	Capacity fade rate pre cycle	Capacity		
			20^{th} cycle	40^{th} cycle	60^{th} cycle
Cell 1	10	0.30%	91.7%	87.6%	80.8%
Cell 2	15	0.22%	93.9%	88.9%	82.4%

4.2. MODEL VALIDATION

The reduction of solid phase volume fraction due to dissolution and the Li-ion loss due to SEI layer formation were calculated based on our SEI layer formation model and dissolution model. The capacity and voltage profiles at 2^{nd} and 60^{th} cycles were first used to modify our SEI layer formation model and dissolution model, and voltage profiles at 20^{th} and 40^{th} cycles were used to validate the simulated results. The capacity loss due to SEI layer and volume fraction at 2^{nd} and 60^{th} cycles were first fitted to match the voltage profile and the remained capacity. The parameters used in the simulation are listed in Table 3.

Table 2. Model parameters used in simulation studies.

Parameter	Value	Description
a_0	2×10^{-9}	Initial crack length (m)
$brug$	1.5	Bruggeman coefficient
c_0	2000	Initial electrolyte concentration (mol m^{-3})
$C_{\max,\, pos}$	22860	Positive maximum concentration (mol m^{-3})
$C_{\max,\, neg}$	15000	Negative maximum concentration (mol m^{-3})
D_e	7.5×10^{-11}	Diffusion coefficient in electrolyte (m^2s^{-1})
$D_{s,n}$	3.9×10^{-14}	Solid-phase Li diffusivity, negative electrode (m^2s^{-1})
$D_{s,p}$	1×10^{-13}	Solid-phase Li diffusivity, positive electrode (m^2s^{-1})
E_{a1}	10.1	Activation energy for crack propagation (kcal mol^{-1}) Fitted
E_{a2}	5.791	Activation energy for SEI layer growth (kcal mol^{-1}) Fitted
E	3.3×10^{10}	Young's modulus of electrode material (N m^{-2})
F	96487	Faraday's constant (C mol^{-1})
k_0	$2.43\text{x}10^{-13}$	Crack propagation coefficient Fitted
k_{dis}	$4.58\text{x}10^{-12}$	Reaction rate constant for the acid attack on the active material (m s^{-1}) Fitted
k_{decom}	$7.5\text{x}10^{-14}$	Salt decomposition coefficient (m^6 mol^{-2}) Fitted
K_{SEI0}	$1.44\text{x}10^{-8}$	SEI layer growth coefficient Fitted
l_{cr0}	2×10^{-9}	Initial crack width (m)
L_n	150×10^{-6}	Negative electrode thickness (m)
L_p	90×10^{-6}	Positive electrode thickness (m)
L_s	30×10^{-6}	Separator thickness (m)
M_{SEI}	78.89	Molecular weight of compounds constituting SEI (g mol^{-1})
n_{SEI}	2	Consumed Li-ion for 1 mol SEI layer formation
Q_g	0.339	Graphite specific capacity (Ah g^{-1})
R	8.314	Universal gas constant (J mol^{-1} K^{-1})
R_n	13×10^{-6}	Particle radius, negative electrode (m)
R_p	15×10^{-8}	Particle radius, positive electrode (m)
R_{SEI}^0	$1\text{x}10^{-3}$	Initial SEI layer resistance (Ω) Assumed
t_+	0.363	Cationic transport number
$V(0)\|_N$	4.2	Initial voltage at each cycle (V)
ε_n	0.471	Negative electrode porosity
ε_p	0.297	Positive electrode porosity
ε_s	1	Separator porosity
ρ_{cr}	2.542×10^{18}	Number of cracks per unit area of particle (m^{-2})
ρ_g	2.26	Graphite density (g cm^{-3})
ρ_{SEI}	2.11×10^{6}	Density of SEI films (g m^{-3})
Ω	8.9×10^{-6}	Partial molar volume of solute (m^3mol^{-1})

4.3. LI-ION LOSS DUE TO SEI LAYER FORMATION

In order to calculate the capacity fade due to SEI layer formation, estimated capacity fade (0% and 13%) at 2nd and 60th cycles were used to find the fitting parameter k_{th0} (coefficient for SEI layer growth) in the SEI layer formation model. Then, the capacity fade is calculated for 20th and 40th cycles (Table 3), and the results with the capacity fade due to SEI layer without dissolution is plotted as Fig. 4. Based on the Li-ion loss due to SEI layer formation, the initial solid phase concentration for both of anode and cathode were updated based on Eqs. 2 and 3, and the resistance due to SEI layer was calculated based on Eq. 6. As shown in Fig. 3, the simulated results at 60th cycle cannot match with experiments observation when only considering the impact of SEI layer on capacity fade, it because that the capacity fade due to SEI layer formation and growth is approximately 0.3% per cycle at 2nd to 40th cycle and then from 40th to 60th cycle the Li-ion loss is slowed down to approximately 0.1% per cycle. This stabilization of capacity fade due to SEI layer is due to the SEI layer became thick and the growth will be slower [17]. Therefore, the remained capacity loss could result from the Mn dissolution at the cathode.

Table 3. Only considered capacity fade due to SEI layer formation

Cycle number	Experimental capacity fade (%)	Capacity fade due to SEI layer (%)	Initial anode concentration ($mol.m^{-3}$)	Initial cathode concentration ($mol.m^{-3}$)	R_{SEI} ($ohm.m^2$)	Simulated capacity fade (%)
2nd	0	0	6603.0	3898.5	1e-3	0
20th	8.3	7	6038.0	3897.4	1.029e-3	8.5
40th	12.6	11	5715.1	3896.8	1.044e-3	13.26
60th	19.2	13	5553.6	3896.5	1.055e-3	15.65

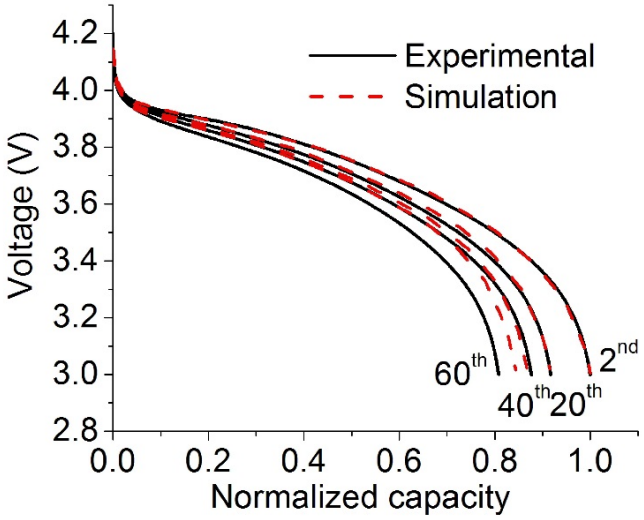

Figure 3. Voltage profile with only considering capacity fade due to SEI layer formation.

4.4. VOLUME FRACTION LOSS DUE TO DISSOLUTION

The reduction of solid phase volume fraction due to Mn dissolution can be calculated based on Eq. 24. The estimated volume changes (100% and 74%) at 2nd and 60th cycles were used to fit the coefficient for Mn dissolution rate, k_{dis}, and the coefficient for electrolyte decomposition rate, k_{decom}, in the dissolution model. Then, the solid phase volume fraction due to dissolution is calculated via the dissolution model for 20th and 40th cycle (Table 5) and the results with the capacity fade due to SEI layer and solid phase volume fraction due to dissolution is plotted as Fig. 4. With the change of volume fraction, the cathode efficient diffusivity is also changed based on Eq. 28, and the initial concentration of two electrodes and SEI layer resistance are not affected by dissolution. At each cycle, the simulated capacity can match well with experimental data with 0.2%, 0.93%, and 0.4% difference. Thus, coupling the effect of SEI layer and dissolution, the SP degradation model can accurately predict the capacity after cycling and predict the

voltage profile within 1.5% errors. The SP degradation model is used to predict the capacity fade of another cell. The comparison of experimental results of cell 2 and simulation results is plotted in Figs. 4c and 4d which indicated that the simulation results matched the cell 2 experimental results within 2% errors.

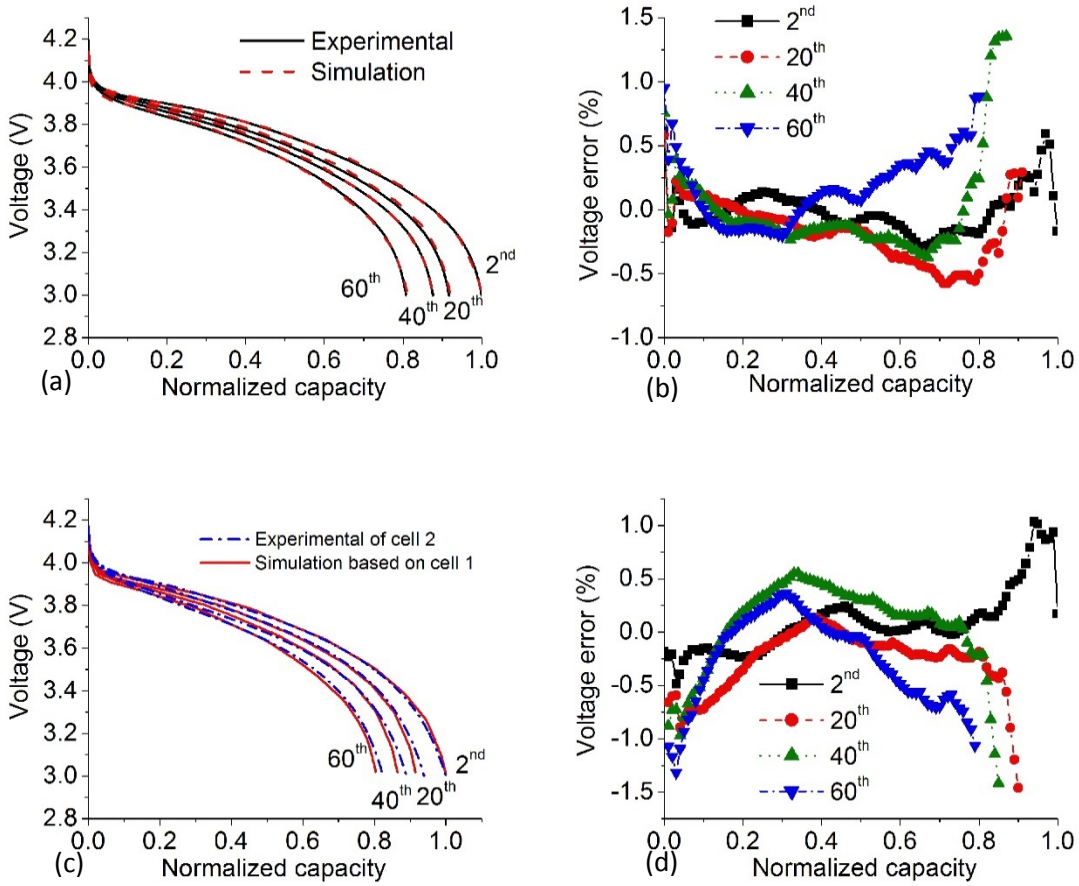

Figure 4. Cycling performance prediction based on dissolution and SEI layer formation cell 1: (a) voltage profile and (b) voltage error, and cell 2: (c) voltage profile and (d) voltage error.

Table 4. Calculated the reduction of solid phase volume fraction and initial electrodes concentration at different cycles

Cycle number	Experimental capacity fade (%)	$\frac{\varepsilon_{1,pos}}{\varepsilon^0_{1,pos}}$ (%)	Initial anode concentration (mol.m^{-3})	Initial cathode concentration (mol.m^{-3})	R_{SEI} (ohm.m^2)	Simulated capacity fade (%)
2nd	0	100	6603.0	3898.5	1e-3	0
20th	8.3	99.7	6038.0	3897.4	1.029e-3	8.5
40th	12.6	94.6	5715.1	3896.8	1.044e-3	13.53
60th	19.2	74	5553.6	3896.5	1.055e-3	19.6

4.5. CAPACITY DEGRADATION ANALYSIS

The comparison of capacity degradation between two experiments and simulation is plotted in Fig. 5a, it indicated that the simulation with coupling the SEI layer and dissolution is able to capture the degradation phenomena accurately. Further, the Li-ion loss due to the SEI layer and volume fraction reduction due to the dissolution as a function of cycle number is decoupled as shown in Fig. 5b, it shows three stages that (1) SEI layer formation dominant cycles, (2) SEI layer stabilizing cycles, and (3) dissolution dominant cycles.

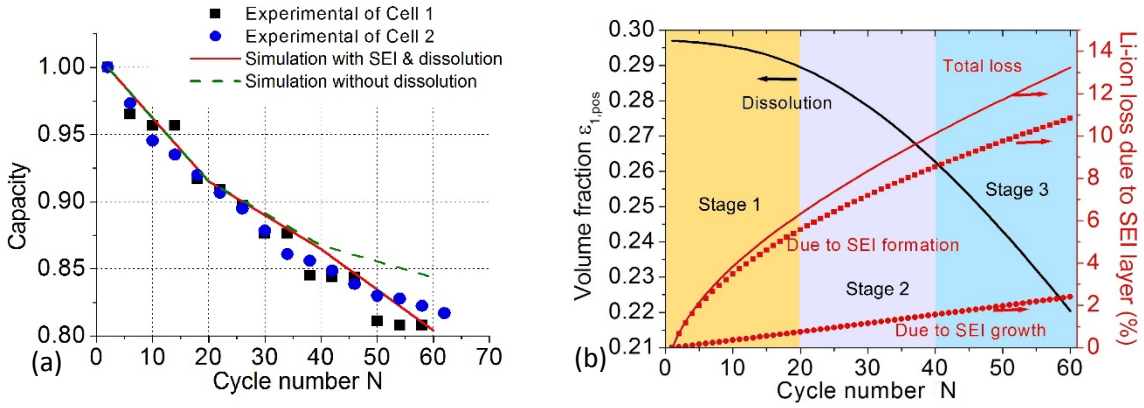

Figure 5. (a) Capacity degradation comparison between experiments and simulation, and (b) Reduction of volume fraction due to dissolution and Li-ion loss (i.e. capacity fade) due to SEI layer formation and growth.

During the SEI layer formation dominate cycles, the Li-ion loss resulting from SEI layer formation and growth on the active material particles in the anode and on the cracks that form on the surfaces of these particles. The Li-ion loss due to SEI layer formation and growth leads to the capacity fade and then the total number of Li-ion inside the cell will be reduced Eq. 2. Correspondingly, the initial concentration at both cathode and anode will be decreased, which will affect the initial SOC and the OCP window at each cycle [31]. On the cathode side, the active material loss due to dissolution is ignorable comparing to Li-ion loss forming SEI layer.

For the dissolution dominant cycles, the capacity fade is due to the cathode active material cannot store enough Li-ions [23,33]. After approximately 30 cycles, as the SEI layer grows thicker, the SEI layer growth slow down. Meanwhile, as Mn dissolution on cathode continues further, the cathode loss overloaded the capacity to contain the reversible Li-ions. Then, the dissolution dominates the capacity fade because the poor capacity of cathode leads to a quick capacity fade, and the SEI layer growth became stable.

One more stage also can be defined between the SEI layer formation dominant cycles and dissolution dominant cycles, where the Li-ion loss due to SEI layer formation trends to stable, while the Mn active material loss did not exceed the loss of Li-ions. Then, the capacity fade is at a stable rate approximately from 20^{th} to 30^{th} cycles as shown in Fig. 6. These stages of degradation have been discussed from full order simulation [23] and experiments [33], which indicated the ability of the SP degradation model is able to reasonably capture the degradation of SEI layer and dissolution.

5. CONCLUSION

In this paper, an advanced physics-based degradation model was developed based on SP model. This model includes two key degradation mechanisms in both anode and cathode materials of the Li-ion battery.

Li-ion loss due to SEI layer formation on the anode, and solid phase volume fraction change due to the dissolution of cathode material are able to be accurately captured, and the effects of them on battery capacity from cycle to cycle were used to modify the initial concentration and diffusion coefficient. In addition, the effect of the two degradation mechanisms on capacity fade and battery performance is studied quantitatively, and the capacity fade can be classed into two parts: SEI layer formation dominant cycles and dissolution dominant cycles. The study will help to control the charge and discharge protocols for extending battery life in a BMS.

REFERENCES

[1] L. D. Couto, J. Schorsch, M. M. Nicotra, and M. Kinnaert, "SOC and SOH estimation for Li-ion batteries based on an equivalent hydraulic model. Part I: SOC and surface concentration estimation," in *2016 American Control Conference (ACC)*, pp. 4022-4028, 2016.

[2] H. Rahimi-Eichi, U. Ojha, F. Baronti, and M.Y. Chow, "Battery management system: an overview of its application in the smart grid and electric vehicles," *IEEE Industrial Electronics Magazine*, vol. 7, pp. 4-16, 2013.

[3] J. Vetter, P. Novák, M. Wagner, C. Veit, K.C. Möller, J. Besenhard, M. Winter, M. Wohlfahrt-Mehrens, C. Vogler, and A. Hammouche, "Ageing mechanisms in lithium-ion batteries," *Journal of Power Sources*, vol. 147, pp. 269-281, 2005.

[4] V. Agubra and J. Fergus, "Lithium ion battery anode aging mechanisms," *Materials*, vol. 6, pp. 1310-1325, 2013.

[5] P. Arora, R. E. White, and M. Doyle, "Capacity fade mechanisms and side reactions in lithium-ion batteries," *Journal of the Electrochemical Society*, vol. 145, pp. 3647-3667, 1998.

[6] R. Hausbrand, G. Cherkashinin, H. Ehrenberg, M. Gröting, K. Albe, C. Hess, and W. Jaegermann, "Fundamental degradation mechanisms of layered oxide Li-ion battery cathode materials: Methodology, insights and novel approaches," *Materials Science and Engineering*: *B*, vol. 192, pp. 3-25, 2015.

[7] M. B. Pinson and M. Z. Bazant, "Theory of SEI formation in rechargeable batteries: capacity fade, accelerated aging and lifetime prediction," *Journal of the Electrochemical Society*, vol. 160, pp. A243-A250, 2013.

[8] J. Li, A. K. Dozier, Y. Li, F. Yang, and Y. T. Cheng, "Crack pattern formation in thin film lithium-ion battery electrodes," *Journal of the Electrochemical Society*, vol. 158, pp. A689-A694, 2011.

[9] J. Dahn, "Phase diagram of Li x C 6," *Physical Review B*, vol. 44, p. 9170, 1991.

[10] L. Beaulieu, S. Beattie, T. Hatchard, and J. Dahn, "The electrochemical reaction of lithium with tin studied by in situ AFM," *Journal of the Electrochemical Society*, vol. 150, pp. A419-A424, 2003.

[11] X. Zhang, W. Shyy, and A. M. Sastry, "Numerical simulation of intercalation-induced stress in Li-ion battery electrode particles," *Journal of the Electrochemical Society*, vol. 154, pp. A910-A916, 2007.

[12] K. Zhao, M. Pharr, J. J. Vlassak, and Z. Suo, "Fracture of electrodes in lithium-ion batteries caused by fast charging," *Journal of Applied Physics*, vol. 108, p. 073517, 2010.

[13] X. Lin, J. Park, L. Liu, Y. Lee, A. Sastry, and W. Lu, "A comprehensive capacity fade model and analysis for Li-ion batteries," *Journal of the Electrochemical Society*, vol. 160, pp. A1701-A1710, 2013.

[14] G. Ning, B. Haran, and B. N. Popov, "Capacity fade study of lithium-ion batteries cycled at high discharge rates," *Journal of Power Sources*, vol. 117, pp. 160-169, 2003.

[15] Jang, Dong H., Young J. Shin, and Seung M. Oh. "Dissolution of Spinel Oxides and Capacity Losses in 4 V Li/Li x Mn2 O 4 Cells." *Journal of The Electrochemical Society* 143.7 (1996): 2204-2211.

[16] J. Christensen and J. Newman, "A mathematical model for the lithium-ion negative electrode solid electrolyte interphase," *Journal of the Electrochemical Society*, vol. 151, pp. A1977-A1988, 2004.

[17] E. Prada, D. Di Domenico, Y. Creff, J. Bernard, V. Sauvant-Moynot, and F. Huet, "A simplified electrochemical and thermal aging model of LiFePO4-graphite li-ion batteries: power and capacity fade simulations," *Journal of the Electrochemical Society*, vol. 160, pp. A616-A628, 2013.

[18] R. Deshpande, M. Verbrugge, Y. T. Cheng, J. Wang, and P. Liu, "Battery cycle life prediction with coupled chemical degradation and fatigue mechanics," *Journal of the Electrochemical Society*, vol. 159, pp. A1730-A1738, 2012.

[19] C. Delacourt and M. Safari, "Mathematical Modeling of Aging of Li-Ion Batteries," in *Physical Multiscale Modeling and Numerical Simulation of Electrochemical Devices for Energy Conversion and Storage*, ed: Springer, pp. 151-190, 2016.

[20] G. Ning and B. N. Popov, "Cycle life modeling of lithium-ion batteries," *Journal of the Electrochemical Society*, vol. 151, pp. A1584-A1591, 2004.

[21] K. Takahashi, and V.Srinivasan, "Examination of graphite particle cracking as a failure mode in lithium-ion batteries: a model-experimental study, " *Journal of the Electrochemical Society*, *162*(4), pp.A635-A645, 2015.

[22] Park, Jonghyun, et al. "Numerical simulation of the effect of the dissolution of LiMn2O4 particles on Li-ion battery performance." *Electrochemical and Solid-State Letters* 14.2 (2011): A14-A18.

[23] Lin, Xianke, et al. "A comprehensive capacity fade model and analysis for Li-ion batteries." *Journal of The Electrochemical Society* 160.10 (2013): A1701-A1710.

[24] V. R. Subramanian, V. D. Diwakar, and D. Tapriyal, "Efficient macro-micro scale coupled modeling of batteries," *Journal of the Electrochemical Society*, vol. 152, pp. A2002-A2008, 2005.

[25] Q. Zhang and R. E. White, "Comparison of approximate solution methods for the solid phase diffusion equation in a porous electrode model," *Journal of Power Sources*, vol. 165, pp. 880-886, 2007.

[26] S. Santhanagopalan and R. E. White, "Online estimation of the state of charge of a lithium ion cell," *Journal of Power Sources*, vol. 161, pp. 1346-1355, 2006.

[27] V. R. Subramanian, V. Boovaragavan, V. Ramadesigan, and M. Arabandi, "Mathematical model reformulation for lithium-ion battery simulations: Galvanostatic boundary conditions," *Journal of the Electrochemical Society*, vol. 156, pp. A260-A271, 2009.

[28] M. Doyle, T. F. Fuller, and J. Newman, "Modeling of galvanostatic charge and discharge of the lithium/polymer/insertion cell," *Journal of the Electrochemical Society*, vol. 140, pp. 1526-1533, 1993.

[29] X. Hu, S. Li, and H. Peng, "A comparative study of equivalent circuit models for Li-ion batteries," *Journal of Power Sources*, vol. 198, pp. 359-367, 2012.

[30] J. Li, N. Lotfi, R. Landers, and J. Park, "A single particle model for lithium-Ion batteries with electrolyte and stress-enhanced diffusion Physics," *Journal of the Electrochemical Society*, vol. 164, pp. A874-A883, 2017.

[31] J. Li, K. Adewuyi, N. Lotfi, R.G. Landers, and J. Park, "A single particle model with chemical/mechanical degradation physics for lithium ion battery State of Health (SOH) estimation. " *Applied Energy, 212*, pp.1178-1190, 2018.

[32] L. Lu, X. Han, J. Li, J. Hua, and M. Ouyang, "A review on the key issues for lithium-ion battery management in electric vehicles," *Journal of Power Sources*, vol. 226, pp. 272-288, 2013.

[33] Zhang, Qi, and Ralph E. White. "Capacity fade analysis of a lithium ion cell." *Journal of Power Sources* 179.2 (2008): 793-798.

SECTION

2. SUMMARIES AND CONCLUSIONS

This research focused on the development of new 3D electrode structures via additive manufacturing to enhance batteries' energy and power densities, and development of fast and accurate physical based battery models to predict the battery status for control purposes in the sophisticated battery management systems.

In the first part of this research, 3D Li-ion battery structures were proposed for achieving high battery performance, such as high areal energy and power densities. In the Paper I, a novel hybrid 3D structure electrode was proposed that utilizes the advantages of digital structure (i.e. high aspect ratio) to break through the limitation posed by the conventional laminated structure, which can be applied to large-scale battery formats. An extrusion-based additive manufacturing method was used to fabricate this hybrid 3D structure with the conventional solution, which resolves the typical challenges in preparing solutions for the extrusion process. The results indicated that significant enhancements can be achieved with the hybrid 3D structure. The hybrid 3D $LiMn_2O_4$ battery showed superior performances, and compared to the conventional structure, the hybrid 3D structure was more efficient and had much better Li-ions utilization. This work resolved fabrication, solution preparation, and assembly issues for a scaled up 3D battery via the extrusion-based additive manufacturing method. In Paper II, a novel macro-micro-controlled 3D electrode was proposed that can achieve high battery performance by utilizing the advantages of the hybrid 3D structure. An extrusion-based additive

manufacturing method was used to control the 3D electrode structure, and an applied electric field was used to further enhance the surface area via manipulating the structure at a particle level. The effect of paste solids loading was well studied and 30% SL can provide the best results for extrusion and battery performance. The effect of the electric field was also well studied that the higher electric field or longer duration time will obtain a better battery performance. In Paper III, a 3D mathematical model was developed for the simulation of batteries' 3D structure. The simulation results were validated with our experimental observation, and the effect of electrode thickness and solid phase volume fraction on battery performance were studied. This model is able to help the design and optimization of 3D electrode structures in the future.

In the second part of this research, an advanced SP model was developed to predict the SOC and SOH in BMS. In Paper IV, a low-order battery model was developed that incorporates stress-enhanced diffusion and electrolyte concentration distribution into a conventional SP model. An approximated analytical solution was derived from the electrolyte concentration distribution by solving the mass transport equation in the electrolyte of a Li-ion cell. It has a simpler and faster than the P2D model, and more accurate than the conventional SP. It was confirmed that this approximate solution can be applied to any combination of operating scenarios, including constant charge/discharge, short/long interval, and rest period, as well as the dynamic loads. In Paper V, an advanced capacity fade model coupled with chemical and mechanical degradation mechanisms was developed based on the new SP model for the electrochemistry and a multi-particle model for mechanical stress. The degradation mechanisms considered capacity decrease due to Li-ion loss resulting from SEI layer

formation and growth on the active material particles of the anode and on the cracks that form on the surfaces of these particles. Li-ion diffusion physics were modified to include effects from mechanical strain energy and changes in battery capacity from cycle to cycle were used to modify the OCP windows. In Paper VI, an SP degradation model was developed for LMO/Graphite battery with considering the dissolution of cathode active materials and Li-ion loss due to SEI layer with crack propagation at anode side. This model was validated with experimental observation for the capacity degradation. Two stages of capacity fade were observed: In the first stage, the Li-ion loss due to SEI layer formation dominated the cell capacity loss, and then the Mn dissolution dominated the cell degradation due to the volume fraction changes. This model, quickly and accurately predicts capacity and voltage as a function of cycles, can be used for SOH estimation in a BMS.

VITA

Jie Li was born in April 1990 in Beijing, P. R. China. In July 2012, he received his Bachelor of Science degree in Material Forming and Control Engineering from North China University of Technology, Beijing, P. R. China. In May 2015, he received his Master's degree in Mechanical and Aerospace Engineering from Missouri University of Science and Technology. In June 2015, he began his study for Ph.D. degree in Mechanical and Aerospace Engineering. His research areas include additive manufacturing and multiscale/Multiphysics modeling for Li-ion battery. In August 2018, he received his Ph.D. degree in Mechanical and Aerospace Engineering from Missouri University of Science and Technology. After his graduation, he has continued to dedicate himself in the field of mechanical engineering.